Ab initio investigations of spin-dependent quantum transport

Jiaqi Zhou

université PARIS-SACLAY

UNIVERSITÉ PARIS SUD
Comprendre le monde, construire l'avenir

北京航空航天大学 BEIHANG UNIVERSITY 1952

NNT : 2019SACLS508

Thèse de doctorat

Etude ab initio du transport quantique dépendant du spin

Thèse de doctorat de Beihang University et de l'Université Paris-Saclay
préparée à l'Université Paris-Sud

École doctorale n°575 Electrical, Optical, Bio : PHYSICS AND ENGINEERING (EOBE)
Spécialité de doctorat : Electronique et Optoélectronique, Nano- et Microtechnologies

Thèse présentée et soutenue à Beijing, le 06/12/2019, par

Jiaqi ZHOU

Composition du Jury :

Dafiné RAVELOSONA Professeur, C2N, Université Paris-Saclay	Président
Tianxiao NIE Professeur, School of Microelectronics, Beihang University	Examinateur
Liliana D. BUDA-PREJBEANU Maître de Conférences, Université Grenoble Alpes, CEA, CNRS, Grenoble INP, SPINTEC	Rapporteur
Ke XIA Professeur, Institute for Quantum Science and Engineering, Southern University of Science and Technology	Rapporteur
Arnaud BOURNEL Professeur, C2N, Université Paris-Saclay	Directeur de thèse
Weisheng ZHAO Professeur, School of Microelectronics, Beihang University	Directeur de thèse
Chun-Gang DUAN Professeur, Key Laboratory of Polar Materials and Devices, Ministry of Education, East China Normal University	Invité
Hongxin YANG Professeur, Ningbo Institute of Materials Technology and Engineering, Chinese Academy of Sciences	Invité

AB INITIO INVESTIGATIONS OF SPIN-DEPENDENT QUANTUM TRANSPORT

A Thesis Submitted in Partial Fulfilment of
the Requirements for the Award of the Degree of

DOCTOR OF PHILOSOPHY

from

UNIVERSITÉ PARIS-SACLAY

by

Jiaqi ZHOU

Centre de Nanosciences et de Nanotechnologies, CNRS
Université Paris-Saclay

2019

CERTIFICATION

I, Jiaqi ZHOU, declare that this thesis, submitted in partial fulfilment of the requirements for the award of DOCTOR OF PHILOSOPHY, in the Centre de Nanosciences et de Nanotechnologies, CNRS, Université Paris-Saclay, is wholly my own work unless otherwise referenced or acknowledged. The document has not been submitted for qualifications at any other academic institution.

Jiaqi ZHOU

(Signature Required)

Jiaqi ZHOU
7th October 2019

Table of Contents

List of Tables

List of Figures

Nomenclatures

2D	Two-Dimensional
AHE	Anomalous Hall Effect
APC	Anti-Parallel Configuration
bcc	body-centered cubic
BZ	Brillouin Zone
DFT	Density Functional Theory
DOS	Density Of States
DOSS	Density Of Scattering States
E_F	Fermi Energy
fcc	face-centered cubic
FET	Field Effect Transistor
GGA	Generalized Gradient Approximation
GMR	Giant MagnetoResistance
HM	Heavy Metal
LDA	Local Density Approximation
LLG	Landau-Lifshitz-Gilbert
MRAM	Magnetic Random Access Memory
MTJ	Magnetic Tunnel Junction
NEGF	Non-Equilibrium Green's Function
PBE	Perdew-Burke-Ernzerhof
PC	Parallel Configuration
PDOS	Projected Density Of States
PMA	Perpendicular Magnetic Anisotropy
SCF	Self-Consistent-Field
SHA	Spin Hall Angle
SHC	Spin Hall Conductivity
SHE	Spin Hall Effect
SIE	Spin Injection Efficiency

SOC	Spin-Orbit Coupling
SOT	Spin-Orbit Torque
STT	Spin-Transfer Torque
vdW	van der Waals
TDOS	Tunneling Density Of States
TMDC	Transition Metal DichalCogenide
TMR	Tunneling MagnetoResistance
AlO_x	Aluminium Oxide
Au	Gold
B	Boron
C	Carbon
Co	Cobalt
Cr	Chromium
Fe	Iron
Ge	Germanium
h-BN	hexagonal Boron Nitrogen
I	Iodine
Ir	Iridium
MgO	Magnesium Oxide
Mo	Molybdenum
N	Nitrogen
Ni	Nickle
Pt	Platinum
Py	Permalloy
S	Sulfur
Se	Selenium
Si	Silicon
Ta	Tantalum
Te	Tellurium
V	Vanadium
W	Tungsten

Ab initio INVESTIGATIONS OF SPIN-DEPENDENT QUANTUM TRANSPORT

Jiaqi ZHOU

A Thesis for DOCTOR OF PHILOSOPHY

Centre de Nanosciences et de Nanotechnologies, CNRS
Université Paris-Saclay

ABSTRACT

Spintronics devices manipulate the electron spin degree of freedom to process information. In this thesis, we investigate spin-dependent quantum transport properties to optimize performances of spintronics devices. Through *ab initio* approach, we research the tunneling magnetoresistance (TMR), spin Hall effect (SHE), as well as spin injection efficiency (SIE). It has been demonstrated that heavy metals (HMs) are able to modulate TMR effects in MgO-based magnetic tunnel junctions (MTJs), and tungsten, molybdenum, and iridium are promising to enhance TMR. Moreover, substitutional atom doping can effectively optimize SHE of HMs, which would strengthen spin Hall angles (SHAs) to achieve efficient spin-orbit torque (SOT) switching of MTJs. To eliminate the mismatch between ferromagnetic and barrier layers in MgO-based MTJs, we design the MTJ with bond-free van der Waals (vdW) heterojunction VSe_2/MoS_2 and report the room-temperature TMR. The occurrence of quantum-well resonances enables voltage control to be an effective method to modulate TMR ratios in vdW MTJ. We put forward the idea of SOT vdW MTJ, which employs SOT to switch vdW MTJ and requires vdW materials with strong SHE. Research on $MoTe_2$ and WTe_2 verifies the possibility of realizing this idea. Both of them are layered transition metal dichalcogenides (TMDC) and exhibit strong SHEs, as well as large SHAs thanks to their low electrical conductivity. Lastly, motivated by the demand of a two-dimensional (2D) switchable device with long spin diffusion length, we construct the spin injection system with silicene monolayer, and reveal high SIEs under electric fields. Works in this thesis would advance the research of spintronics devices.

KEYWORDS: tunneling magnetoresistance, spin Hall effect, spin injection efficiency, magnetic tunnel junction, two-dimensional system, *ab initio* calculation

RÉSUMÉ

• Chapitre 1 : Introduction des concepts fondamentaux de la spintronique

Le chapitre 1 présente les dispositifs et les phénomènes dans le domaine de la spintronique. La mémoire magnétique à accès aléatoire (Magnetic Random Access Memory, MRAM) est une mémoire non-volatile, elle stocke les informations par les spins des électrons. Le dispositif élémentaire de MRAM est la jonction tunnel magnétique (Magnetic Tunnel Junction, MTJ). Elle est basée sur une barrière ultramince entre deux électrodes ferromagnétiques. L'électrode libre est une couche ferromagnétique conservant les informations stockées, la barrière est une couche isolante utilisée pour le transport par effet tunnel et l'électrode fixe présente une forte anisotropie magnétique et une aimantation stable. La MTJ présente une faible résistance quand les moments magnétiques de la couche libre et de la couche fixe sont en configuration parallèle (Parallel Configuration, PC) et une résistance plus grande pour la configuration anti-parallèle (Anti-Parallel Configuration, APC). Dans une MTJ, on peut donc écrire des informations binaires en modifiant l'orientation magnétique de la couche libre et les lire en mesurant la résistance de la structure. La variation de résistance correspond à l'effet de magnétorésistance tunnel (Tunneling MagnetoResistance, TMR). L'augmentation de TMR bénéficie à la fiabilité des MRAM. Au delà de la structure fondamentale, les métaux lourds sont largement utilisés en tant que couche de revêtement et de fond dans des MTJ.

Des calculs théoriques ont prédit en 2001 qu'une TMR élevée peut être obtenue dans un empilement fer/oxyde de magnésium/fer (Fe/MgO/Fe). Depuis lors, beaucoup d'efforts ont été consacrés à l'élaboration des MTJ à base de MgO et des TMR élevées ont été obtenues expérimentalement. Parallèlement, on a également observé que les métaux lourds utilisés comme couches de revêtement des MTJ influencent la valeur de la TMR. La plupart des expérimentateurs attribuent ce phénomène à la diffusion des atomes des métaux lourds, cependant, les études théoriques sur l'influence intrinsèque

causée par les métaux lourds restent insuffisantes. En dépit des avancées réalisées dans les MTJ basés sur MgO, la désadaptation de maille cristalline de 2% entre la couche ferromagnétique et la couche de MgO empêche l'amélioration de TMR. Par ailleurs, les matériaux bidimensionnels (two-dimensional, 2D) et leurs hétérostructures de van der Waals (vdW) offrent une stratégie d'intégration sans limitation vis-à-vis de la maille cristalline. La découverte du ferromagnétisme dans des matériaux 2D permet de les utiliser comme électrodes dans des MTJ, ce qui permet d'atteindre une TMR remarquable à basse température. L'effet TMR n'apparaît cependant jusqu'à présent pas à température ambiante au niveau expérimental.

Une méthode pour écrire des données dans les MTJ est d'utiliser le couple de transfert de spin lié à l'interaction spin-orbite (Spin-Orbit Torque, SOT) qui peut être induit par l'effet de Hall de spin (Spin Hall Effect, SHE). Un courant de spin peut être généré via le SHE par un courant électrique, à travers une contribution extrinsèque (via des collisions dépendant du spin avec des impuretés) ou intrinsèque (liée au couplage spin-orbite caractéristique des matériaux). Dans le deuxième cas, elle est calculable par un formalisme *ab initio* combiné à la formule de Kubo. De telles prédictions théoriques sont utiles pour guider les travaux expérimentaux et optimiser la conception de dispositifs basés sur le SHE.

L'injection efficace de courant polarisé en spin dans un canal diffusif est essentielle pour les dispositifs spintroniques. L'injection du spin a déjà été démontrée dans le graphène avec une haute efficacité et une grande longueur de diffusion de spin. Cependant, l'absence de bande d'énergie interdite dans le graphène empêche la réalisation d'un transistor utilisant le spin. L'émergence de systèmes de spin avec une fonction commutable, une grande longueur diffusion du spin et une efficacité élevée d'injection du spin (Spin Injection Efficiency, SIE) est fortement attendue.

• **Chapitre 2 : Théorie du transport quantique**

Le chapitre 2 présente brièvement les fondements de la théorie de la fonctionnelle de la densité (Density Functional Theory, DFT). Un système solide contient de nombreux noyaux et électrons, donc des approximations et des simplifications sont inévitables pour les analyses pratiques des propriétés physiques. L'approximation de Born-Oppenheimer découple les mouvements des noyaux d'atomes et des électrons, en s'appuyant sur la différence de masse entre les deux types de particules. L'approximation de Hartree transforme le système à plusieurs particules en un système à une particule, de plus, l'approximation de Hartree-Fock introduit le déterminant de Slater pour construire une solution antisymétrique et donner le terme d'échange dans l'hamiltonien. Les théorèmes de Hohenberg-Kohn indiquent que la densité de charge est la quantité fondamentale pour résoudre l'hamiltonien du système, puis l'équation de Kohn-Sham fournit une approche permettant de la calculer par la méthode du champ auto-cohérent (Self-Consistent Field, SCF) et les fonctionnelles d'échange-corrélation.

Le schéma DFT ne peut pas être utilisé dans les systèmes hors d'équilibre car la statistique de Fermi-Dirac utilisée ne s'applique qu'aux systèmes en équilibre. Pour résoudre le problème du transport quantique, la fonction de Green hors d'équilibre peut être mise en oeuvre. Tout d'abord, une estimation initiale de la densité de charge est donnée comme la solution d'équation de Kohn-Sham, alors le potentiel de Kohn-Sham peut être obtenu et la matrice hamiltonienne de dispositif est donnée. Ensuite, avec les énergies propres des électrodes, la fonction de Green du dispositif est calculée, et une nouvelle densité de charge peut être produite par la fonction de Green. La méthode du SCF est utilisée pour faire converger la valeur de densité de charge. Enfin, la fonction de Green est produite et utilisée pour les calculs de propriétés de transport.

• Chapitre 3 : Optimisation de la TMR et du SHE par métaux lourds

Le chapitre 3 discute l'influence des couches de métaux lourds utilisés dans les MTJ à base de MgO sur la TMR et le SHE. Nous étudions des MTJ symétriques avec différents métaux lourds, tantale (Ta), tungstène (W), molybdène (Mo) et iridium (Ir), lesquels sont utilisés comme couches de recouvrement et de fond. Les calculs *ab initio* montrent que les métaux lourds ont un impact important sur la conductance dépendant du spin et la TMR. Les spectres de la transmission dépendant du spin montrent que des pics de la transmission du spin majoritaire apparaissent en PC dans tous les MTJ, à l'exception de celle utilisant Mo. L'analyse des bandes d'énergie révèle que l'absence de la bande Δ_1 au niveau Fermi (Fermi energy, E_F) dans Mo, explique la disparition de ce pic. Le canal de conduction à spin minoritaire en PC est dominé par les états de résonances interfaciaux, lesquels s'atténuent légèrement dans le régime d'effet tunnel ce qui conduit à une grande TMR dans les MTJ à base de Mo. Les MTJ incluant W ou Ir présentent également des effets de TMR remarquables grâce à leur conductance ultra-faible dans l'APC. La tension appliquée aux MTJ réduit l'effet de TMR, en partie à cause de la destruction du tunnel résonnant en PC.

Après cela, nous étudions la conductivité de Hall de spin intrinsèque (intrinsic Spin Hall Conductivity, SHC) des métaux lourds, car la SOT peut être induite par cet effet. La SHC est calculée dans Mo et Ir et les analyses de la courbure de Berry de spin sont présentées. Mo a une SHC de -412 $(\hbar/\mathrm{e})$S/cm à E_F. La SHC d'Ir est 403 $(\hbar/\mathrm{e})$S/cm à E_F et 2056 $(\hbar/\mathrm{e})$S/cm à $E = E_F + 0,84$ eV. Il est fort probable que la SHC de l'Ir puisse être optimisée par un dopage avec des atomes de substitution de platine Pt ou Au. Des atomes de substitution avec un plus grand nombre d'électrons de valence élèvent la position de E_F et augmentent la SHC des alliages d'Ir-Pt et d'Ir-Au par rapport au cas d'Ir. Nous avons étudié la SHC des alliages d'$\mathrm{Ir}_{1-x}\mathrm{Pt}_x$ et d'$\mathrm{Ir}_{1-x}\mathrm{Au}_x$ pour $x = 0{,}125$, 0,25, 0,375, ou 0,5. Dans $\mathrm{Ir}_{0.75}\mathrm{Au}_{0.25}$, la SHC atteint 1475 $(\hbar/\mathrm{e})$S/cm, plus de trois fois

celle dans Ir. Ce résultat démontre que le dopage par substitution est un moyen efficace d'optimiser la SHC, dans le but d'améliorer l'efficacité de renversement par SOT.

• Chapitre 4 : MTJ basées sur des hétérojonctions vdW

Le chapitre 4 propose des MTJ à base des hétérojonctions vdW, qui peuvent être assemblées sans limitation vis-à-vis de la maille cristalline. Des travaux expérimentaux ont rapporté le ferromagnétisme à température ambiante d'une monocouche de diséleniure (VSe_2) préparée sur substrat en disulfure de molybdène (MoS_2). Ayant en vue l'implémentation pratique, nous proposons une MTJ basée sur l'empilement $VSe_2/MoS_2/VSe_2$. Les calculs *ab initio* montrent qu'à l'état d'équilibre, la grande conductance dans l'APC entraîne le déclin de TMR. Nous trouvons que dans l'APC, les états de transmission se localisent au niveau de certaines couches et induisent des résonances, avec une probabilité de transmission extrêmement élevée, proche de l'unité. L'application d'une tension appliquée supprime les résonances, ce qui peut être une méthode efficace pour améliorer la TMR dans des MTJ vdW. Nos calculs indiquent un ratio de TMR à température ambiante pouvant atteindre 846% sous tension, qui passe à 1277% à 100 K. Nous étudions la possibilité de SOT dans les MTJ avec MoS_2 comme couche du fond. La valeur de la SHC dans MoS_2 est seulement de -34 $(\hbar/e)$S/cm à E_F, mais elle peut atteindre 400 $(\hbar/e)$S/cm à $E = E_F - 2.0$ eV, ce qui ouvre des perspectives pour réaliser le renversement d'aimantation.

Pour identifier des matériaux présentant une SHC élevée à E_F, nous avons étudié les semi-métaux $MoTe_2$ et WTe_2. La valeur de SHC s'avère considérable dans les deux cas. Avec des propriétés plus intéressantes que MoS_2, $MoTe_2$ présente une SHC notable de $\sigma_{yx}^z = -361$ $(\hbar/e)$S/cm à E_F, et un angle de Hall de spin (Spin Hall Angle, SHA) élevé de $-0{,}72$. Le SHA est un bon indicateur pour l'efficacité de conversion d'un courant du charge en courant du spin. Un grand SHA peut être attribué à la

SHC élevée et à la faible conductivité électrique du semi-métal. Pour WTe_2, la SHC $\sigma_{xy}^{z} = -204$ $(\hbar/e)$S/cm à E_F et le SHA $= -0{,}54$. Il est intéressant de noter que $MoTe_2$ et WTe_2 ont six éléments de tenseur de SHC non nuls avec des amplitudes différentes. Cette richesse inhabituelle de SHC est mise en évidence pour la première fois dans des matériaux 2D et est attribuée à la symétrie structurelle réduite de $MoTe_2$ et de WTe_2. Ces travaux devraient favoriser l'émergence de dispositif 2D pour la spintronique.

• Chapitre 5 : Système d'injection du spin sur silicène

Motivés par l'exigence de systèmes d'injection du spin avec une fonction commutable, une grande longueur de diffusion du spin et une efficacité d'injection du spin élevée, nous avons étudié un système utilisant le silicène, c'est-à-dire une monocouche constituée d'atomes de Si à structure hexagonale. Des travaux antérieurs ont montré qu'une bande interdite en énergie peut être ouverte dans le silicène en appliquant un champ électrique vertical grâce à sa structure ondulée. Cette bande interdite permet d'envisager l'utilisation du silicène commutable comme canal pour le transport de spin. Nous avons étudié théoriquement le transport de spin dans un canal de silicène associé à un empilement Fe(111)/silicène en tant qu'injecteur de spin. Les calculs hors équilibre montrent que, dans une certaine plage de tension appliquée, le système peut présenter les SIE proches de 100%, provenant de la densité d'états dépendant de spin particulière de l'empilement Fe(111)/silicène. Au-dessus de l'énergie de Fermi, il existe seulement des états du spin minoritaire, d'où le courant dû à ce type d'électrons. Les spectres de la transmission en fonction de l'énergie ont également été étudiés pour comprendre le courant dépendant du spin et les SIE élevés. Cette proposition de système d'injection du spin doit bénéficier au développement de spintronique à base du silicène.

• **Chapitre 6 : Conclusions et perspectives**

Le chapitre 6 résume les conclusions et présente les perspectives de cette thèse. Nous avons étudié le transport quantique dépendant du spin en utilisant des calculs *ab initio* pour concevoir des dispositifs spintroniques à haute performance. Nous nous sommes focalisés sur la magnétorésistance tunnel dans des jonctions tunnel magnétiques, la conductivité de Hall de spin intrinsèque dans des métaux lourds et des matériaux 2D et l'efficacité d'injection de spin dans un système à base de silicène. De futurs travaux pourront porter sur l'évaluation de couple spin-orbite pour le renversement de l'aimantation et la dynamique du spin dans des MTJ.

Chapter 1

Introduction

Spintronics is an interdisciplinary subject investigating and manipulating the electron spin degree of freedom,[1, 2] which enables the electronic device to process information with advantages of the nonvolatility, long endurance, low-power consumption, and high speed.[3, 4] In recent years, thanks to innovative materials and novel device structures, plenty of new phenomena and exciting functionalities emerge in this field,[5–12] making spintronic devices promising for future memory technology. An important spintronic memory is the magnetoresistive random access memory (MRAM),[13–16] whose basic cell is the magnetic tunnel junction (MTJ). In this chapter, we would introduce the mechanisms of reading and writing operations in MTJs, and discuss the research on performances of spintronic devices.

1.1 Magnetic tunnel junction

Figure 1.1(a) shows the atomic diagram and Fig. 1.1(b) shows the transmission electron microscopy image of MTJ. The basic structure of MTJ, from the bottom to the top, consists of seed layer/free layer/tunnel layer/reference layer/capping layer.[17] The ferromagnetic materials are employed as the free layer and reference layer, their

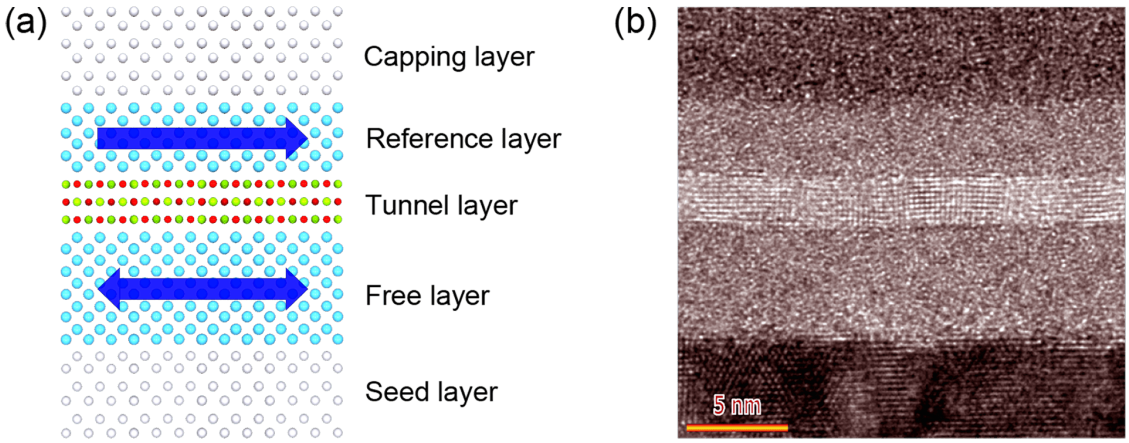

Figure 1.1: (a) Atomic diagram and (b) high-resolution transmission electron microscopy image [17] of a typical MTJ.

magnetizations can be in parallel configuration (PC) or anti-parallel configuration (APC). The tunnel layer is an ultrathin insulator which results in the quantum tunneling transport. Heavy metals (HMs) are extensively used as seed layer and capping layer, to promote the crystallization and prevent oxidation of ferromagnetic layers. Based on the basic MTJ structure, many optimization techniques have been invented, such as the synthetic antiferromagnets structure,[18] double-interface free layer,[19] double tunnel barrier layer,[20] three-terminal MTJ,[21] etc. These creations lead to the enhancement of TMR effect and the reduction of energy dissipation.

Basic functionalities of MTJs include reading and writing operations on data, which are stored through the relative magnetization orientation of two ferromagnets, namely, PC or APC. The reading operation employs the TMR effect, which is the resistance difference between PC and APC of MTJ. Meanwhile, instead of the external magnetic field, the spin-transfer torque (STT) [22] and spin-orbit torque (SOT) [23] can be efficient electrical approaches to write data in MTJs by switching the magnetization of free layer. To optimize MTJ performances including reading reliability and writing energy consumption, many efforts have been devoted to the enhancement of TMR ratio and SOT efficiency, as discussed in the following.

1.2 Tunnel magnetoresistance effect

The resistance of MTJ depends on the relative magnetization alignment of two ferromagnetic layers, as shown by the blue arrows in Fig. 1.1(a). When the magnetizations of two ferromagnetic layers are in PC, the junction exhibits a low-resistance state. When the magnetizations are in APC, the junction exhibits a high-resistance state. The resistance variation originates from the spin-dependent scattering of the electrons. When the magnetizations of both ferromagnetic layers are parallel, the electrons with majority spin, which is parallel with the local magnetization, would be weakly scattered in the quantum tunneling transport, leading to low resistance. However, for the anti-parallel magnetization, both the majority and minority electrons get scattered severely. Consequently, few electrons can pass and high resistance can be observed. This resistance variation between PC and APC of MTJ is the TMR effect, and the ratio of resistance variation is called TMR ratio. We use R to represent the resistance and G to denote the conductance, and define TMR ratio as

$$\text{TMR ratio} = \frac{\mathrm{R_{APC}} - \mathrm{R_{PC}}}{\mathrm{R_{PC}}} \times 100\% = \frac{\mathrm{G_{PC}} - \mathrm{G_{APC}}}{\mathrm{G_{APC}}} \times 100\%. \tag{1.1}$$

In Eq. 1.1, $\mathrm{G_{PC}} = \mathrm{G_{PC}^{\uparrow}} + \mathrm{G_{PC}^{\downarrow}}$, where $\mathrm{G_{PC}^{\uparrow}}$ and $\mathrm{G_{PC}^{\downarrow}}$ is the majority-spin and minority-spin conductance in PC, respectively. $\mathrm{G_{APC}} = \mathrm{G_{APC}^{\uparrow}} + \mathrm{G_{APC}^{\downarrow}}$, where $\mathrm{G_{APC}^{\uparrow}}$ and $\mathrm{G_{APC}^{\downarrow}}$ is the majority-spin and minority-spin conductance in APC, respectively.

In 1975, Jullière firstly reported the tunneling magnetoresistance (TMR) effect with the ratio of 14% at the temperature of 4.2 K in the Fe/Ge/Co junction.[24] Since 18% TMR ratio was reliably realized at room temperature in the $Fe/Al_2O_3/Fe$ junction,[25, 26] the TMR effect started to attract tremendous attention, and extensive theoretical and experimental efforts have been devoted to increasing the TMR ratio at room temperature. However, the TMR ratio in AlO_x-based MTJ was limited to

70%,[27] hindering the practical applications of spintronic devices. Novel insulator materials were investigated and brought great breakthroughs in the enhancement of TMR ratio.[28, 29]

1.2.1 MgO-based MTJ

A revolutionary study through *ab initio* approach predicted that remarkable TMR ratio can be found in the MTJ structure of Fe(100)/MgO(100)/Fe(100).[30–32] A crystalline MgO(100) barrier layer can be epitaxially grown on a body-centered cubic (bcc) Fe(100) layer with a lattice mismatch around 2%. In this way, a relatively perfect crystallization could be realized, and coherent tunneling would happen in the Fe/MgO/Fe stack.

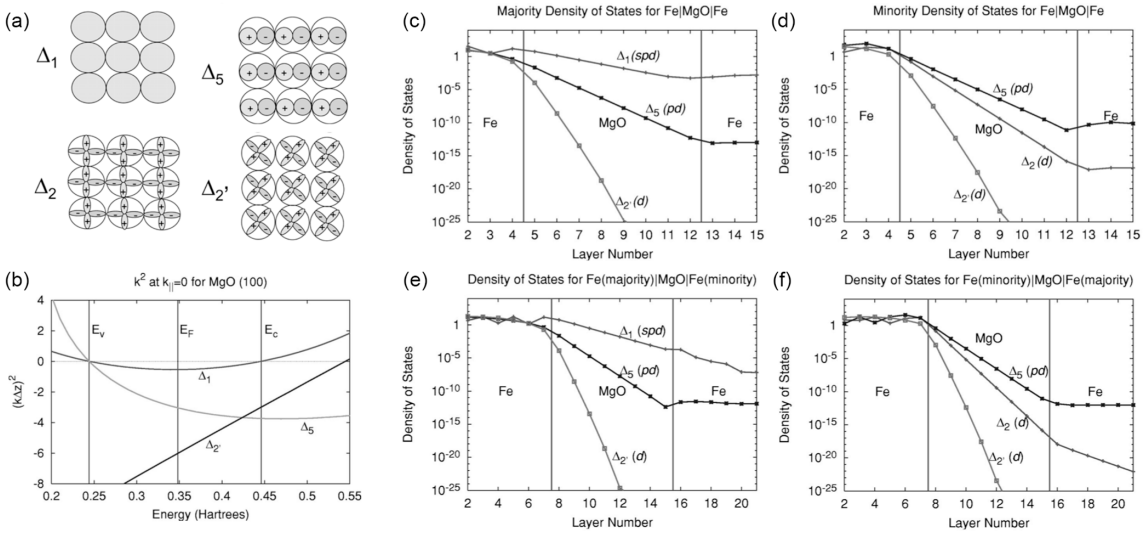

Figure 1.2: (a) Possible symmetries of Bloch states propagating along Δ (100) direction.[30] (b) Dispersion for MgO in the vicinity of the gap along Δ (100).[31] (c)-(f) Tunneling density of states (TDOS) of Fe/MgO/Fe in different spin-dependent channels.[31]

Butler *et al.* calculated the spin-resolved transport properties in Fe/MgO/Fe stack.[31] The high $G_{PC}^{\uparrow}$ as well as a large difference between G_{PC} and G_{APC} have

been found, resulting in a remarkable TMR ratio. It shows that the transmission spectrum of $G_{PC}^{\uparrow}$ has a distinct and broad peak centered at $\boldsymbol{k}_{||} = 0$. To figure out the transmission character, the tunneling density of states (TDOS) for $\boldsymbol{k}_{||} = 0$ was examined. Figure 1.2(a) presents the possible symmetries of Bloch states which participate electronic transport. It can be observed that the Δ_1 Bloch states, i.e. *spd* hybridized states, have the highest symmetry. Figure 1.2(b) displays the dispersion of MgO in the vicinity of the gap along Δ (100) direction. It illustrates that Δ_1 Bloch states have the slowest decay rate in MgO. Flat bands of spin-polarized Fe show that the Δ_1 states are fully spin-polarized at Fermi energy, namely, only the majority-spin states has the Δ_1 band crossing E_F.[33] On the other hand, both the majority- and minority-spin states have the Δ_5 and Δ_2' (Δ_2) symmetries. As a result, for the spin-dependent tunneling transport in PC, Δ_1 states in the majority-spin channel decay in the slowest rate, as shown in Fig. 1.2(c). The rapid attenuation of Δ_2' (Δ_2) and Δ_5 states in MgO can be observed in Figs. 1.2(c)-(f). The spin-dependent tunneling transports in APC are similar and discussions are omitted. Briefly saying, the tunneling transport in the Fe/MgO/Fe MTJ depends strongly on the Bloch states with Δ_1 symmetry. With the matching of Δ_1 states in Fe and MgO, the coherent tunneling in MTJ leads to the large $G_{PC}^{\uparrow}$ as well as high TMR ratio. Following works on Fe/MgO/Fe report impressive results, including the TMR ratio at non-equilibrium states,[34] the oxygen-vacancy-induced diffusive scattering,[35] as well as the thermoelectricity and disorder of CoFe/MgO/CoFe MTJ.[36]

Inspired by the theoretical discovery, great efforts have been devoted to the experimental study of MgO-based MTJs. Utilizing molecular beam epitaxy, Yuasa *et al.* reported a room-temperature TMR ratio of 180% in the single-crystal MTJ with Fe/MgO/Fe structure.[37] Meanwhile, TMR ratio up to 220% was observed in CoFe/MgO/CoFe junction at room temperature.[38] After that, TMR ratio of 500%

can be obtained in MTJs with CoFeB electrodes at room temperature.[39] More intriguingly, by suppressing the diffusion of Ta atoms, a room-temperature TMR ratio of 604% was successfully observed in CoFeB/MgO MTJ.[40] Compared to the polycrystalline CoFe layer,[38] the amorphous CoFeB layer is homogeneous,[40] making it more practical to prepare the MTJ devices in large scale utilizing magnetron sputtering.[41]

On the other hand, due to the potential for high-density MRAM, the interfacial perpendicular magnetic anisotropy (PMA) attracts increasing interests.[42] One pioneering study on p-MTJ is based on the Ta/CoFeB/MgO/CoFeB/Ta stack with a free layer of 1.7 nm and a reference layer as thin as 1.0 nm.[43] Interfacial PMA competes with the bulk in-plane magnetic shape anisotropy, hence the thick CoFeB layer is harmful to PMA. After the annealing process at 300 °C, the MTJ can exhibit a TMR ratio of 124%. Since then, a series of experiments with Ta layers emerged. Jeon *et al.* performed a comprehensive investigation of Ta/CoFeB/MgO-based p-MTJs.[44] They reveal that the TMR ratio strongly depends on the thicknesses of both free and reference layers. The thickness of ferromagnetic layers determines both the PMA strength and the diffusion of Ta atoms, while strong PMA benefits TMR and diffusion damages TMR. Considering all factors, the combination of 1.59 nm free layer and 1.1 nm reference layer is the best strategy for this p-MTJ, and generates the highest TMR ratio of 104%. This work and Ref. [40] report the influence on TMR caused by the Ta diffusion effect, demonstrating that HMs can greatly impact TMR.

Actually, the diffusion effect of Ta atoms is a serious problem. When the annealing temperature increases to 400 °C which is required for the back-end-of-line process of integrated circuit devices, Ta atom diffusion would induce a thick magnetic dead layer especially for long-time annealing, then the instability of APC occurs as well as an obvious reduction of TMR ratio.[45, 46] As a result, it may be challenging to apply the MTJs with Ta layers to MRAM in practice.

Replacing Ta with another heavy metal may overcome the diffusion problem. One promising HM candidate is Mo.[47] It has been reported that for the Mo/CoFeB/MgO structures, the strong PMA remains after annealing at 425 °C. Besides, Mo/CoFeB and CoFeB/MgO interfaces are clearly sharp.[48] The stability of Mo atoms can be attributed to the large formation energy of Mo-Fe alloys.[49] Following work proves that MTJ with Mo layers could exhibit a TMR ratio over 140% after annealing at 400 °C for 2 hours.[49] Moreover, by combining the stability of Mo layer and the good boron sink Ta layer, Almasi *et al.* designed the MTJ with Ta/thin Mo/CoFeB/MgO/CoFeB/thin Mo/Ta stack, which prevents the intermixing of Ta with Fe as well as allows the small B atoms to diffuse out during the annealing process. As a result, a high TMR ratio of 208% has been achieved in this p-MTJ.[50]

On the other hand, with a high melting point which boosts up the annealing stability, the heavy metal W also attracts lots of attention, since the robust W-W bonds can prevent W atoms from diffusing into MgO layer during the annealing process. After the annealing at 420 °C for 10 minutes, the p-MTJ based on W/CoFeB/MgO/CoFeB/W stack can present a TMR ratio of 138%.[46] Lee *et al.* reveal a higher TMR ratio of 163% in p-MTJ with W/Ta seed layer and W capping layer.[51] Both CoFeB layers have been well textured with the MgO layer, thereby realizing a high TMR ratio after annealing at 400 °C. Recently, remarkable TMR ratio have been reported in the MTJ with W monolayer.[52] The MTJ stack consists of double free layers separated by the W monolayer and double CoFeB/MgO interfaces. High TMR ratio of 249% has been observed in this p-MTJ, demonstrating the occurrence of coherent tunneling in crystalline MgO.

Table 1.1 presents TMR ratios in p-MTJs with various HMs. Experiments above demonstrate that HMs greatly impact the TMR in MTJs due to the diffusion effects under different annealing conditions. By virtue of superior thermal stability, Mo and

Table 1.1: TMR in MTJs with varying heavy metal materials, t denotes thickness, T_a represents annealing temperature. All MTJs employed $Co_{20}Fe_{60}B_{20}$ as ferromagnets.

HM	$t_{\text{free layer}}$	$t_{\text{ref layer}}$	t_{MgO}	T_a	TMR (%)	Reference
Ta	1.7	1.0	0.85	300	124	[43]
Ta	1.05	1.59	1.0	-	104	[44]
Ta/thin Mo	1.5	0.85	0.9	500	208	[50]
Mo	1.6	0.8	1.95	400	162	[49]
W	1.0	1.4	1.2	400	163	[51]
W	1.5	0.95	2.4	420	138	[46]
W inserting	1.3 and 0.5	1.0	0.8	390	249	[52]

W metals can be good candidates for high TMR ratios. However, despite abundant experimental achievements, theoretical works studying the intrinsic influence on TMR caused by heavy metals remain inadequate, impeding the comprehension of the role of HMs.

1.2.2 Development of vdW MTJ

Different from the traditional MgO-based MTJ with a 2% lattice mismatch, van der Waals (vdW) MTJs provide a strategy to exterminate lattice mismatch in heterojunctions, thanks to the bond-free integration of vdW materials.[53–55] Breakthroughs in ferromagnetic vdW materials enable the two-dimensional (2D) spintronic devices. Long-range magnetic orders have been found in two different insulating vdW materials, $Cr_2Ge_2Te_6$ and CrI_3.[56, 57] $Cr_2Ge_2Te_6$ is a 2D Heisenberg ferromagnet with small magnetic anisotropy, whereas CrI_3 is a 2D A-type antiferromagnet with strong PMA. However, the ferromagnetic orders in $Cr_2Ge_2Te_6$ and CrI_3 can only be preserved at low temperatures. Later on, gate-tunable room-temperature ferromagnetism was found in Fe_3GeTe_2.[58] In Fe_3GeTe_2, the crystallographic environments of Fe atoms are asymmetric along and normal to the basal plane, leading to the sizable magnetocrys-

talline anisotropy. Recently, room-temperature and intrinsic ferromagnetism has been discovered in the 2D ferromagnets VSe_2 monolayer which can be grown on MoS_2 by molecular beam epitaxy,[59] providing the possibility of 2D spintronic applications.

The observations of intrinsic ferromagnetism in vdW materials trigger interests in spintronic devices. Recently, MTJs based on vdW materials have been studied a lot.[60–63] Tunneling spin valves have been achieved using exfoliated Fe_3GeTe_2 as ferromagnetic layers and h-BN as the tunnel layer, and the TMR signal reaches up to 160% at 4.2 K.[64] The vdW heterojunctions consisting of CrI_3 tunnel layers exhibit larger TMR performances. Layer-dependent magnetic phases have been observed in CrI_3-based MTJs,[65] and TMR can be drastically enhanced with increasing CrI_3 layer thickness, reaching up to 19000% at the ultra-low temperature of 2 K. Works above reveal the possibility to shrink the MTJ scale to the atomically thin limit with versatile vdW materials, as well as remarkable TMR effects in vdW MTJs. Meanwhile, we anticipate the achievement of room-temperature TMR in vdW MTJs, which would promote the application of vdW devices.

1.3 Spin Hall effect

For the writing operation, STT and SOT can be employed to switching the magnetization of free layer. Despite advances in STT method, there still remains some challenges. The same path of reading and writing currents results in undesirable writing operation in the readout process, meanwhile increasing the probability of tunnel layer breakdown. Besides, STT MRAM is hard to reach the speed required by cache memory.[66–68] The emerging SOT MRAM provides an alternative method to solve above issues.[69–75] In the three-terminal SOT MTJ, the separation of reading and writing paths reduces the write error rate and improves the device endurance. Meanwhile, Cubukcu *et al.* has reported an ultra-fast bipolar magnetization switching down

to 400 ps in perpendicular SOT MTJ, making SOT MRAM promising for the cache memory application.[76] In the SOT MTJ, writing current is injected into the bottom layer consisting of heavy metal, where SHE occurs and induces SOT.[77, 78] In this section, we discuss the SHE and SHE-induced SOT.

1.3.1 Mechanisms of SHE

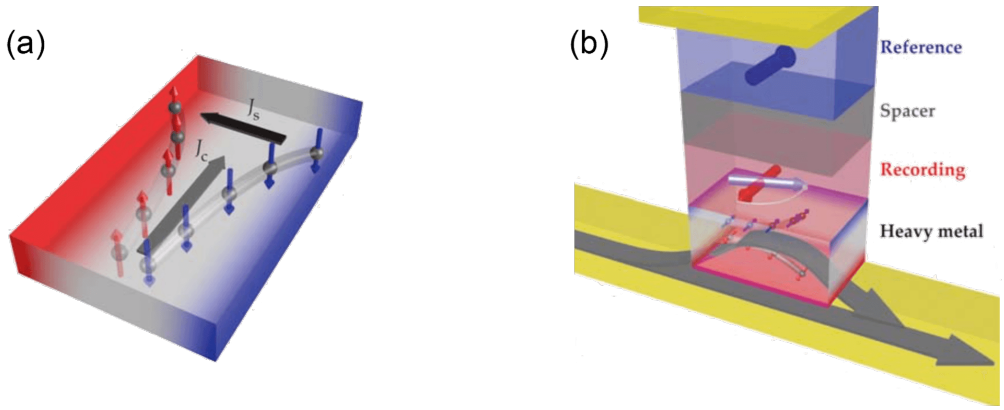

Figure 1.3: Schematics of (a) Spin Hall effect and (b) SOT induced by SHE.[79]

The generation, manipulation, and detection of spin currents are key aspects in the field of spintronics. In this field, spin Hall effect has been extensively used. As shown in Fig. 1.3(a), in SHE, spin-dependent deflections due to the spin-orbit coupling (SOC) generates a spin current J_s (black arrow), which is transverse to the charge current J_c (gray arrow). The spin polarization is perpendicular to the plane defined by the spin and charge currents.[79] Inspired by the theoretical framework of anomalous Hall effect (AHE),[80] the sources of SHE can be divided into three distinct microscopic mechanisms, namely, the intrinsic, the skew-scattering, and the side jump mechanisms.[10]

- *Intrinsic mechanism*

The intrinsic contribution to the spin Hall conductivity (SHC) depends only on the band structure of the perfect crystal. It can be calculated accurately using *ab initio*

technique. According to the Kubo formula,[81, 82] SHC can be written as

$$\begin{aligned}\sigma_{xy}^{z}(\omega) = \ & \hbar \int_{\mathrm{BZ}} \frac{d^3k}{(2\pi)^3} \sum_{n} f_{n\boldsymbol{k}} \\ & \times \sum_{m \neq n} \frac{2\,\mathrm{Im}\left[\langle n\boldsymbol{k}|\hat{j}_x^z|m\boldsymbol{k}\rangle \langle m\boldsymbol{k}|-e\hat{v}_y|n\boldsymbol{k}\rangle\right]}{\left(\epsilon_{n\boldsymbol{k}} - \epsilon_{m\boldsymbol{k}}\right)^2 - (\hbar\omega + i\eta)^2}\end{aligned} \tag{1.2}$$

where σ_{xy}^{z} is a third-rank tensor and represents the spin current along x direction produced by an electric field along y direction, and the spin current is polarized along z direction. ϵ_n and ϵ_m are the eigenvalues, n and m are band indexes. BZ denotes the first Brillouin zone, $f_{n\boldsymbol{k}}$ is the Fermi distribution function, $\hat{j}_x^z = \frac{1}{2}\{\hat{s}_z, \hat{v}_x\}$ is the spin current operator, $\hat{s}_z = \frac{\hbar}{2}\hat{\sigma}_z$ is the spin operator, $\hat{v}_y = \frac{1}{\hbar}\frac{\partial H(\boldsymbol{k})}{\partial k_y}$ is the velocity operator and $H(\boldsymbol{k})$ is the Hamiltonian matrix. Frequencies ω and η are set to zero in the direct current.

- *Skew-scattering mechanism*

The defect in a crystal may change the moving directions of the electrons through scattering. Electrons in different paths (deviating to the left or to the right) experience opposite effective magnetic fields caused by SOC, leading to different scattering probabilities for electrons with opposite spin angular momenta, as well as a subsequent spin current flowing perpendicularly to the charge current.

- *Side-jump mechanism*

In a crystal, a defect produces an electric field around itself. When an itinerant electron passes in the vicinity of the defect, it experiences an effective magnetic field caused by SOC, which comes from the electrical field of defect. For the straight-going electron passing through the defect from left or right side, opposite lateral displacement would be generated depending on the spin angular momentum of electron, leading to disparate paths for electrons with different spin as well as the subsequent spin current.

1.3.2 SOT induced by SHE

Spin-orbit torque originates from the transfer of angular momentum from lattice to spin system in the ferromagnet/nonmagnetic metal bilayer.[72, 75, 83–85] The dynamics of ferromagnetic layer is governed by the Landau-Lifshitz-Gilbert (LLG) equation

$$\frac{d\mathbf{m}}{dt} = -\gamma \mathbf{m} \times \mathbf{B_M} + \alpha \mathbf{m} \times \frac{d\mathbf{m}}{dt} + \frac{\gamma}{M_s}\mathbf{T} \tag{1.3}$$

where $m = \mathbf{M}/M_s$ is the unitary magnetization vector and M_s is the saturation magnetization, γ is the gyromagnetic ratio, and α is the Gilbert damping parameter. The first term on the right side of Eq. 1.3 is the precession of the magnetization $\mathbf{m}$ around the effective field $\mathbf{B_M}$. The second term denotes the magnetization relaxation towards its equilibrium position. The third term accounts for other torques induced by the electrical current, e.g. STT or SOT. Such torques are defined to be orthogonal to the magnetization $\mathbf{m}$ in the form of

$$\mathbf{T} = \tau_{\mathrm{FL}} \mathbf{m} \times \zeta + \tau_{\mathrm{DL}} \mathbf{m} \times (\mathbf{m} \times \zeta), \tag{1.4}$$

where ζ is a unit vector determined by the spin-charge conversion originating from SOC. Generally, τ_{FL}, the field-like torque, denotes the longitudinal component lying in the $(\mathbf{m}, \zeta)$ plane. τ_{DL}, the damping-like torque, is the transverse component normal to the $(\mathbf{m}, \zeta)$ plane.

Figure 1.3(b) presents the picture of SHE-induced SOT, where SHE effectively turns the HM into a spin injector. Then, the angular momentum of the pure spin current is absorbed by the proximate ferromagnetic layer.[79, 83] Next, SHE-SOT works similarly to STT, i.e., the angular momentum is transferred from the spin current to the local magnetization, and then realizes the magnetization switching in the free layer.[70, 71] Since the SHE-SOT model provides an insightful picture to the origin of

SOT, it is widely adopted in experimental investigations.

Plenty of works have reported SHE and SOT in ferromagnet/HM devices with different HM materials, such as Ta, W, Pt, Ir, etc.[71, 77, 86, 87] To realize the SOT switching, it is in urgent need to find HMs with superior spin Hall properties, including strong SHE and large spin Hall angle (SHA), which is defined as the ratio of spin Hall conductivity and electrical conductivity, indicating the efficiency of spin-charge conversion.

Overall, with advantages of low-power consumption, long endurance and high speed, SOT MRAM is a competitive candidate for the next-generation spintronic memory technology, and the identification of HMs with desirable spin Hall properties is urgently required to achieve the efficient SOT switching.

1.4 Spin injection system

Logic device is another application of spintronics. The efficient injection of spin-polarized current into a diffusive channel is important, since spin logic devices exploit spin as input and detect spin as output.[88, 89] For this reason, intense research efforts have been devoted to the improvement of spin injection efficiency (SIE) using new materials and structures.

Thanks to the weak SOC and long spin diffusion length of graphene, the spin injection into epitaxial graphene has been widely studied.[90–92] Karpan *et al.* observed that the in-plane lattice constants of ferromagnets Co and Ni can match well with the in-plane lattice constant of graphite. They reveal that the electronic structures of Co (Ni) and graphite overlap in reciprocal space only for one spin component, and predict the perfect spin filtering for the ferromagnet/graphite interface.[93] Besides, Maassen *et al.* performed an *ab initio* research on the ferromagnet/graphene interface using Co(111) and Ni(111). The use of Co and Ni ferromagnets achieves SIE

reaching up to 80% and 60%, respectively. High SIEs result from the interaction between the ferromagnets and graphene. The band structures show that the linear dispersion relations of the graphene have been damaged by ferromagnets, leading to a spin-dependent energy gap at K point. The minority-spin band gap resides in high energy, while the majority-spin band gap locates near the Fermi energy. This feature results in a dominant minority-spin-polarized current, as well as the high SIE.[94] However, generally, the computational cost of *ab initio* method is relatively high. Lazić *et al.* formulated a computationally inexpensive model to examine the non-uniformity and bias dependence of spin injection. They elucidate proximity effects using spin polarization maps, extending the applicability of simple spin injection models based on ferromagnet/graphene junctions.[95]

Apart from theoretical studies, significant progresses have also been made in experiments.[96, 97] Taking the advantage of high-impedance injecting/detecting tunnel junctions of Co/Al_2O_3/graphene, Dlubak *et al.* report an SIE up to 75% and a spin diffusion length exceeding 100 μm in graphene.[98] Works above demonstrate the possibility to manipulate spin injection and spin-polarized current efficiently in 2D systems. However, the lack of energy gap in graphene impedes the application of graphene transistor device.[99, 100] We expect the emergence of spin injection system with characters of tunable gap, long spin diffusion length as well as high spin injection efficiency.

1.5 Summary

In this chapter, we introduce the key effects and devices in the field of spintronics. MTJ is the basic cell of MRAM device. The reading operation of data exploits the TMR effect, and an efficient approach of writing manipulation is the SOT switching, which can be induced by SHE. HMs in MTJs play an important role on both TMR and

SHE. On the other hand, vdW materials provide a strategy to overcome the problem of lattice mismatch existing in MgO-based MTJs, and experimental works on vdW MTJs have achieved remarkable TMR ratios. Moreover, spin transport systems based on 2D materials provide intriguing perspectives for spin logic devices.

This thesis will be organized as follows. In Chapter 2, the density functional theory is reviewed. We briefly present the theory of quantum transport, which can be investigated using non-equilibrium Green's function. Chapter 3 focuses on the role of heavy metals in MTJs based on the CoFe/MgO/CoFe stack. We theoretically research the influence on TMR caused by HMs, as well as the spin Hall effects in various HMs and optimization approach. Chapter 4 studies the MTJs based on vdW materials. We report room-temperature TMR effects in MTJs consisting of VSe_2/MoS_2 heterojunctions, and demonstrate that the $MoTe_2$ and WTe_2 can exhibit strong SHE and large SHA, making it promising to realize the SOT switching of vdW MTJ. Chapter 5 presents the spin transport system based on silicene. We reveal the efficient spin injection in the system where Fe/silicene stack is spin injector and silicene acts as spin transport channel. Chapter 6 summarizes this thesis and proposes the future work.

Chapter 2

Quantum transport theory

The working principles of electronic devices are governed by the physics of electron transport. As the feature size of electronic devices tends to the nanometer scale, quantum mechanical effects are playing an increasingly important role in transport theory. Thus, it is essential to consider the microscopic origin of physical effects and use advanced theoretical methods to accurately predict device properties. In this chapter, we will introduce the basic concepts of the quantum transport theory and methods for the atomic scale calculation.

2.1 Density functional theory

This section will briefly present the fundamentals of density functional theory (DFT), which is extensively used to calculate the ground-state electronic structure of atoms, molecules, and solid-state materials. In principle, the solid system contains numerous nuclei and electrons, thus, approximations and simplifications are inevitable for the practical analyses of physical properties. Born-Oppenheimer approximation separates the movements of nuclei and electrons. Hartree approximation turns the many-particle system to a single-particle system, and the self-consistent-field has been used to solve

the Hartree equation. Hartree-Fock approximation introduces the Slater determinant to build an antisymmetric solution and results in the exchange term in the Hamiltonian. Based on Hohenberg-Kohn theorems, DFT regards the electron density as the fundamental quantity, and provides an alternative approach to the Kohn-Sham equation.

2.1.1 Born-Oppenheimer approximation

The Schrödinger equation of many-particle system can be written as

$$\left(T_{\mathrm{I}} + V_{\mathrm{II}} + V_{\mathrm{eI}} + T_{\mathrm{e}} + V_{\mathrm{ee}}\right)\chi(\mathbf{R}_{N_I}, \mathbf{r}_{N_e}) = E\chi(\mathbf{R}_{N_I}, \mathbf{r}_{N_e}), \tag{2.1}$$

where $\mathbf{R}_{N_I}$ denotes the coordinates of all nuclei, $\mathbf{r}_{N_e}$ denotes the coordinates of all electrons, $\chi(\mathbf{R}_{N_I}, \mathbf{r}_{N_e})$ is the wave function of many-particle system and E is energy. T_{I} is the kinetic energy of nuclei, V_{II} is the Coulomb repulsion between nuclei, V_{eI} is the Coulomb attraction between nuclei and electrons, T_{e} is the kinetic energy of electrons, and V_{ee} is the Coulomb repulsion between electrons. Setting $e^2 = \hbar = 2m_e = 1$ where e represents the elementary electron, $\hbar$ is the reduced Plank constant, m_e is the electron mass, we can write

$$\begin{aligned} T_{\mathrm{I}} &= -\sum_{\mu=1,N_I} \frac{1}{2M_\mu}\nabla_\mu^2,\ V_{\mathrm{II}} = \sum_{\mu\neq\nu} \frac{Z_\mu Z_\nu}{|\mathbf{R}_\mu - \mathbf{R}_\nu|}, \\ T_{\mathrm{e}} &= -\sum_{i=1,N_e} \nabla_i^2,\ V_{\mathrm{ee}} = \sum_{i\neq j} \frac{1}{|\mathbf{r}_i - \mathbf{r}_j|}, \\ V_{\mathrm{eI}} &= -\sum_{\mu=1,N_I}\sum_{i=1,N_e} \frac{Z_\mu}{|\mathbf{R}_\mu - \mathbf{r}_i|}, \end{aligned} \tag{2.2}$$

where M_μ is the mass of nucleus, Z is the atomic number. Considering the fact that nuclei are much slower in movement and heavier in mass than electrons, we can assume that the motion of atomic nuclei and electrons can be treated separately. This

assumption is the Born-Oppenheimer approximation.[101] Thanks to the separation, we can write the total wavefunction of the nuclei-electrons system as a multiplication of two wavefunctions for nuclei and electrons which are decoupled as

$$\chi(\mathbf{R}_\mu, \mathbf{r}_i) = \Phi(\mathbf{R}_\mu)\Psi_{\mathbf{R}}(\mathbf{r}_i), \tag{2.3}$$

where $\Psi_{\mathbf{R}}(\mathbf{r}_i)$ is the electron wavefunction satisfying the Schrödinger equation

$$\left(T_\mathrm{e} + V_\mathrm{eI} + V_\mathrm{ee}\right)\Psi_{\mathbf{R}}(\mathbf{r}_i) = E_{\mathbf{R}}\Psi_{\mathbf{R}}(\mathbf{r}_i). \tag{2.4}$$

In Eq. 2.4, the index $\mathbf{R}$ is a reminder that both the wave function and the energy depend on the nuclei coordinates via V_eI.

2.1.2 Hartree approximation

Even though the Born-Oppenheimer approximation has simplified the Schrödinger equation to a large extent, it is still impossible to solve the many-electron Schrödinger equation due to the difficulties in dealing with the electron-electron interaction. Further approximations are required.

Consider a simple assumption that the many-electron system can be written as a multiplication of many single-electron wavefunctions. The wavefunction of the many-electron system $\Psi(\mathbf{r})$ can be expressed as

$$\Psi(\mathbf{r}) = \psi_1(\mathbf{r}_1)\psi_2(\mathbf{r}_2)\ldots\psi_N(\mathbf{r}_N), \tag{2.5}$$

where $\psi_i(\mathbf{r}_i)$ is the wavefunction of the single-electron system. Equation 2.5 is called Hartree wavefunction, and this assumption is named as Hartree approximation.[102] The wavefunction $\Psi(\mathbf{r})$ satisfies the Schrödinger equation

$$H\Psi(\mathbf{r}) = E\Psi(\mathbf{r}) \tag{2.6}$$

and the total energy can be calculated by

$$E = \langle \mathbf{\Psi} | H | \mathbf{\Psi} \rangle = \sum_i \langle \psi_i | H_i | \psi_i \rangle + \frac{1}{2} \sum_{i,j} \langle \psi_i \psi_j | H_{ij} | \psi_i \psi_j \rangle , \tag{2.7}$$

where H_i is single-electron Hamiltonian, H_{ij} is the Hamiltonian denoting two-electron interaction. By applying the variational principle to the many-electron Schrödinger equation Eq. 2.6, we can arrive at the single-electron equation

$$\left[-\nabla^2 + V_{\text{ext}}(\mathbf{r}) + \sum_{i'(\neq i)} \int \mathrm{d}\mathbf{r}' \frac{|\psi_{i'}(\mathbf{r}')|^2}{|\mathbf{r}' - \mathbf{r}|} \right] \psi_i(\mathbf{r}) = E_i \psi_i(\mathbf{r}). \tag{2.8}$$

Equation 2.8 is called Hartree equation. It shows that the $-\nabla^2$ term in the left side is the single-electron kinetic energy, and the single electron obeying an effective potential, which is a combination of the external potential $V_{\text{ext}}(\mathbf{r})$ and the potential caused by all other electrons, i.e., Hartree potential V_{Hartree}.

2.1.3 Hartree-Fock approximation

Although the Hartree equation has made great progress by coming up with the Hartree potential, it still has some limitations, such as the Hartree approximation did not respect the principle of antisymmetry of the wave function.[103] As an alternative method, we can build an antisymmetric solution by introducing the following Slater determinant:

$$\Psi(\mathbf{r}_1, \mathbf{r}_2, \ldots, \mathbf{r}_N) = \frac{1}{\sqrt{N!}} \begin{vmatrix} \psi_1(\mathbf{r}_1) & \psi_2(\mathbf{r}_1) & \cdots & \psi_N(\mathbf{r}_1) \\ \psi_1(\mathbf{r}_2) & \psi_2(\mathbf{r}_2) & \cdots & \psi_N(\mathbf{r}_2) \\ \vdots & \vdots & \ddots & \vdots \\ \psi_1(\mathbf{r}_N) & \psi_2(\mathbf{r}_N) & \cdots & \psi_N(\mathbf{r}_N) \end{vmatrix} . \tag{2.9}$$

By the variational principle, the expectation value of the single-electron Hamilto-

nian $E = \langle\psi_i(\mathbf{r}_i)|H|\psi_i(\mathbf{r}_i)\rangle$ for single-electron state ψ can be obtained, as well as the Hartree-Fock equation:

$$\left[-\nabla^2 + V_{\text{ext}}(\mathbf{r}) + \sum_{i'(\neq i)} \int \mathrm{d}\mathbf{r}' \frac{|\psi_{i'}(\mathbf{r}')|^2}{|\mathbf{r}' - \mathbf{r}|}\right] \psi_i(\mathbf{r}) - \sum_{i'(\neq i),||} \int d\mathbf{r}' \frac{\psi^*_{i'}(\mathbf{r}')\psi_i(\mathbf{r}')}{|\mathbf{r}' - \mathbf{r}|}\psi_{i'}(\mathbf{r}) = E_i\psi_i(\mathbf{r}). \tag{2.10}$$

Compared with the Hartree equation Eq. 2.8, the Hartree-Fock equation Eq. 2.10 has one more term $\sum_{i'(\neq i),||} \int d\mathbf{r}' \frac{\psi^*_{i'}(\mathbf{r}')\psi_i(\mathbf{r}')}{|\mathbf{r}'-\mathbf{r}|}\psi_{i'}(\mathbf{r})$ which is called the exchange term, where $||$ denotes the same spin. However, the Hartree-Fock solution is not exact, since generally, the system could not be described by wavefunction in the form of a Slater determinant. The energy difference between the exact solution and Hartree-Fock solution is called the correlation energy. This name originates from the fact that Hartree-Fock approximation misses part of the "electron correlation", i.e., an artificial effect caused by our assumption that the many-electron system can be described by a single-electron equation obeying an effective potential.

2.1.4 Hohenberg-Kohn theorem

Discussions above demonstrate that the Hartree-Fock approximation is not accurate. On the other hand, the density functional theory provides alternative methods to solve this problem. In 1927, Thomas [104] and Fermi [105] put forward the basic idea of DFT, i.e., the fundamental physical properties of atoms, molecules and bulks can be described by the densities of particles. Namely, the functional of electron density can determine the ground state properties of systems. This idea originated from two famous Hohenberg-Kohn theorems:[106]

- *The first Hohenberg-Kohn theorem:*

  The external potential $V_{\text{ext}}(\mathbf{r})$ and the total energy are uniquely determined by

the ground-state electron density $\rho(\mathbf{r})$.

- *The second Hohenberg-Kohn theorem:*

  The ground-state energy can be obtained variationally: The electron density that minimizes the total energy is the exact ground-state density, within an additive constant.

Hohenberg-Kohn theorems illustrate that the electron density is the basic variable to determine the properties of many-electron system, and the ground state of system can be obtained using the variation of energy with respect to the electron density. In the following, we will discuss how to get the electron density and energy of ground state.

We consider a non-degenerate ground state, where the energy of many-electron system without spin can be written as

$$E_{\mathrm{HK}}[\rho(\mathbf{r})] = T_{\mathrm{e}} + V_{\mathrm{ee}} + V_{\mathrm{eI}} + T_{\mathrm{I}} + V_{\mathrm{II}} = T[\rho(\mathbf{r})] + E_{\mathrm{int}}[\rho(\mathbf{r})] + V_{\mathrm{ext}}(\mathbf{r}) + E_{\mathrm{II}}, \quad (2.11)$$

where $T[\rho(\mathbf{r})]$ denotes the kinetic energies of electrons, $E_{\mathrm{int}}[\rho(\mathbf{r})]$ illustrates the potential energies of electrons, and $V_{\mathrm{ext}}(\mathbf{r})$ represents the potential energies between electrons and nuclei. $E_{\mathrm{II}} = T_{\mathrm{I}} + V_{\mathrm{II}}$ is the sum of kinetic and potential energies of nuclei. $V_{\mathrm{ext}}(\mathbf{r})$ and E_{II} can be calculated accurately, consequently, we focus on how to get the electron-related energies in the following.

We define the energy functional of electrons $F_{\mathrm{HK}}[\rho(\mathbf{r})]$ as

$$F_{\mathrm{HK}}[\rho(\mathbf{r})] = T[\rho(\mathbf{r})] + E_{\mathrm{int}}[\rho(\mathbf{r})], \quad (2.12)$$

where $T[\rho(\mathbf{r})]$ accurately describes the kinetic energies of electrons, and the potential energies of electrons $E_{\mathrm{int}}[\rho(\mathbf{r})]$ comprise the energies of Hartree potential and electrons'

interactions. In this condition, to calculate the properties of ground state, we have three problems to be solved:

(1) How to find out the electron density $\rho(\mathbf{r})$?

(2) How to get the electron kinetic functional $T[\rho(\mathbf{r})]$?

(3) How to describe the electron potential functional $E_{\text{int}}[\rho(\mathbf{r})]$?

2.1.5 Kohn-Sham equation

To answer the questions mentioned above, we introduce the concept of Kohn-Sham equation,[107] which can be written as

$$\left\{-\nabla^2 + V_{\text{KS}}[\rho(\mathbf{r})]\right\}\psi_i(\mathbf{r}) = E_i\psi_i(\mathbf{r}). \tag{2.13}$$

In Eq. 2.13, the ∇^2 term in the left side represents the kinetic energy of single electron, and the Kohn-Sham potential V_{KS} is

$$\begin{aligned} V_{\text{KS}}[\rho(\mathbf{r})] &= V_{\text{ext}}(\mathbf{r}) + V_{\text{Hartree}}[\rho(\mathbf{r})] + V_{\text{xc}}[\rho(\mathbf{r})] \\ &= V_{\text{ext}}(\mathbf{r}) + \int \mathrm{d}\mathbf{r}' \frac{\rho(\mathbf{r}')}{|\mathbf{r}-\mathbf{r}'|} + \frac{\delta E_{\text{xc}}[\rho(\mathbf{r})]}{\delta\rho(\mathbf{r})}. \end{aligned} \tag{2.14}$$

and the electron density is

$$\rho(\mathbf{r}) = \sum_{i=1}^{N} f(E_i,\mu)\left|\psi_i(\mathbf{r})\right|^2. \tag{2.15}$$

where $f(E_i,\mu)$ is the Fermi-Dirac distribution function, and μ is the electrochemical potential.

The Kohn-Sham equation Eq. 2.13 has a similar form to the Hartree-Fock equation Eq. 2.10, except the effective potential term $V_{\text{KS}}[\rho(\mathbf{r})]$. With the given electron density $\rho(\mathbf{r})$ and the exchange-correlation term $V_{\text{xc}}[\rho(\mathbf{r})]$ which comprises complicated

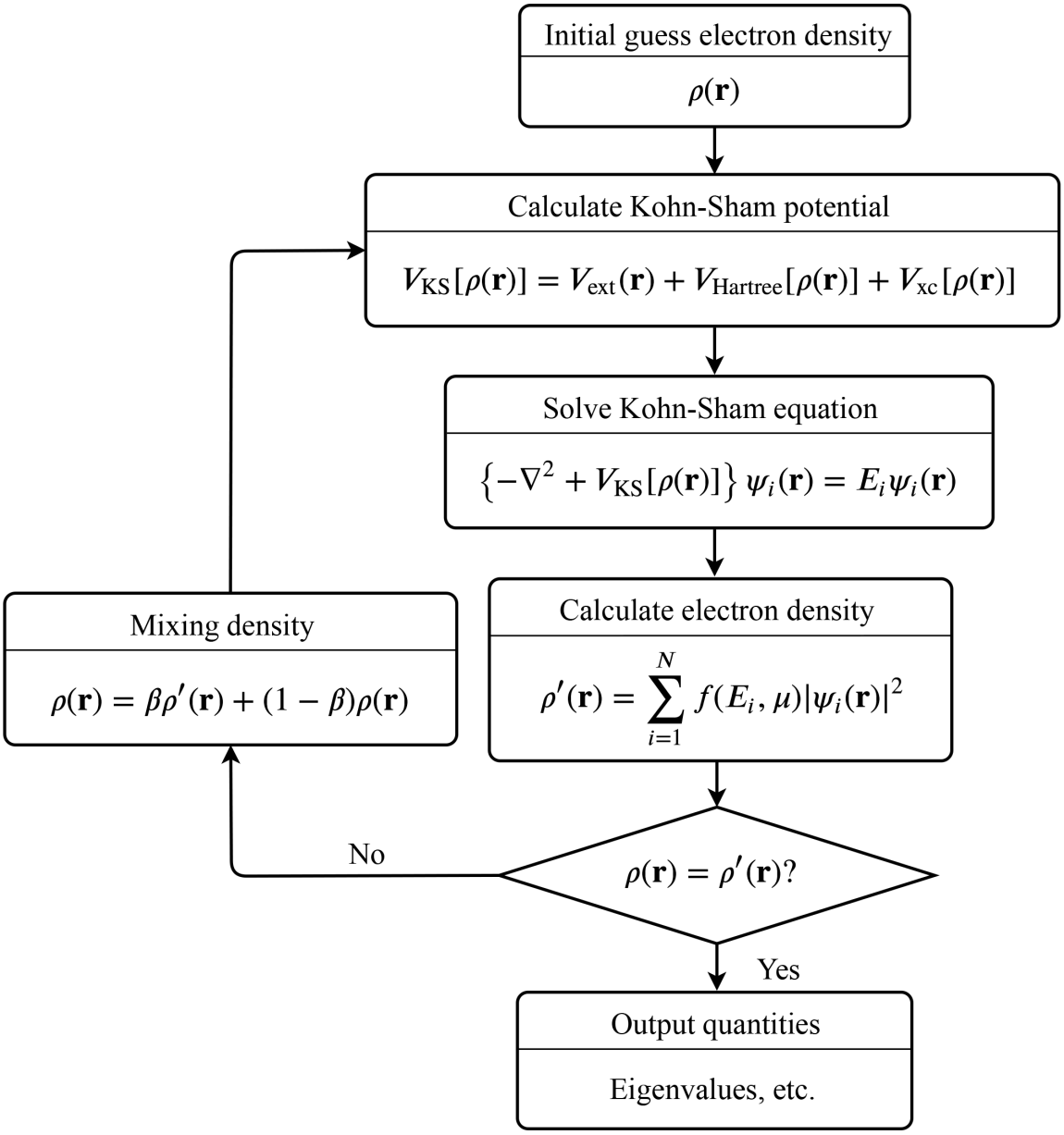

Figure 2.1: Flow chart of solving the Kohn-Sham equation.

electrons' interactions, we can get the Kohn-Sham potential $V_{\mathrm{KS}}[\rho(\mathbf{r})]$. Thus, the wave-function of single-electron system $\psi_i(\mathbf{r})$ can be obtained by solving Eq. 2.14, where the Hamiltonian is diagonalized to calculate the eigenvalues E_i and eigenvectors $\psi_i(\mathbf{r})$. Next, the ground-state electron density $\rho(\mathbf{r})$ is determined by $\psi_i(\mathbf{r})$ using Eq. 2.15, consequently, a new electron density comes up, denoted as $\rho'(\mathbf{r})$. Compare $\rho'(\mathbf{r})$ with

the initial $\rho(\mathbf{r})$, if they are equal or the difference is small enough to be neglected, we can regard that the correct $\rho(\mathbf{r})$ has been obtained. If not, we would mix the initial guess $\rho(\mathbf{r})$ with $\rho'(\mathbf{r})$, and then a new loop would be started again, until the difference is small enough to get convergent. This process is called as self-consistent-field, as shown in Fig. 2.1.

2.1.6 Exchange correlation functional

In the Hohenberg-Kohn-Sham framework, the problem of solving the many-electron system can be transformed into solving an effective single-electron problem, while the complicated many-electron interations are ascribed to the exchange-correlation potential functional $E_{\mathrm{xc}}[\rho(\mathbf{r})]$. This method is similar to the Hartree-Fock approximation, but the theory is more rigorous than that of the Hartree-Fock approximation. However, the advancements of the Hohenberg-Kohn-Sham framework only make sense when $E_{\mathrm{xc}}[\rho(\mathbf{r})]$ is known. This is the key to solve the second and third questions mentioned at the end of Sec. 2.1.4. In the following, we will discuss the exchange-correlation functional $E_{\mathrm{xc}}[\rho(\mathbf{r})]$.

The exchange-correlation energy can be written as

$$E_{\mathrm{xc}}[\rho(\mathbf{r})] = T[\rho(\mathbf{r})] - T_{\mathrm{s}}[\rho(\mathbf{r})] + E_{\mathrm{int}}[\rho(\mathbf{r})] - E_{\mathrm{Hartree}}[\rho(\mathbf{r})], \tag{2.16}$$

where $T[\rho(\mathbf{r})]$ is the exact many-electron kinetic energy, $T_{\mathrm{s}}[\rho(\mathbf{r})]$ is the non-interacting single-electron kinetic energy. $E_{\mathrm{int}}[\rho(\mathbf{r})]$ is the electron-electron interaction energy, and $E_{\mathrm{Hartree}}[\rho(\mathbf{r})]$ is the Hartree term. The exchange-correlation energy can be expressed in the form of energy density as

$$E_{\mathrm{xc}}[\rho(\mathbf{r})] = \int \mathrm{d}\mathbf{r}\rho(\mathbf{r})\varepsilon_{\mathrm{xc}}[\rho(\mathbf{r})], \tag{2.17}$$

where $\varepsilon_{\mathrm{xc}}[\rho(\mathbf{r})]$ is the exchange-correlation energy density. Then, we can get the exchange-correlation potential as

$$V_{\mathrm{xc}}[\rho(\mathbf{r})] = \frac{\delta E_{\mathrm{xc}}[\rho(\mathbf{r})]}{\delta\rho(\mathbf{r})} \approx \frac{\mathrm{d}}{\mathrm{d}\rho(\mathbf{r})}\left\{\rho(\mathbf{r})\varepsilon_{\mathrm{xc}}[\rho(\mathbf{r})]\right\} = \varepsilon_{\mathrm{xc}}[\rho(\mathbf{r})] + \rho(\mathbf{r})\frac{\mathrm{d}\varepsilon_{\mathrm{xc}}[\rho(\mathbf{r})]}{\mathrm{d}\rho(\mathbf{r})}. \quad (2.18)$$

We introduce two kinds of exchange-correlation approximations. In the simplified condition, homogeneous electron gas can be used as a model of the local density approximation (LDA).[108] In the uniform electron gas, the electron density is a constant, making the exchange-correlation energy density $\varepsilon_{\mathrm{xc}}[\rho(\mathbf{r})]$ a function of electron density, then $\varepsilon_{\mathrm{xc}}[\rho(\mathbf{r})]$ can be solved by Monte Carlo simulation and summarized as a table. After that, by dividing the real non-uniform electron density into infinite small volumes, the electron density in every small volume can be regarded as a constant. According to the $\varepsilon_{\mathrm{xc}}[\rho(\mathbf{r})]$ table, we can get the exchange-correlation energy density of the real system. For the condition where electron density varies rapidly over a small region of space, a better choice could be the generalized gradient approximation (GGA),[109] which depends on the local density as well as the spatial gradient of the density. GGA overcomes deficiencies to a considerable extent, giving more realistic descriptions for many materials.

In summary, based on the Hohenberg-Kohn theorems and Kohn-Sham equation, we can find out the electron density through self-consistent field, describe the kinetic and potential energies using single-electron model, and ascribe the complicated many-electron part to the exchange-correlation term, thus solving all the questions mentioned in Sec. 2.1.4.

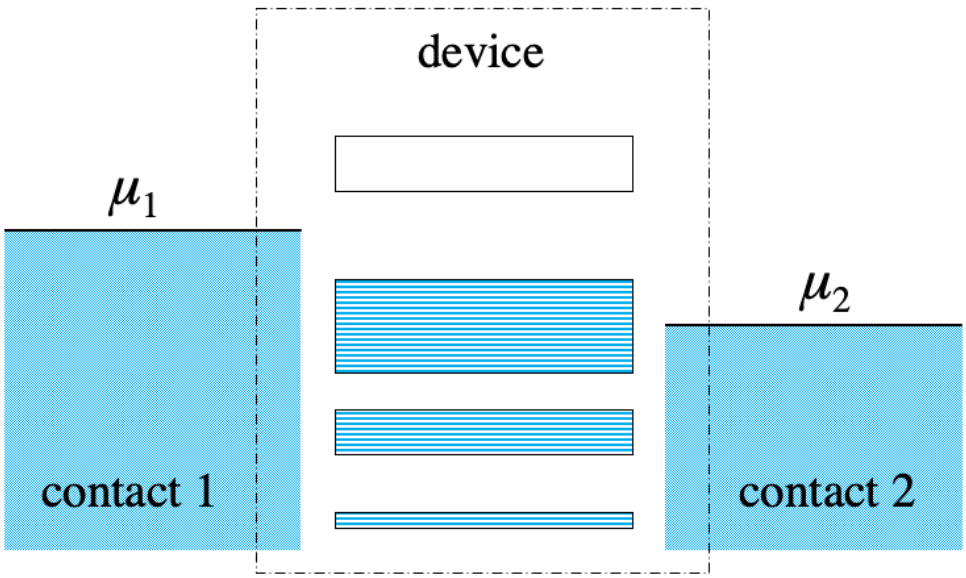

Figure 2.2: Schematic plot of a two-contact device model. μ_1 and μ_2 are the electrochemical potentials of the left/right electrodes. The dashed line box indicates the device region with quantum levels shown as blue lines.

2.2 Non-equilibrium Green's function

Although the density functional theory has been used extensively, it should be noted that Fermi-Dirac statistics can only apply to equilibrium systems, hence the above DFT calculation scheme can not be used for non-equilibrium systems such as those driven by quantum transport. Since treating the non-equilibrium quantum statistics of system goes beyond the standard DFT, in this section, we will discuss how to address this problem by non-equilibrium Green's function (NEGF), as well as the framework of NEGF-DFT.

2.2.1 Two-contact transport model

Figure 2.2 shows the two-contact device model for the quantum transport. The semi-infinite contacts are periodic structures away from the device, and two contacts have different and negative electrochemical potentials μ_1 and μ_2, making the system in non-

equilibrium state. As shown in Fig. 2.2, electrons come from the contact 1, cross the device, and then are transmitted to the contact 2 or reflected back to the contact 1. We assume the transport in the device is coherent. This quantum transport model is the so-called Landauer-Büttiker model.

2.2.2 Green's function

We simplify the quantum transport system into the form of single-electron system, similar to the process in DFT. We use $|\psi\rangle$ in the following to emphasize it is a vector describing electron wavefunction. The Schrödinger equation of the stationary single-electron system is

$$H\,|\psi\rangle = E\,|\psi\rangle\,. \tag{2.19}$$

Dividing the Hamiltonian H and wavefunction $|\psi\rangle$ of the system into contacts and device subspaces, we can get

$$\begin{pmatrix} H_1 & \tau_1 & 0 \\ \tau_1^\dagger & H_d & \tau_2^\dagger \\ 0 & \tau_2 & H_2 \end{pmatrix} \begin{pmatrix} |\psi_1\rangle \\ |\psi_d\rangle \\ |\psi_2\rangle \end{pmatrix} = E \begin{pmatrix} |\psi_1\rangle \\ |\psi_d\rangle \\ |\psi_2\rangle \end{pmatrix}, \tag{2.20}$$

where H_1 and $|\psi_1\rangle$ are for contact 1, H_2 and $|\psi_2\rangle$ are for contact 2, H_d and $|\psi_d\rangle$ are for the device region. $\tau_{1,2}$ describes the interactions between the device and the contacts, and we assume that the contacts are independent, i.e., there is no interaction between contact 1 and contact 2.

Generally, it is easier to calculate Green's function than to solve the whole eigenvalue problem, meanwhile, most properties of the system can be calculated from Green's function, and we would use Green's function to solve Eq. 2.20. The Green's function $G(E)$ is defined as

$$(E - H)G(E) = I, \tag{2.21}$$

and the response to the perturbation $|v\rangle$ can be calculated by the Green's function directly, as

$$|\psi\rangle = -G(E)|v\rangle. \tag{2.22}$$

To make the following contents more intelligible, here we present some additional clarifications of the Green's function. There are two types of solution for Green's function of Eq. 2.21, i.e., the retarded and the advanced Green's functions. In the following, G and $G^\dagger$ denote the retarded Green's function and the advanced Green's function, respectively. Capital G denotes the Green's function of the whole system, lowercase g_1 and g_2 denote Green's functions of isolated contacts.

We start with solving Eq. 2.20. By rearranging the third row of Eq. 2.20 and combining Eq. 2.22, the wavefunction of contact 2 can be written as

$$|\psi_2\rangle = g_2(E)\tau_2 |\psi_d\rangle , \tag{2.23}$$

where g_2 is the Green's function of the isolated contact 2. We can rewrite Eq. 2.20 as

$$\begin{pmatrix} E-H_1 & -\tau_1 & 0 \\ -\tau_1^\dagger & E-H_d & -\tau_2^\dagger \\ 0 & -\tau_2 & E-H_2 \end{pmatrix} \begin{pmatrix} G_1 & G_{1d} & G_{12} \\ G_{d1} & G_d & G_{d2} \\ G_{21} & G_{2d} & G_2 \end{pmatrix} = \begin{pmatrix} I & 0 & 0 \\ 0 & I & 0 \\ 0 & 0 & I \end{pmatrix}. \tag{2.24}$$

Through Eq. 2.24, we can obtain that

$$G_{1d} = g_1\tau_1 G_d,\ G_{2d} = g_2\tau_2 G_d,\ G_d = \left(E - H_d - \Sigma_1 - \Sigma_2\right)^{-1}, \tag{2.25}$$

where $\Sigma_1 = \tau_1^\dagger g_1 \tau_1$ and $\Sigma_2 = \tau_2^\dagger g_2 \tau_2$ are the self energies for contacts 1 and 2, respectively. On the other hand, for any perturbation $|v\rangle$, we can get two solutions, $|\psi^R\rangle$

and $|\psi^A\rangle$, to the perturbed Schrödinger equation

$$(E - H)|\psi\rangle = -|v\rangle, \tag{2.26}$$

with the definition of $\left|\psi^R\right\rangle$ and $\left|\psi^A\right\rangle$ as

$$|\psi_R\rangle = -G|v\rangle, |\psi_A\rangle = -G^\dagger|v\rangle. \tag{2.27}$$

Then we can get

$$(E - H)(|\psi_R\rangle - |\psi_A\rangle) = (E - H)\left(G - G^\dagger\right)|v\rangle = (I - I)|v\rangle = 0. \tag{2.28}$$

Define the spectral function as

$$A = i\left(G - G^\dagger\right). \tag{2.29}$$

Consequently, it can be seen that $|\psi\rangle = A\,|v\rangle$ is the solution to Schrödinger equation for any perturbation $|v\rangle$. The specific form of Green's function can be written as

$$G = \frac{1}{E + i\delta - H} = \sum_k \frac{|k\rangle\langle k|}{E + i\delta - \epsilon_k}, \tag{2.30}$$

where $i\delta$ is the small imaginary part, $|k\rangle$ denotes all eigenvectors to H with corresponding eigenvalues ϵ_k. Meanwhile, the spectral function can be written as

$$A = \sum_k |k\rangle\langle k| \frac{2\delta}{(E - \epsilon_k)^2 + \delta^2} \overset{\delta\to 0}{=} 2\pi \sum_k \delta(E - \epsilon_k)|k\rangle\langle k|. \tag{2.31}$$

Equation 2.31 illustrates that the spectral function A gives all solutions to the Schrödinger equation.

2.2.3 Response to an incoming wave

In the stationary case, the isolated contact 1 has the solutions corresponding to incoming waves which are totally reflected at the contact end. These solutions are denoted by $|\psi_{1,n}\rangle$ where 1 is the contact number and n is the index of the coming wave. We use a_1 to denote the spectral function of the isolated contact. All solutions including eigenvalues and eigenvectors can be found in a_1.

In the non-equilibrium case, contacts with different electrochemical potentials will inject electrons into the device. Therefore, we want to find out the solutions corresponding to these incoming waves. After connecting the contact 1 to the device, the wavefunction of the whole system is $|\psi_{1,n}\rangle + |\psi^R\rangle$, where $|\psi_{1,n}\rangle$ is localized in the contact 1. We assume that $|\psi_{1,n}\rangle$ is the solution of $\tau_1 |\psi_{1,n}\rangle = (E - H_1) |\psi_{1,n}\rangle$ and regard $|\psi^R\rangle$ as the retarded response to $|\psi_{1,n}\rangle$ spreading over the whole system. By applying this wavefunction to Schrödinger equation and combining Eq. 2.20, we can get

$$\begin{aligned}(H_1 + \tau_1 + H_d + \tau_1^\dagger + \tau_2^\dagger + H_2 + \tau_2)(|\psi_{1,n}\rangle + |\psi^R\rangle) = E(|\psi_{1,n}\rangle + |\psi^R\rangle),\\ (H - E) |\psi^R\rangle = -\tau_1^\dagger |\psi_{1,n}\rangle.\end{aligned} \tag{2.32}$$

Equation 2.32 shows that $|\psi^R\rangle$ is the response of the whole system to a perturbation of $-\tau_1^\dagger |\psi_{1,n}\rangle$, and Eq. 2.32 can be rewrite as

$$|\psi^R\rangle = G\tau_1^\dagger |\psi_{1,n}\rangle . \tag{2.33}$$

For the device part, the wavefunction $|\psi_d\rangle$ is

$$|\psi_d\rangle = G_d\tau_1^\dagger |\psi_{1,n}\rangle . \tag{2.34}$$

For the contact 2, the wavefunction $|\psi_2\rangle$ is

$$|\psi_2\rangle = g_2\tau_2 |\psi_d\rangle = g_2\tau_2 G_d \tau_1^\dagger |\psi_{1,n}\rangle . \tag{2.35}$$

For the contact 1, we need to add the incoming wavefunction, as

$$|\psi_1\rangle = (1 + g_1\tau_1 G_d \tau_1^\dagger) |\psi_{1,n}\rangle . \tag{2.36}$$

Through DFT, we can use self-consistent field to describe the change of electron density caused by the non-equilibrium condition. Consequently, we are interested in the electron density matrix, which is defined as

$$\rho = \sum_n f(E_n, \mu) |\psi_n\rangle \langle\psi_n| , \tag{2.37}$$

where $f(E_n, \mu_1)$ is the Fermi-Dirac function with the electrochemical potential μ_1.

The wavefunction of the device is given by an incoming wave in contact 1, as

$$|\psi_{d,n}\rangle = G_d \tau_1^\dagger |\psi_{1,n}\rangle . \tag{2.38}$$

Adding up all states from contact 1 and considering Eq. 2.31, we can obtain $\rho_{d,1}$, which is the change of device electron density matrix caused by $|\psi_{1,n}\rangle$

$$\begin{aligned} \rho_{d,1} &= \int_{-\infty}^{\infty} \mathrm{d}E \sum_n f(E, \mu_1)\delta(E - E_n) |\psi_{d,n}\rangle \langle\psi_{d,n}| \\ &= \int_{-\infty}^{\infty} \mathrm{d}E f(E, \mu_1) G_d \tau_1^\dagger \frac{a_1}{2\pi} \tau_1 G_d^\dagger \\ &= \frac{1}{2\pi} \int_{-\infty}^{\infty} \mathrm{d}E f(E, \mu_1) G_d \Gamma_1 G_d^\dagger . \end{aligned} \tag{2.39}$$

where $\Gamma_1 = \tau_1^\dagger a_1 \tau_1 = i(\Sigma_1 - \Sigma_1^\dagger)$. Then we have

$$\rho = \frac{1}{2\pi}\int_{-\infty}^{\infty} \mathrm{d}E \sum_{i=1,2} f(E,\mu_i) G_d \Gamma_i G_d^\dagger. \tag{2.40}$$

2.2.4 Electric current

For a steady state, the probability to find an electron in the device is conserved. Due to the conservation of the wave function, we can have

$$\begin{aligned} 0 &= \frac{\partial \sum_i |\psi_i|^2}{\partial t} \\ &= i\left(\left[\langle\psi_1|\tau_1|\psi_d\rangle - \langle\psi_d|\tau_1^\dagger|\psi_1\rangle\right] + \left[\langle\psi_2|\tau_2|\psi_d\rangle - \langle\psi_d|\tau_2^\dagger|\psi_2\rangle\right]\right). \end{aligned} \tag{2.41}$$

Here, $\sum_i |\psi_i|^2$ is the wave function summed over the device, i is the basis of wavefunctions, and $|i\rangle\langle i|$ can be used as the projection operator. We interpret the term in the first square bracket as the incoming probability current into the device from contact 1 and the second bracket from contact 2. Generalizing to an arbitrary contact j, and using electron $-e$ to multiply the probability current, we get the electric current as (physical constants have been omitted for simplification)

$$i_j = -i(\langle\psi_j|\tau_j|\psi_d\rangle - \langle\psi_d|\tau_j^\dagger|\psi_j\rangle),\ j = 1,2. \tag{2.42}$$

Take the electrical current from contact 1 to contact 2 as an example, we have

$$i_{\text{from 1 to 2}} = -i(\langle\psi_2|\tau_2|\psi_d\rangle - \langle\psi_d|\tau_2^\dagger|\psi_2\rangle). \tag{2.43}$$

Considering Eq. 2.25, Eq. 2.43 turns to be

$$i_{\text{from 1 to 2}} = \langle\psi_{1,n}|\tau_1 G_d^\dagger \Gamma_2 G_d \tau_1^\dagger|\psi_{1,n}\rangle, \tag{2.44}$$

where $\Gamma_2 = \tau_2^\dagger(g_2^\dagger - g_2)\tau_2$ under the non-equilibrium state. Adding all the energy levels n filled in the device, it gives (2 for spin)

$$\begin{aligned} I_{\text{from 1 to 2}} &= \int_{E=-\infty}^{\infty} \mathrm{d}E f(E,\mu_1) \sum_n \delta\left(E - E_n\right) \langle\psi_{1,n}|\tau_1 G_d^\dagger \Gamma_2 G_d \tau_1^\dagger|\psi_{1,n}\rangle \\ &= \frac{1}{2\pi}\int_{E=-\infty}^{\infty} \mathrm{d}E f(E,\mu_1)\,\mathrm{Tr}(G_d^\dagger\Gamma_2 G_d \Gamma_1) \end{aligned} \tag{2.45}$$

To get the total current through the device, the current from contact 2 to contact 1 have to be subtracted away. Then we can get the Landauer formula for current, as

$$I = I_{\text{from 1 to 2}} - I_{\text{from 2 to 1}} = \frac{1}{\pi}\int_{-\infty}^{\infty} \mathrm{d}E[f(E,\mu_1) - f(E,\mu_2)]\,\mathrm{Tr}(G_d^\dagger\Gamma_2 G_d\Gamma_1). \tag{2.46}$$

At the end of this section, we would briefly summarize how to calculate the electrical current with NEGF-DFT method in Fig. 2.3. Firstly, we give an initial guess for the electron density of device $\rho(\mathbf{r})$, after that, $V_{\text{KS}}[\rho(\mathbf{r})]$ can be calculated. Thus, the Hamiltonian matrix $H[\rho(\mathbf{r})]$ of the device is known, and then, the Green's function of the device can be calculated with self energies Σ_1 and Σ_2. A new electron density can be obtained using Green's function, denoted as $\rho'(\mathbf{r})$. Compare $\rho'(\mathbf{r})$ with the initial $\rho(\mathbf{r})$, if they are equal or the difference is small enough to be neglected, we can regard that the exact $\rho(\mathbf{r})$ has been obtained. If not, we would mix the initial guess $\rho(\mathbf{r})$ with the new electron density $\rho'(\mathbf{r})$, and then a new loop would be started again until the difference is small enough to get self-consistent. Using the exact $\rho(\mathbf{r})$, we output Green's function, which can be used for calculations of transport properties.

2.3 Summary

In this chapter, we introduce the basic concepts of density functional theory and quantum transport theory. In Hohenberg-Kohn-Sham framework, the electron density

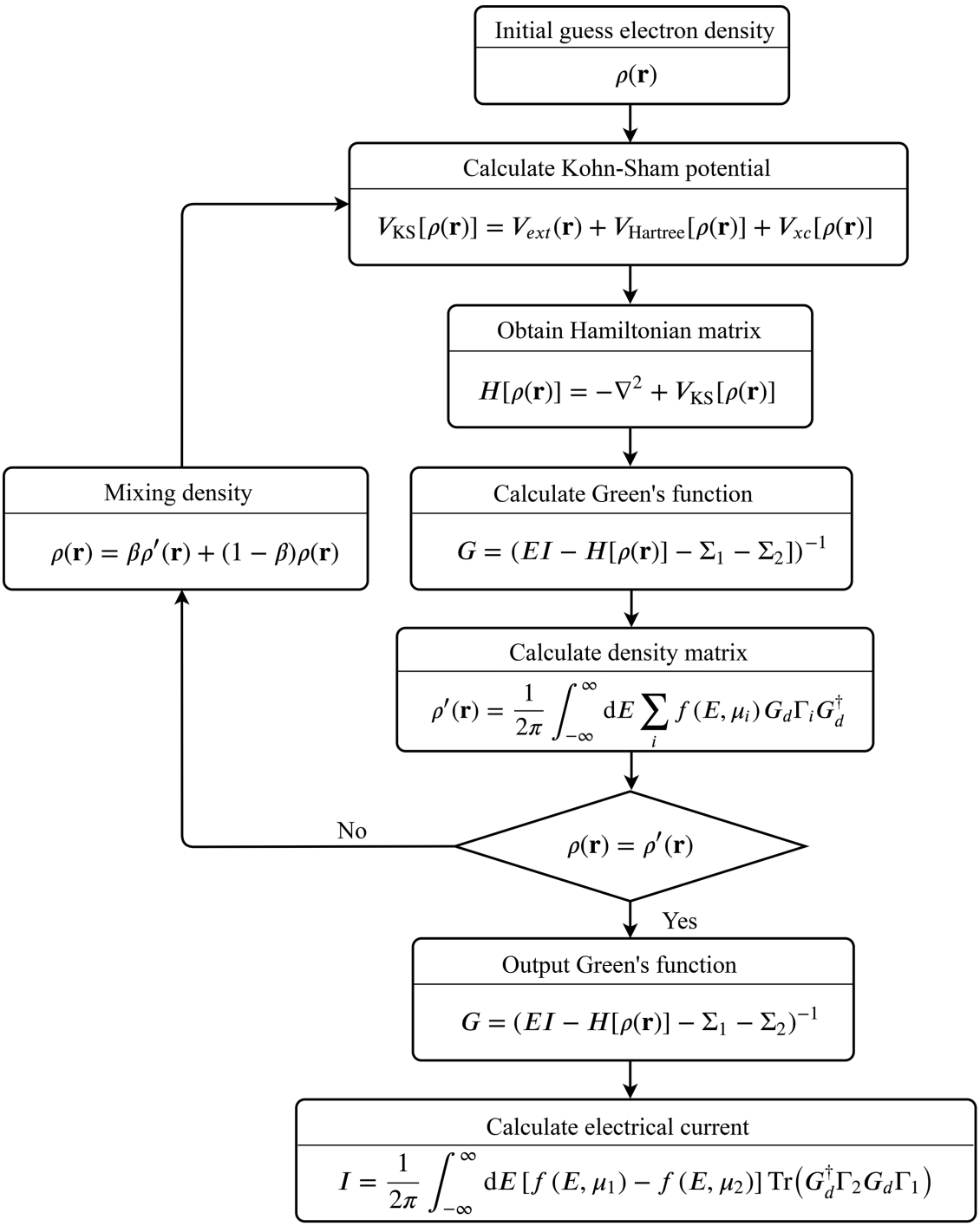

Figure 2.3: Flow chart of electrical current calculation through NEGF-DFT method.

is the fundamental quantity to determine the physical properties. The Green's function can be used for transport calculations. In the NEGF-DFT workflow, Hamiltonian

determined by the electron density can be used to construct the Green's function, which can output a new electron density. The SCF method can be employed to get an exact solution of the electron density, to further calculate transport properties.

Chapter 3

TMR and SHE modulations by heavy metals

3.1 Introduction

Basic functionalities of MTJ device involve reading and writing operations, which employ TMR and STT/SOT effects, respectively. Great efforts have been devoted to the enhancement of TMR to improve the reading reliability,[11] and SOT switching is increasingly attracting attention due to its superiority such as low-power consumption and high speed.[85, 110]

Recently, many experimental works have reported that HM layers in MTJs can noticeably modulate TMR.[11, 51, 111, 112] This modulation effect is usually attributed to the HM atoms diffusion which affects the crystallization of MgO, while the intrinsic influence caused by HMs is often neglected. There is no doubt that the existence of HMs would change the electronic structures of MTJs, hence impacting the transport properties, i.e. spin-polarized reading current and subsequent TMR ratio. However, despite abundant achievements in experiments, theoretical investigations on essential influence caused by HMs remain quite inadequate. To improve TMR ratio

furthermore, it is urgently required to fundamentally understand the mechanism of TMR modulation caused by HMs, and figure out desirable HMs to achieve the TMR optimization.

On the other hand, many works have reported various SOT threshold current densities in devices with different HMs,[71, 86, 113, 114] demonstrating that HMs in SOT devices play an important role in the modulation of power dissipation. To further reduce the energy consumption, HMs with strong SHE and large SHA are highly desired, since SOT can be induced by SHE [10, 71] and the threshold SOT current density is inversely proportional to SHA.[115] Consequently, figuring out HMs with remarkable SHE and SHA as well as the method to improve spin Hall properties have great significance for the performance of SOT devices.

To optimize the reading and writing processes of MTJs, in this chapter, we will investigate the mechanisms of TMR and SHE modulation induced by heavy metals, and discuss the optimization of TMR and SHE enhancement.

3.2 Atomic model and method

The MTJ model is shown in Fig. 3.1, composed of HM/CoFe/MgO/CoFe/HM structure, where CoFe has the 1:1 composition. We use symmetric structures, i.e. both free layer and reference layer consist of 5 monolayers of CoFe, and identical heavy metals are used as capping and seed layers. MgO of 5 monolayers, around 1 nm in thickness, is employed as the tunnel layer. Layers are stacked along z direction, while the periodic boundary condition is satisfied along x and y directions. After investigating experimental works,[46, 49, 71, 113] we choose extensively used HMs including Ta, W, Mo, and Ir in the face-centered-cubic (fcc) structures and with lattice constants of 4.22 Å, 4.06 Å, 4.03 Å, and 3.90 Å, respectively.[116] The CoFe/HM interfaces are matched by rotating HM by 45° in xy-plane,[117] and the in-plane lattice constant

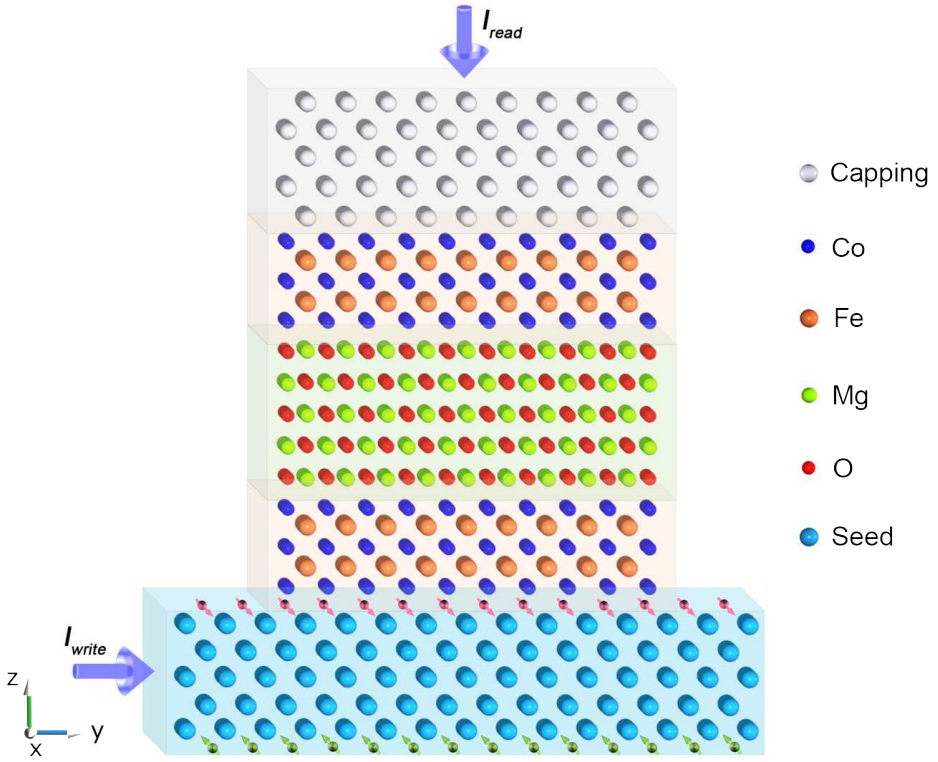

Figure 3.1: Schematic structure of the three-terminal MTJ. Capping layer and seed layers are composed by the same heavy metal.

of all MTJs is fixed to 2.83 Å according to the lattice constant of CoFe.[118] Atomic structures of the MTJs have been optimized by Vienna *Ab initio* Simulation Package (VASP) [119–121] using a cutoff energy of 520 eV, a $\boldsymbol{k}$-mesh of $31 \times 31 \times 1$, and a force convergence criterion of 0.01 eV/Å. In the following, we use HM-MTJ to denote the MTJ with HM as capping and seed layers.

Quantum transport properties were calculated by NanoDCAL package,[122, 123] which is in the framework of non-equilibrium Green's function combined with density functional theory (NEGF-DFT). Spin-dependent conductance can be derived by Landauer-Büttiker formula

$$G_\sigma = \frac{e^2}{h} \sum_{\boldsymbol{k}_{||}} T_\sigma(\boldsymbol{k}_{||}, E_F), \tag{3.1}$$

where σ represents the spin index, and $T_\sigma(\boldsymbol{k}_{||}, E_F)$ denotes the σ-spin transmission coefficient at $\boldsymbol{k}_{||} = (k_x, k_y)$. E_F is the Fermi energy, e denotes the elementary charge and h is Planck constant. A $20 \times 20 \times 1$ $\boldsymbol{k}$-mesh was adopted in the self-consistent calculation, and a dense $\boldsymbol{k}$-mesh of $300 \times 300 \times 1$ was employed in transmission calculation.

We calculated the intrinsic spin Hall conductivity of various HMs. QUANTUM ESPRESSO package was employed for the *ab initio* calculations [124] with a $\boldsymbol{k}$-mesh of $10 \times 10 \times 10$ in self-consistent calculations. Then, DFT wavefunctions were transformed to maximally localized Wannier functions using WANNIER90 package.[125, 126] SHC calculations employed Kubo formula Eq. 1.2, which indicates that SHC is the integral over all occupied bands as

$$\sigma_{yz}^{x} = -\frac{e^2}{\hbar}\frac{1}{VN_k^3}\sum_{\boldsymbol{k}}\Omega_{yz}^{x}(\boldsymbol{k}), \tag{3.2}$$

where the $\boldsymbol{k}$-resolved term is the spin Berry curvature. More details about the calculation method can be found in our previous work.[81] A dense $200\times200\times200$ $\boldsymbol{k}$-mesh and the adaptive mesh refinement were adopted to deal with the rapid variation of the spin Berry curvature in BZ. The Perdew-Burke-Ernzerhof generalized gradient approximation (PBE-GGA) exchange-correlation potential [109] was used in all calculations.

3.3 Influence on TMR caused by heavy metals

In this section, we will discuss TMR effects in MTJs with different heavy metals including Ta, W, Mo, and Ir. Different from experimental works which attribute the impact on TMR to the diffusion of HM atoms,[52, 127–129] in this section, we would study the intrinsic influence on TMR in terms of transmission channels and band structures of HMs .

3.3.1 Transmission channels

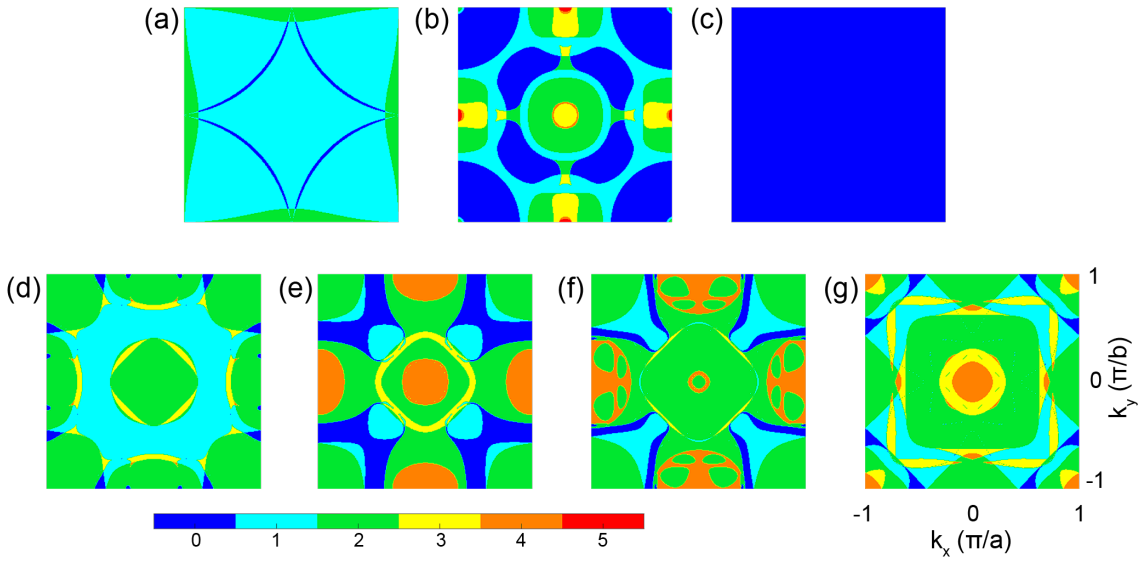

Figure 3.2: 2D transmission channel spectra along z direction of (a) majority-spin CoFe, (b) minority-spin CoFe, (c) MgO, (d) Ta, (e) W, (f) Mo, and (g) Ir. Colorbar indicates the number of transmission channel.

Firstly, we show the transmission channel spectra in 2D BZ of different materials in Fig. 3.2. The transmission channel was calculated by counting the number of Bloch waves existing in the material and propagating along z direction. It can be observed in Figs. 3.2(a)-(b) that the majority-spin CoFe exhibits extensive open regions, while the minority-spin component suppresses transmission in most parts. Zero-channel MgO in Fig. 3.2(c) indicates the tunneling transport in MTJs. Different HMs exhibit diverse transmission channel spectra in Figs. 3.2(d)-(g), and open transmission fractions would influence the outlines of transmission spectra.

3.3.2 Spin-dependent conductance and TMR

We calculated the spin-resolved conductance of Ta-MTJ, W-MTJ, Mo-MTJ, and Ir-MTJ, and present the result in Fig. 3.3. There are four channels in each MTJ, i.e., $G^{\uparrow}_{PC}$, $G^{\downarrow}_{PC}$, and $G^{\uparrow}_{APC}$ which is the same as $G^{\downarrow}_{APC}$ due to the structural symmetry. We

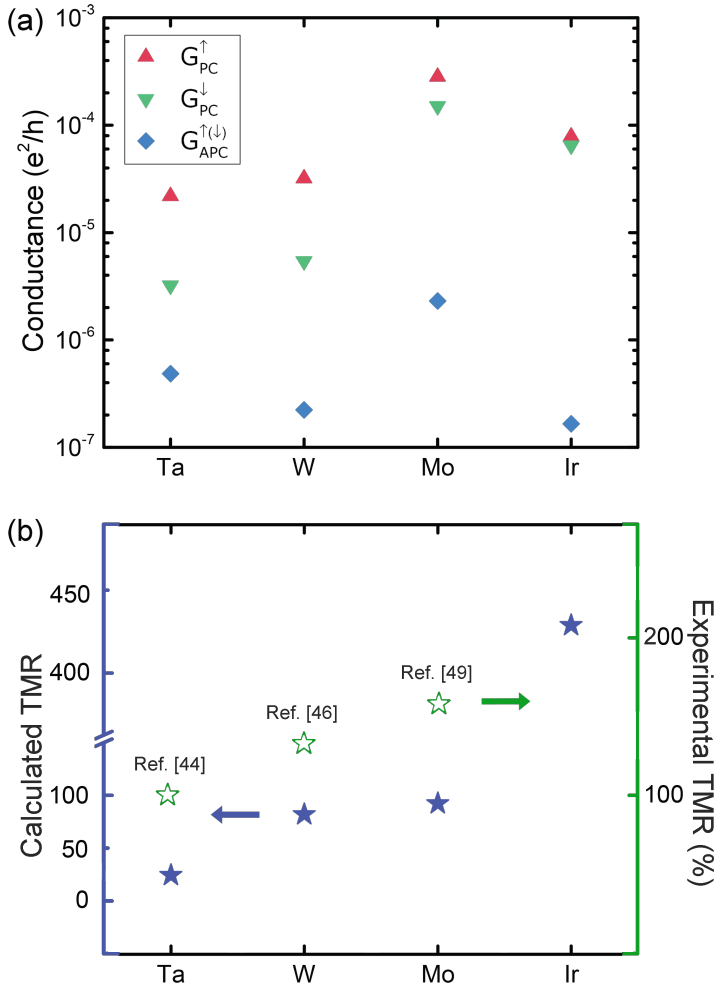

Figure 3.3: (a) Spin-resolved conductance. (b) TMR of MTJs with different heavy metals as shown in the horizontal axis. The blue stars denote our calculated results corresponding to the left vertical axis, and the green stars indicate the experimental reports corresponding to the right vertical axis.

define TMR $= \frac{G_{PC}-G_{APC}}{G_{APC}}$, where $G_{PC} = G^{\uparrow}_{PC} + G^{\downarrow}_{PC}$ and $G_{APC} = G^{\uparrow}_{APC} + G^{\downarrow}_{APC}$. It is obvious that MTJs with different HMs vary a lot in the aspect of conductance and the subsequent TMR. Compared to Ta-MTJ, W-MTJ has higher TMR due to its low G_{APC}, and Mo-MTJ also exhibits a remarkable TMR thanks to its high G_{PC}. More intriguingly, Ir-MTJ presents a TMR four times as large as that of Mo-MTJ, and the reason can be attributed to the high G_{PC} and ultralow G_{APC} in Ir-MTJ. Except the absence of experiment on Ir-MTJ, our results are qualitatively corresponding to

previous experimental reports, i.e., W-MTJ and Mo-MTJ has higher TMR than Ta-MTJ,[44, 46, 49] as shown by green stars in Fig. 3.3(b). Our work indicates that W, Mo, and Ir can be promising candidates as HMs of MTJ for high TMR.

3.3.3 Analyses of transmission spectra

According to Eq. 3.1, conductance is the integral of all transmission coefficients in 2D BZ. To analyze the conductance, we studied the spin-resolved transmission spectra, as shown in Fig. 3.4. The first and the second columns are the majority-spin and minority-spin transmissions in PC, respectively, and the last column is the majority-(minority-) spin transmission in APC. Four rows correspond to four MTJs with Ta, W, Mo, and Ir layers. We use the red and blue colors to denote the high and low transmission probabilities, respectively. As reported in previous work,[31] in the MTJ consisting of Fe/MgO/Fe stack, there is a broad peak at the center of 2D BZ in the majority-spin channel. This phenomenon is attributed to the low decay rate of Δ_1 states, as introduced in Sec. 1.2.1. For MTJs with HMs, Ta-, W-, and Ir-MTJs present centered broad peaks, which contribute dominantly to $G_{PC}^{\uparrow}$. Moreover, compared to those of Ta- and W-MTJs, the peak of Ir-MTJ is more prominent as shown in Fig. 3.4(j) by the red color, leading to the high $G_{PC}^{\uparrow}$ of Ir-MTJ. Combining the ultralow G_{APC}, Ir-MTJ realizes the highest TMR among all MTJs. On the other hand, as shown in Fig. 3.4(g), it is distinctive that the centered peak disappears in $T_{PC}^{\uparrow}$ of Mo-MTJ. Meanwhile, transmissions augment in a centered ring, leading to a high $G_{PC}^{\uparrow}$ of Mo-MTJ.

To understand the unusual transmission spectrum of Mo-MTJ shown in Fig. 3.4(g), we study the band structures of four metals, as shown in Fig. 3.5. Bands are plotted along Γ-Z direction, and Δ_1 states containing s, p_z, d_{z^2} orbitals are projected. It can be observed that Δ_1 bands cross the Fermi energy in Ta, W, and Ir. However, the Δ_1

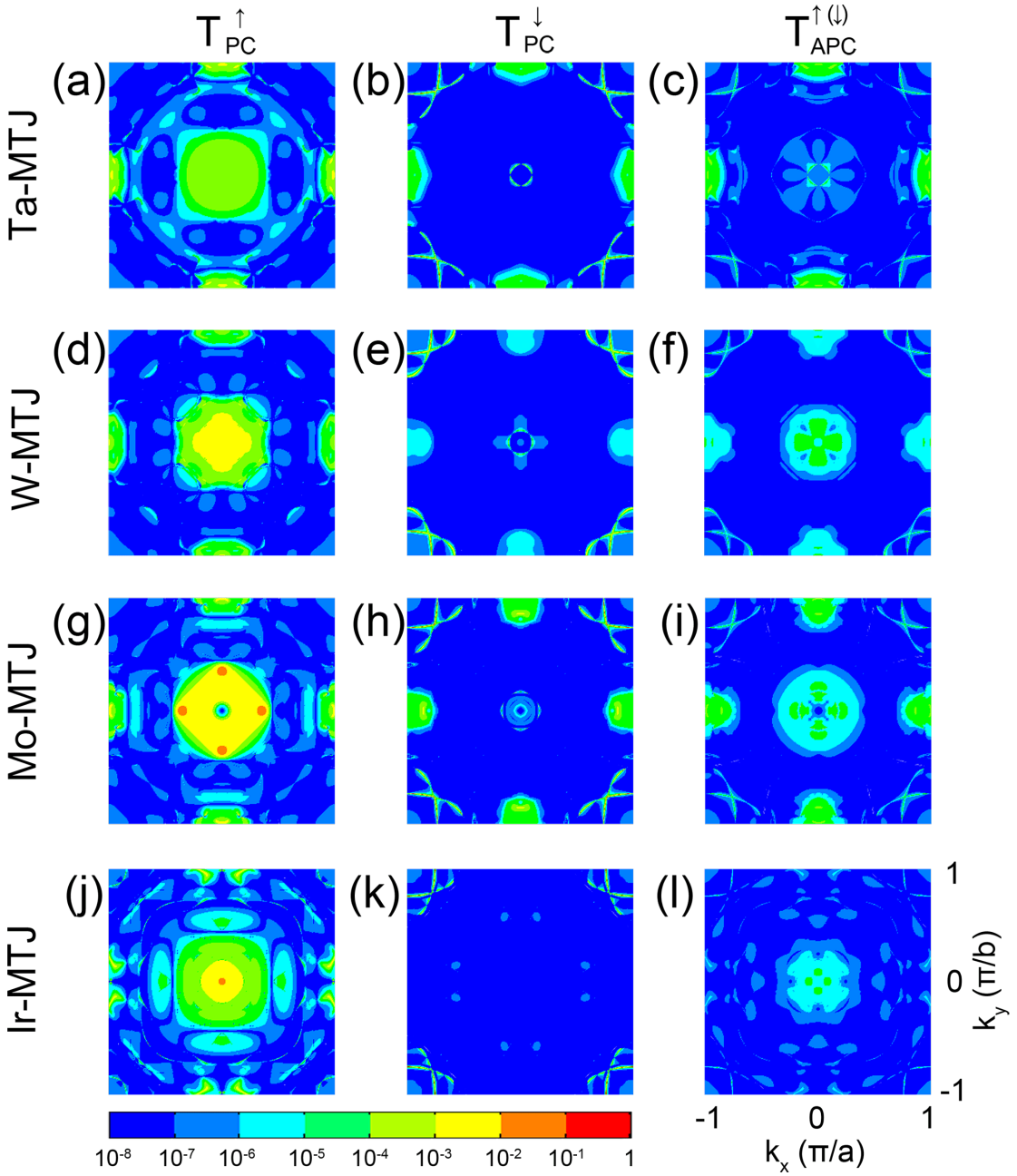

Figure 3.4: Spin- and 2D $\boldsymbol{k}_{||}$-resolved transmission spectra of MTJs capped by diverse heavy metals. Colorbar indicates the transmission coefficients.

band of Mo has no intersection with E_F. Since the Δ_1 states play a determined role in the transmission peak at $\boldsymbol{k}_{||} = (0, 0)$, we conclude that the disappearance of centered peak in Fig. 3.4(g) can be attributed to the absence of Δ_1 states crossing the Fermi energy of Mo metal.

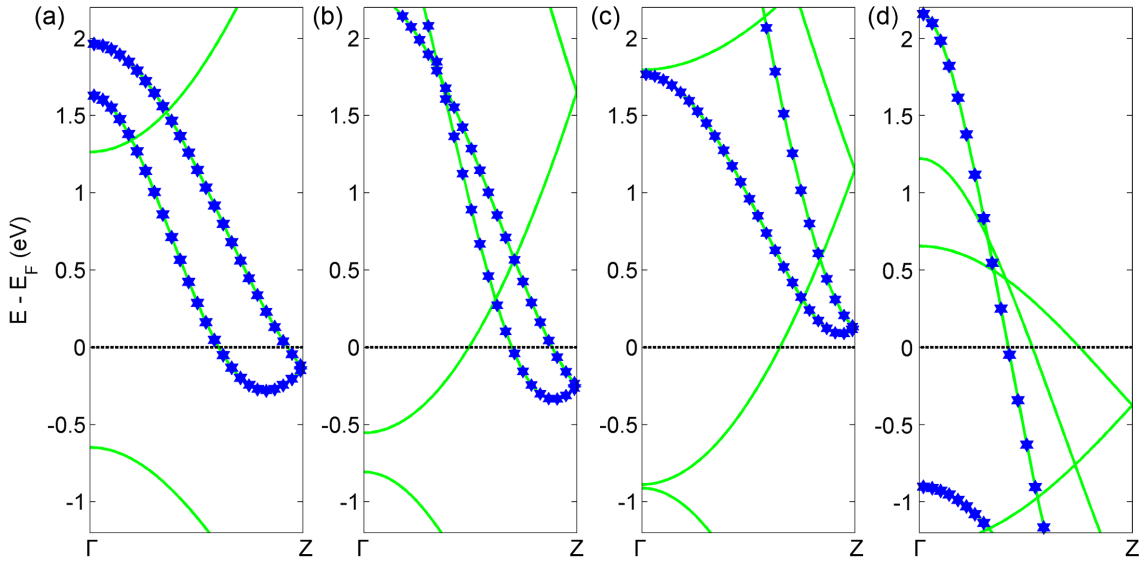

Figure 3.5: Band structures of different heavy metals along Γ-Z direction. (a) Ta. (b) W. (c) Mo. (d) Ir. Δ_1 bands have been projected by Blue stars.

On the other hand, Fig. 3.3(a) shows that Mo-MTJ presents the highest $G_{PC}^{\downarrow}$ among all MTJs. Through observing the transmission spectrum $T_{PC}^{\downarrow}$ carefully, we find that Fig. 3.4(h) shows some very sharp transmissions at corners of 2D BZ, indicated by some red point. We measured the value of ultrahigh transmission coefficients in this tiny fraction, and we find that the highest one is $T_{PC}^{\downarrow} = 0.8991$ at $\boldsymbol{k}_{||} = (0.526, 0.900)$. Since the transmission coefficient is close to unity, we infer that it is caused by the interfacial resonant states, and the ultrahigh transmission peaks are called "hot spots".[31] Hot spots can be understood by the formation of bonding and antibonding hybrids between the interfacial states on both sides of the barrier, and electrons could tunnel through the barrier with no or little attenuation.[130] When the barrier thickness is broadened, the coupling between the interfacial resonances attenuate and disappear, then normal tunneling transport with high decay rate and low transmission coefficient happen.[131] In our work, the minority-spin channel is dominated by the interfacial resonant states due to the thin tunnel layer. Actually, Fig. 3.4 shows that for all MTJs, hot spots occur in minority-spin channels with diverse

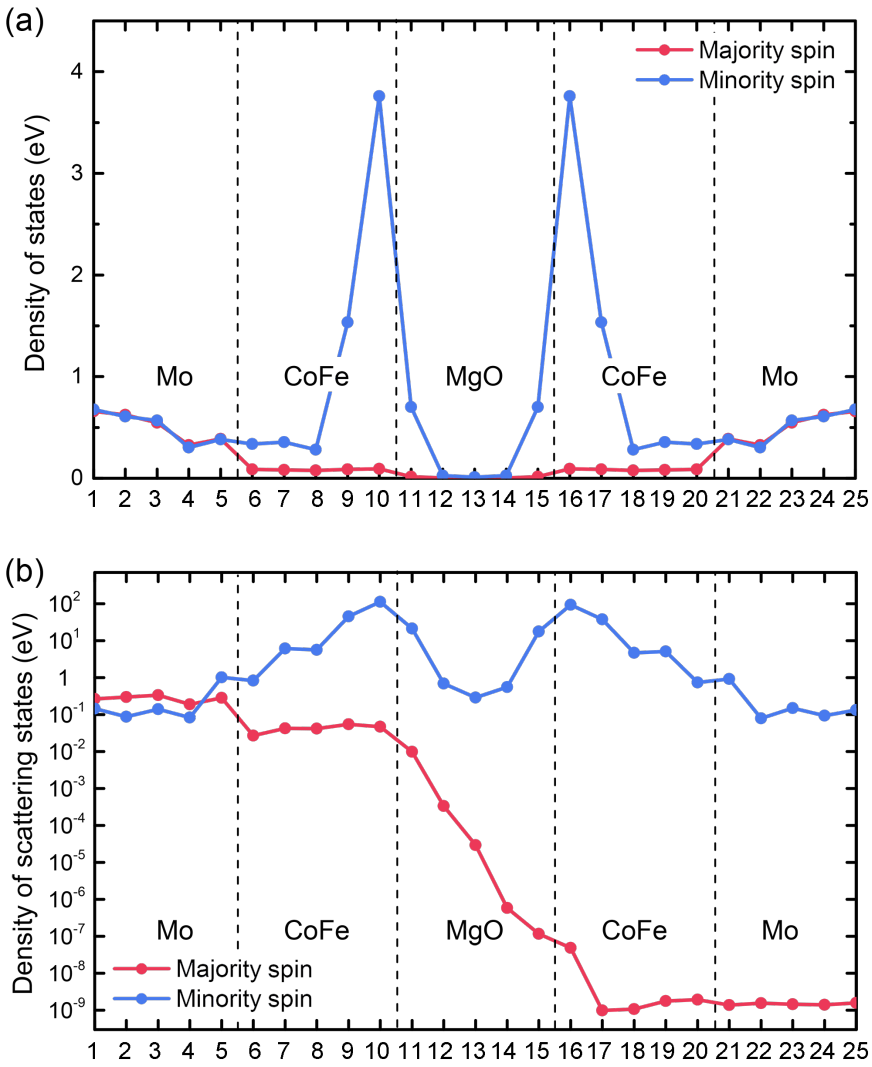

Figure 3.6: Spin- and layer-resolved (a) density of states and (b) density of scattering states of parallel Mo-MTJ on the transmission peak of $\boldsymbol{k}_{||} = (0.526, 0.900)$.

amplitudes. Note that hot spots are very sensitive to the interface roughness and the symmetry of junction.[32] From this perspective, an ideal symmetric MTJ would strengthen TMR effect.

Figure 3.6 validates our discussions on interfacial resonant states. Density of states (DOS) and density of scattering states (DOSS) of Mo-MTJ projected on $\boldsymbol{k}_{||} = (0.526, 0.900)$ are shown in Figs. 3.6(a) and (b), respectively. Fig. 3.6(a) shows that in Mo layers, the majority-spin and minority-spin DOS overlap since Mo is nonmag-

netic. The minority-spin DOS are strongly localized at both CoFe/MgO interfaces, indicating the existence of interfacial resonant states which yield huge wavefunction amplitudes. Figure 3.6(b) presents DOSS at $\boldsymbol{k}_{||} = (0.526, 0.900)$, where transmission coefficients are $T^{\uparrow}_{PC} = 1.28 \times 10^{-8}$ and $T^{\downarrow}_{PC} = 0.8991$, respectively. It shows that the majority-spin DOSS decay rapidly, while the minority-spin DOSS present negligible attenuation, verifying the occurrences of interfacial resonant states and resonant tunneling transport.

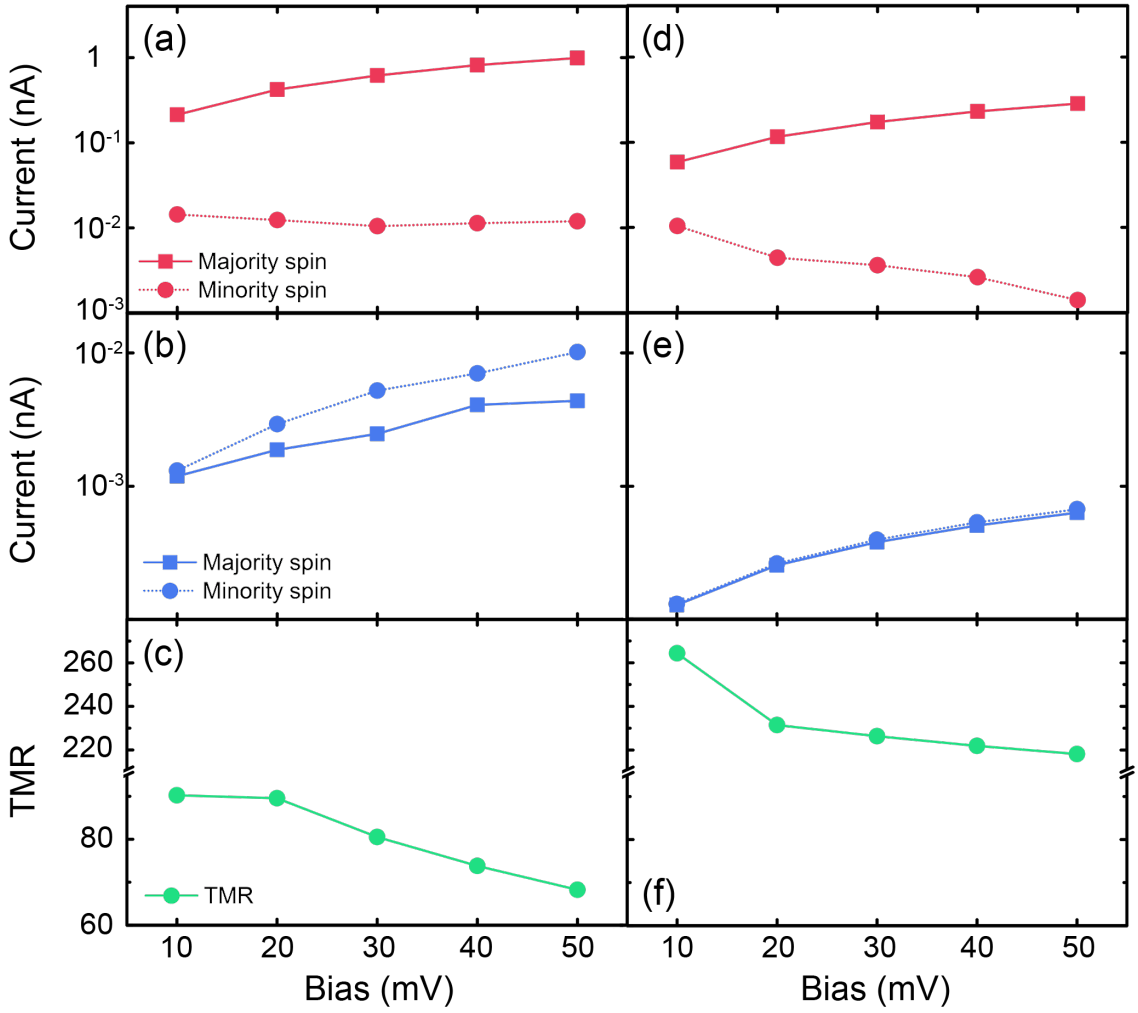

Figure 3.7: Non-equilibrium transport properties. The left column is for Mo-MTJ, and the right column is for Ir-MTJ. (a) and (d) are the currents in PC. (b) and (e) are the currents in APC. (c) and (f) are the TMRs.

3.3.4 TMR under bias

Figure 3.7 presents TMR in non-equilibrium states, where TMR = $\frac{I_{PC}-I_{APC}}{I_{APC}}$, $I_{PC} = I^{\uparrow}_{PC} + I^{\downarrow}_{PC}$, and $I_{APC} = I^{\uparrow}_{APC} + I^{\downarrow}_{APC}$. The left column is for Mo-MTJ, while the right column is for Ir-MTJ. It can be observed that $I^{\uparrow}_{PC}$, $I^{\uparrow}_{APC}$ and $I^{\downarrow}_{APC}$ are rising with increasing bias, while $I^{\downarrow}_{PC}$ and TMRs decline with increasing bias. Compared with the value at equilibrium state, TMR of Mo-MTJ is reduced by 30% at bias of 50 mV, and that of Ir-MTJ is reduced by 18% at bias of 50 mV. The falling TMR can be partly attributed to the decline of minority-spin current in PC. Since $I^{\downarrow}_{PC}$ is mainly contributed by the interfacial resonant states which would be greatly impacted and destructed by the bias condition, $I^{\downarrow}_{PC}$ decreases in both Mo-MTJ and Ir-MTJ with rising bias, leading to the reduction of I_{PC} and TMR.

3.4 SHE of HMs and alloys

In this section, we will discuss SHE of HMs which can induce SOT and achieve switching of MTJ. Since the spin Hall conductivity of Ta and W has been reported,[81, 132] we investigate the SHC of HMs including Mo and Ir, as well as the realization of SHC enhancement through substitutional doping.

3.4.1 SHC of Mo

Figure 3.8 shows the energy-resolved SHC of Mo metal, inset is the primitive cell we used in calculations. By tuning the position of Fermi energy, SHC changes a lot in both magnitude and sign. Figure 3.8 shows that SHC of Mo is negative, to be exact, SHC = -412 $(\hbar/e)$S/cm at E_F. There is a small peak near the Fermi energy, i.e. SHC = -841 $(\hbar/e)$S/cm at $E = E_F - 0.3$ eV. Moreover, a larger SHC up to 1230 $(\hbar/e)$S/cm can be found at $E = E_F + 3.82$ eV.

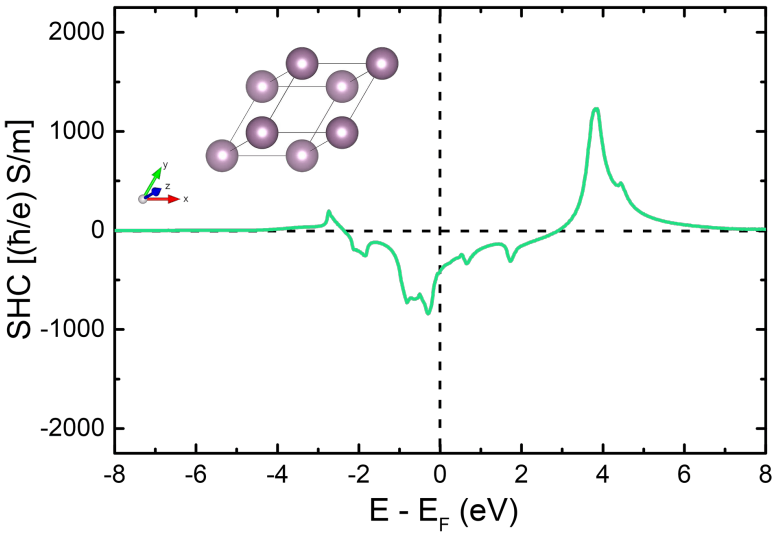

Figure 3.8: Energy-resolved SHC of Mo metal, inset is the structure of primitive cell.

To elucidate the underlying mechanism of the of SHC, we show the band structure projected by spin Berry curvature. We firstly introduce the concept of spin Berry curvature. The Kubo formula for SHC calculation is given by [133, 134]

$$\sigma_{yz}^{x} = -\frac{e^2}{\hbar}\frac{1}{VN_k^3}\sum_{\boldsymbol{k}}\Omega_{yz}^{x}(\boldsymbol{k}), \tag{3.3}$$

where the $\boldsymbol{k}$-resolved term is the spin Berry curvature. It is defined as

$$\Omega_{yz}^{x}(\boldsymbol{k}) = \sum_{n} f_{n\boldsymbol{k}}\Omega_{n,yz}^{x}(\boldsymbol{k}), \tag{3.4}$$

and the band-projected spin Berry curvature term is

$$\Omega_{n,yz}^{x}(\boldsymbol{k}) = \hbar^2\sum_{m\neq n}\frac{-2\,\mathrm{Im}[\langle n\boldsymbol{k}|\frac{1}{2}\{\hat{\sigma}_x,\hat{v}_y\}|m\boldsymbol{k}\rangle\langle m\boldsymbol{k}|\hat{v}_z|n\boldsymbol{k}\rangle]}{(\epsilon_{n\boldsymbol{k}}-\epsilon_{m\boldsymbol{k}})^2}. \tag{3.5}$$

We discuss SHC in the aspect of the spin Berry curvature, $\Omega_{yz}^{x}(\boldsymbol{k})$. Figure 3.9 presents analyses of spin Berry curvature of Mo. Figure 3.9(a) shows the band-

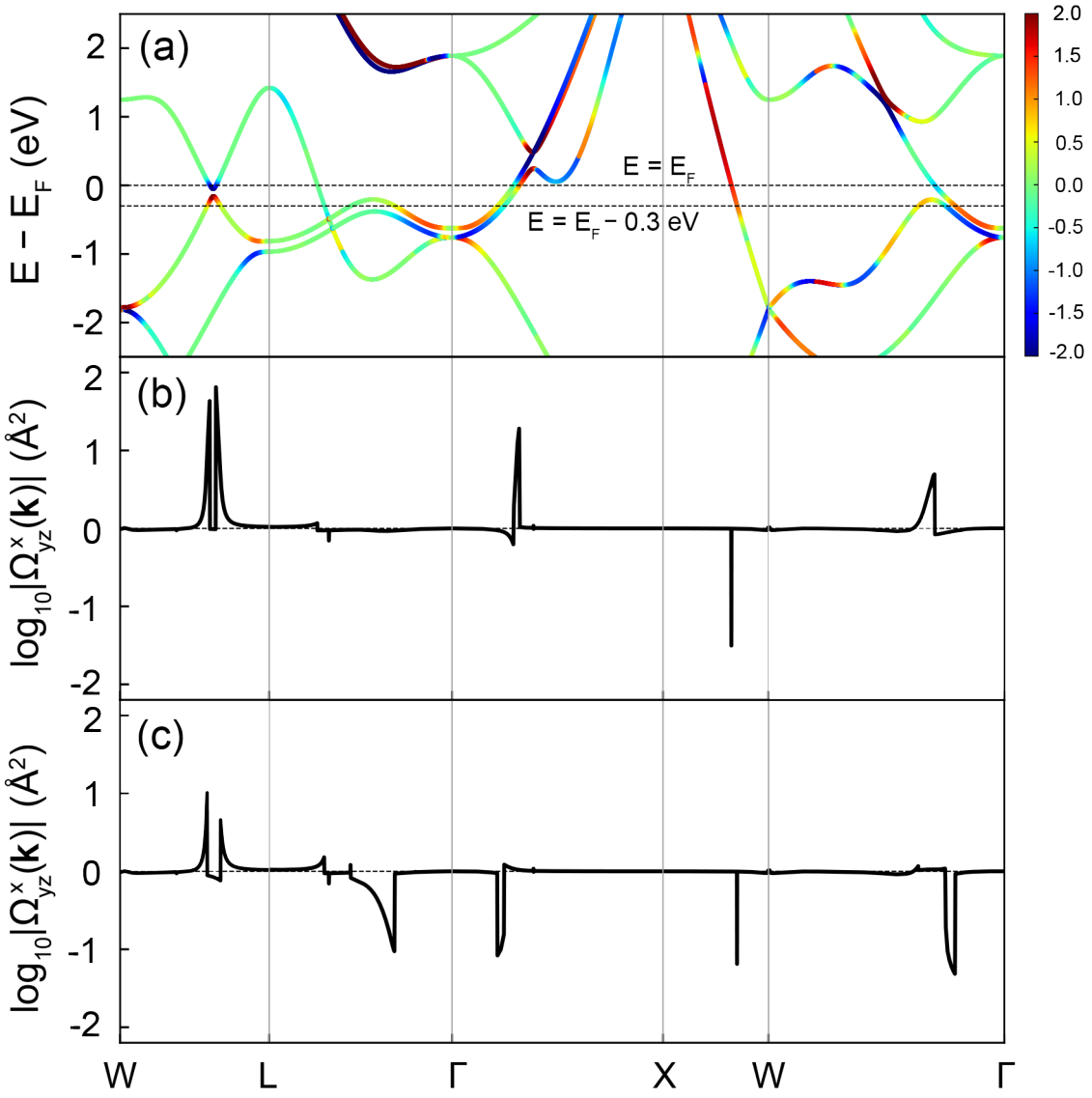

Figure 3.9: Analyses of spin Berry curvature of Mo. (a) Band-projected spin Berry curvature. Colorbar indicates the amplitude of spin Berry curvature in the log scale defined as Eq. 3.6. Two black dashed horizontal lines denote energy points $E = E_F$ and $E = E_F - 0.3$ eV. (b) and (c) present the amplitudes of spin Berry curvatures at $E = E_F$ and $E = E_F - 0.3$ eV, respectively. (a), (b), and (c) are along the same $\boldsymbol{k}$-path.

projected spin Berry curvature $\Omega^x_{n,yz}(\boldsymbol{k})$, in the log scale as defined as

$$\text{result} = \begin{cases} \text{sgn}(x)\lg|x|, & |x| > 10, \\ \frac{x}{10}, & |x| \leqslant 10. \end{cases} \tag{3.6}$$

Several high-symmetry points are selected to present the $\boldsymbol{k}$-resolved contribution to SHC. Figure 3.9(a) presents that the spin Berry curvatures are relatively small at E_F shown by the green color. At the energy $E = E_F - 0.3$ eV, the positive contributions along W-L path are reduced, since SHC is the integral over occupied bands. Thus, the negative SHC increases to -841 $(\hbar/e)$S/cm. Figures 3.9(b) and (c) present more intelligible results, i.e. the amplitudes of spin Berry curvature at different energy points. It can be observed that spin Berry curvatures along the $\boldsymbol{k}$-path are widely negligible except some peaks. Figure 3.9(b) illustrates that at $E = E_F$, the spin Berry curvature along W-L is positively large, and positive contributions occur along Γ-X and W-Γ, originating from the valence bands close to E_F. Figure 3.9(c) shows the spin Berry curvature at $E = E_F - 0.3$ eV. It has a negative peak along L-Γ. More intriguingly, contributions along Γ-X and W-Γ turn to be negative, reinforcing the negative SHC of Mo.

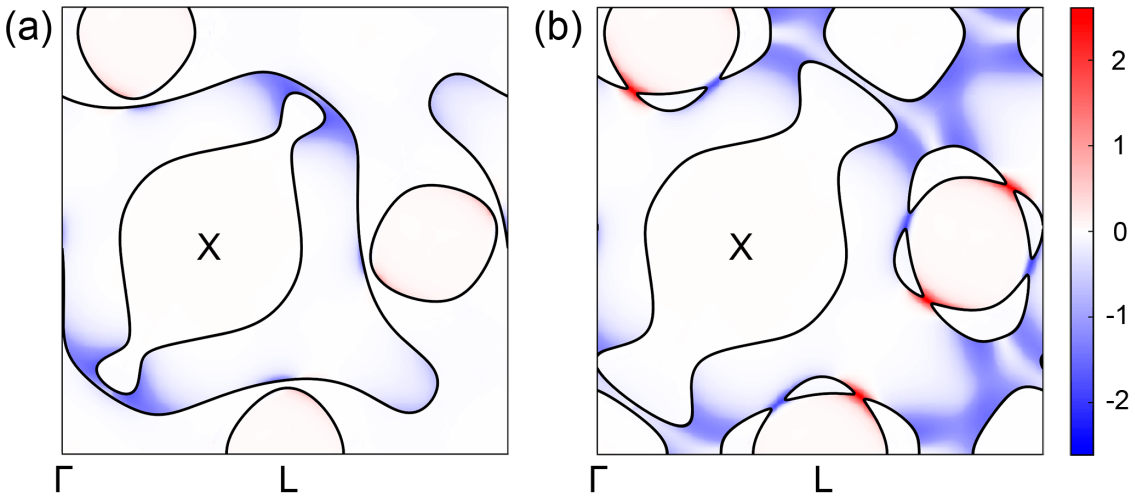

Figure 3.10: The spin Berry curvature in 2D slices of $k_z = 0$ in BZ for σ^x_{yz} SHC of Mo. (a) Slice at $E = E_F$. (b) Slice at $E = E_F - 0.3$ eV. The color bar indicates the term is in the log scale defined as Eq. 3.6. Γ (0, 0, 0), L ($\frac{1}{2}$, 0, 0), and X ($\frac{1}{3}$, $\frac{\sqrt{2}}{3}$, 0) are employed as high symmetry points.

To present a more visual picture on the spin Berry curvature of Mo, we display the spin Berry curvature on the 2D slice of $k_z = 0$ in BZ. The slice crosses high-symmetry

points of Γ, L and X. Figure 3.10(a) shows the result at $E = E_F$ and Fig. 3.10(b) is for $E = E_F - 0.3$ eV. The red and blue colors on slices illustrate the positive and negative spin Berry curvatures, respectively, and black lines denote the intersections of 2D slice and Fermi surface. Figure 3.10(a) presents that most regions of the slice at E_F are shown by the white color, manifesting the negligible magnitude of spin Berry curvature. Some parts contributing negatively are shown in blue. Figure 3.10(b) shows that at $E = E_F - 0.3$ eV, although some positive regions appear, the negative fractions augment, leading to a negatively large SHC of Mo.

3.4.2 SHC of Ir

Figure 3.11 shows the energy-resolved SHC of Ir metal, inset denotes primitive cell. SHC at Fermi energy is 403 $(\hbar/e)$S/cm. An SHC peak occurs at $E = E_F + 0.84$ eV, where SHC reaches up to 2056 $(\hbar/e)$S/cm. By lowering the position of E_F, SHC can become negative to be $-1713(\hbar/e)$S/cm at $E = E_F - 4.42$ eV and -1577 $(\hbar/e)$S/cm at $E = E_F - 3.74$ eV.

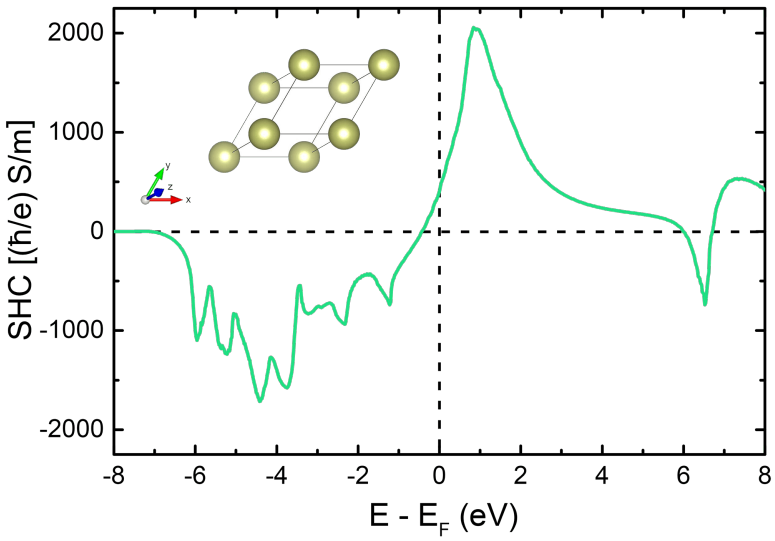

Figure 3.11: Energy-resolved SHC of Ir metal, inset is the structure of primitive cell.

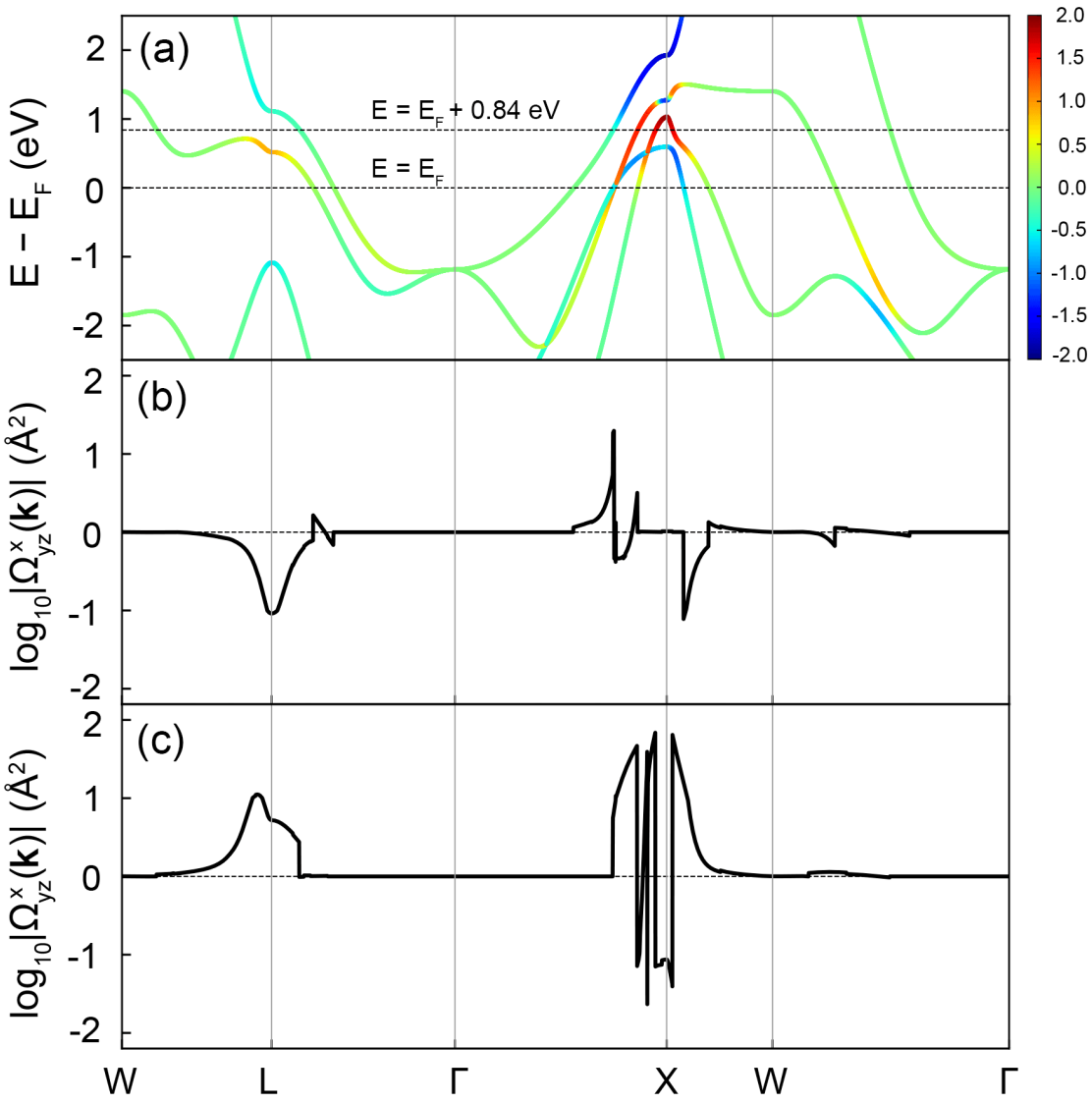

Figure 3.12: Analyses of spin Berry curvature of Ir. (a) Band-projected spin Berry curvature. Colorbar indicates the amplitude of spin Berry curvature in the log scale defined as Eq. 3.6. Two black dashed horizontal lines denote energy points $E = E_F$ and $E = E_F + 0.84$ eV. (b) and (c) present the amplitudes of spin Berry curvatures at $E = E_F$ and $E = E_F + 0.84$ eV, respectively. (a), (b), and (c) are along the same $\boldsymbol{k}$-path.

Figure 3.12 presents analyses of spin Berry curvature of Ir. Figure 3.12(a) shows that the spin Berry curvature is relatively small at E_F, however, at the energy $E = E_F + 0.84$ eV, positive spin Berry curvature occurs at X point as shown by the red color. This can be attributed to the strong spin-orbit splitting at X point. When the

energy is shifted to $E = E_F + 0.84$ eV, double degeneracies lifted by the SOC can be observed at the X point in Fig. 3.12(a), further inducing to the large SHC of 2056 ($\hbar$/e)S/cm. Figures 3.12(b) and (c) visually illustrate that most spin Berry curvatures are negligible along the $\boldsymbol{k}$-path, except the regions around L and X points. Figure 3.12(b) shows that at $E = E_F$, the spin Berry curvature at L point is negative. The reason can be attributed to the valence band close to E_F at L point, as shown in blue color in Fig. 3.12(a). The spin Berry curvature around X point varies, especially at points where bands cross E_F. Figure 3.12(c) shows the spin Berry curvature term at $E = E_F + 0.84$ eV. At L point, spin Berry curvature turns to be positive, and dramatic changes occur around X point owing to the bands with strong spin-orbit splitting.

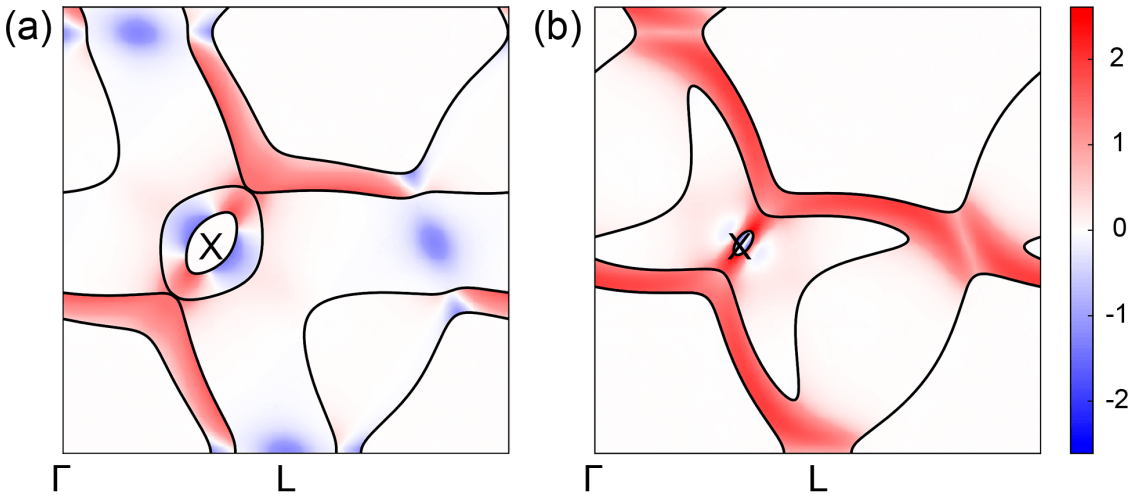

Figure 3.13: The spin Berry curvature in 2D slices of $k_z = 0$ in BZ for σ^x_{yz} SHC of Ir. (a) Slice at $E = E_F$. (b) Slice at $E = E_F + 0.84$ eV. The color bar indicates the term is in the log scale defined as Eq. 3.6. Γ (0, 0, 0), L ($\frac{1}{2}$, 0, 0), and X ($\frac{1}{3}$, $\frac{\sqrt{2}}{3}$, 0) are employed as high symmetry points.

Figures 3.13(a) and (b) show the 2D slices of spin Berry curvature of Ir at $E = E_F$ and $E = E_F + 0.84$ eV, respectively. Figure 3.13(a) shows that around X point, the spin Berry curvature exhibits dramatic changes, and the trade-off of positive and negative contribution leads to the vanishing SHC. Moreover, at L point, the spin Berry curvature is negative, shown by the slightly blue color. When the Fermi energy

is elevated by 0.84 eV as shown in Fig. 3.13(b), the spin Berry curvature around L point turns to be positive as shown by the red color. This variation is corresponding to the projected band structures in Figs. 3.12(b) and (c), where the sign of spin Berry curvature at L point is reversed by the shift of E_F position. Besides, the positive contribution expands and strengthens, whereas the negative regions disappear around L point, resulting in the enhancement of positive SHC, i.e. from 403 $(\hbar/e)$S/cm at $E = E_F$ to 2056 $(\hbar/e)$S/cm at $E = E_F + 0.84$ eV.

At the end of this section, we summarize and compare spin Hall properties of several HMs. Table 3.1 presents the calculated SHC and observed SHA of different HMs. It is noticeable that Pt has the highest SHC among all HMs. In fact, the peak of Pt SHC is exactly located at E_F,[135] resulting in an SHC as high as 2200 $(\hbar/e)$S/cm. Attracted by the inspiring theoretical result, people devote to the SHE experiments of Pt, and report a 0.076 SHA of Pt.[77] The relatively small SHA is owing to the superior electrical conductivity of Pt. Besides, β-W has an SHC of -1255 $(\hbar/e)$S/cm,[132] as well as an SHA reaching up to 0.30±0.02 due to its low electrical conductivity.[86] It has been reported that the SHA of β-Ta is in the range of 0.12–0.15,[71] and the SHA of Ir is 0.02±0.005.[87] Later on, attributed to the SHE and exchange bias, the field-free SOT switching has been achieved based on Ir layer,[113] illustrating the potential to realize SOT MTJ with Ir metal.

Table 3.1: Spin Hall properties of different HMs. SHC is the calculated value at E_F, $\mathrm{SHC_{MAX}}$ is the peak value of SHC, both are in the unit of $(\hbar/e)$S/cm. Energy is the position where $\mathrm{SHC_{MAX}}$ occurs, in the unit of eV. SHA is the result of experiments.

HMs	Pt[77, 135]	β-W[86, 132]	β-Ta[71, 81]	Mo	Ir[87]
SHC	2200	-1255	-389	-421	403
$\mathrm{SHC_{MAX}}$	2200	-1565	-2055	1230	2056
Energy	E_F	$E_F - 0.4$	$E_F + 1.24$	$E_F + 3.82$	$E_F + 0.84$
SHA	0.076	0.30±0.02	0.12–0.15	-	0.02±0.005

3.4.3 SHC optimization through doping

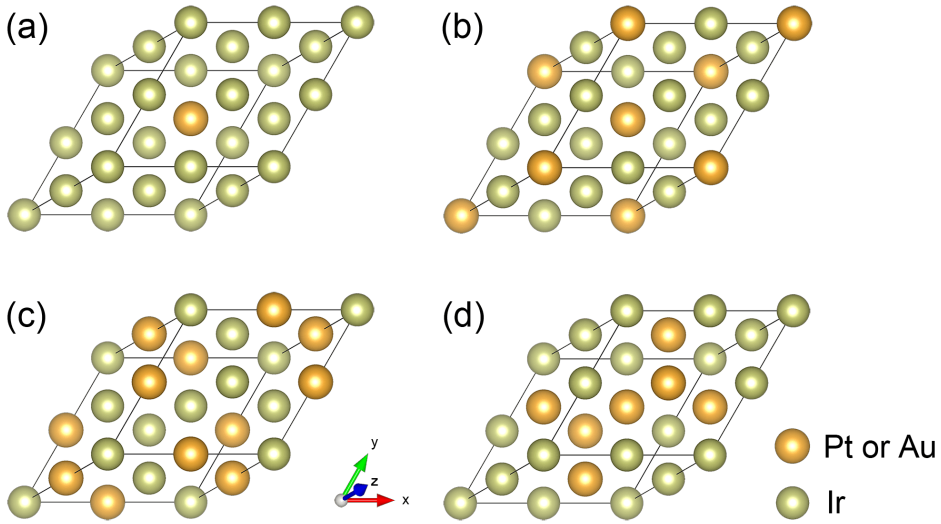

Figure 3.14: Atomic structures of $Ir_{1-x}Pt_x$ or $Ir_{1-x}Au_x$ alloys. (a) $x = 0.125$. (b) $x = 0.25$. (c) $x = 0.375$. (d) $x = 0.5$.

Efficient SOT switching requires the HMs with superior spin Hall properties, thus, the method to optimize SHC and SHA has great significance. Previous work has verified that substitutional doping is an effective method to achieve SHC optimization.[132] Through analyzing the SHC outlines of Mo and Ir, we conclude that it is more promising to improve the SHC of Ir, since the SHC peak of Ir is higher and closer to E_F, i.e., 2056 $(\hbar/e)$S/cm at $E = E_F + 0.84$ eV. It is quite probable to tune the SHC of Ir with substitutional Pt or Au atoms, since the element Pt has one more electron than Ir, and Au has two more electrons than Ir. Substitutional atoms with more electrons would elevate E_F and then enhance the SHC of Ir alloys.

Based on this idea, we built a $2 \times 2 \times 2$ supercell of Ir, and replaced part of Ir atoms by Pt or Au atoms. Atomic structures are shown in Fig. 3.14 where periodic boundary conditions are satisfied. We calculated SHC of Ir alloys with varying components and present results in Fig. 3.15, where the SHC of Ir metal is set as references in the top subfigures. Results in the left column illustrate that for the Pt doping, the SHC is

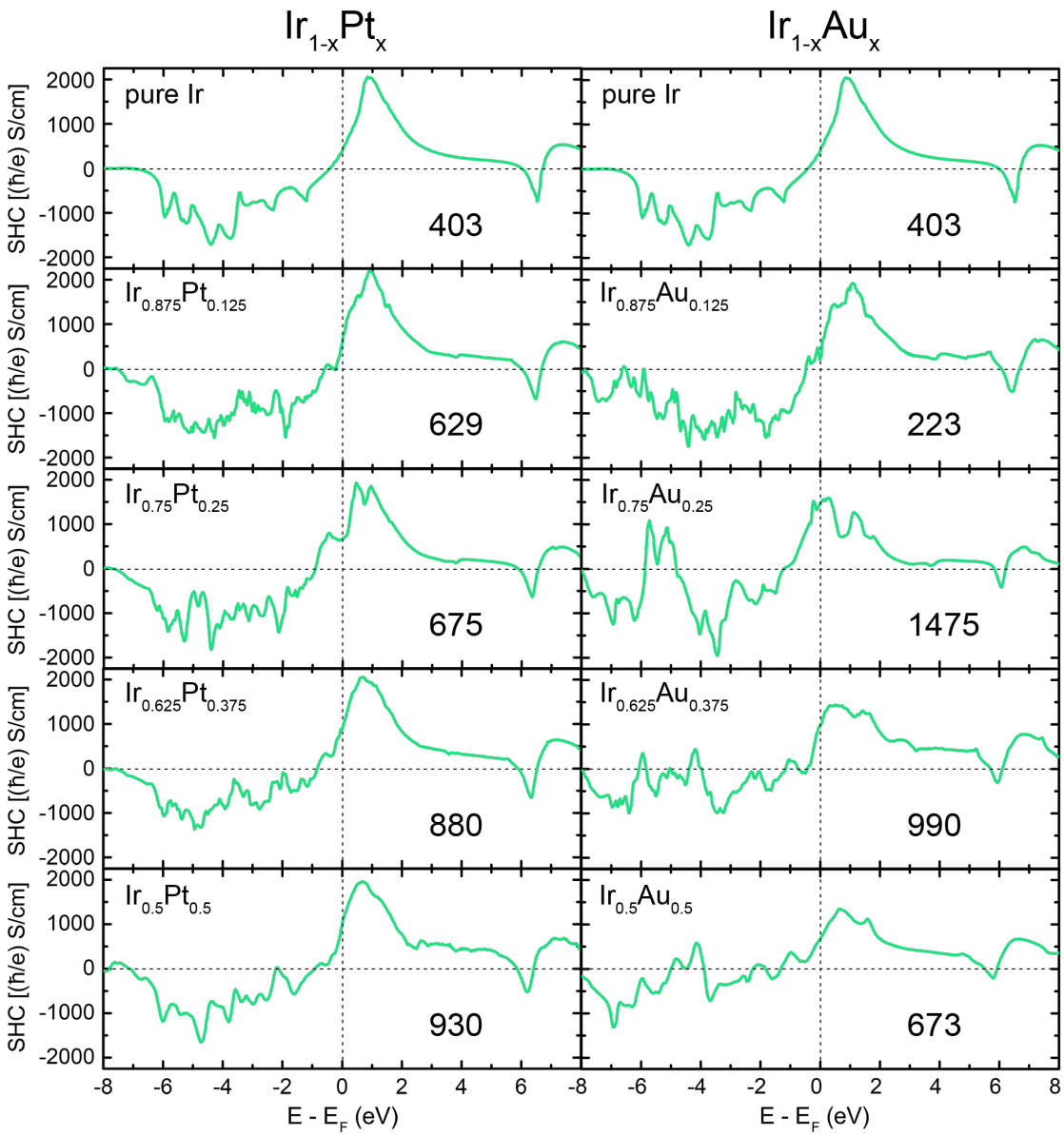

Figure 3.15: SHC of Ir alloys. Left column is for $Ir_{1-x}Pt_x$ alloys and right column is for $Ir_{1-x}Au_x$ alloys. $x = 0.125, 0.25, 0.375, 0.5$, respectively. SHC of pure Ir metal is given for references. Values in subfigures indicate the SHC at E_F.

rising with increasing Pt component, since the SHC peak is approaching to E_F. A more inspiring result can be found in Au-doped alloys, where $Ir_{0.75}Au_{0.25}$ alloy presents an SHC reaching up to 1475 $(\hbar/e)$S/cm, more than three times as large as the SHC of pure Ir. Considering that doping would probably increase the resistivities of metals,[136] large SHAs can be expected in Pt-doped and Au-doped Ir alloys.

We discuss the SHC of $Ir_{0.75}Au_{0.25}$ alloy briefly. Figure 3.16 presents the analyses of spin Berry curvature. A complicated band structure of $Ir_{0.75}Au_{0.25}$ has been presented in Fig. 3.16(a), where many bands cross E_F, leading to rapid changes of spin

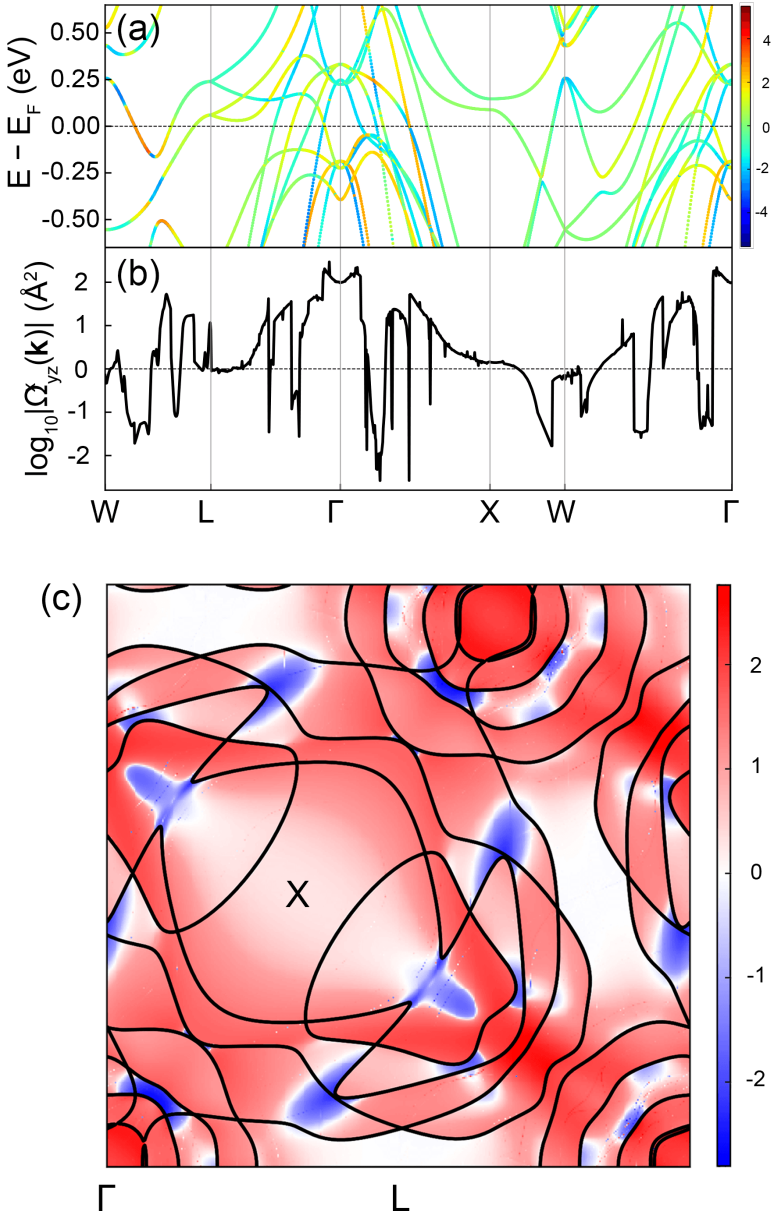

Figure 3.16: Analyses on SHC of $Ir_{0.75}Au_{0.25}$. (a) Spin Berry curvature projected on the band structure. (b) Amplitudes of spin Berry curvatures at $E = E_F$. (c) The spin Berry curvature term in slices of the BZ at $k_z = 0$ for σ^x_{yz} SHC of $Ir_{0.75}Au_{0.25}$ at $E = E_F$.

Berry curvatures as shown in Fig. 3.16(b). Figure 3.16(c) shows that most fractions contribute positively to SHC. Regions around Γ point make dominant contributions to SHC, while other regions exhibit variations in both amplitudes and signs. Through comparing Fig. 3.16(c) with Fig. 3.13(a), we can find that 25% Au concentration makes great difference, since it not only alter the electronic band structure, but also tune the position of Fermi energy.

3.5 Summary

Plenty of experiments have reported that heavy metals could modulate performances of MTJs. However, theoretical works on intrinsic influence caused by HMs remain inadequate. To reveal the intrinsic mechanism and provides guidelines to experiments, we theoretically studied the TMR and SHE in MgO-based MTJs with different heavy metals.

We firstly designed symmetrical MTJs with different HMs including Ta, W, Mo, and Ir, which are used as capping and bottom layers. *Ab initio* calculations manifest that HMs can greatly impact the spin-dependent conductance as well as the subsequent TMR. Compared to Ta, both W and Mo are desirable candidate for high TMR. More intriguingly, Ir-MTJ exhibits remarkable TMR effects thanks to its high G_{PC} and ultralow G_{APC}. Diverse transmission channel spectra of different materials are presented. Spin-resolved transmission spectra show that in PC, the majority-spin transmission peaks occur in all MTJs except Mo-capped MTJ. Analysis of projected band reveals the absence of Δ_1 band crossing E_F in Mo metal, explaining the disappearance of the centered transmission peak. Meanwhile, the minority-spin channel in PC is dominated by the interfacial resonant states, which attenuate slightly in the tunneling transport. The voltages applied on MTJs reduce TMR ratios, partly due to the destruction of resonant tunneling in the minority-spin channel of PC.

After that, we investigated SHC of heavy metals since SOT can be induced by spin Hall effect. SHC of Mo and Ir metals have been presented. Mo has an SHC of -412 $(\hbar/\mathrm{e})\mathrm{S/cm}$ at E_F. SHC of Ir is 403 $(\hbar/\mathrm{e})\mathrm{S/cm}$ at E_F, and 2056 $(\hbar/\mathrm{e})\mathrm{S/cm}$ at $E = E_F + 0.84$ eV. We analyzed SHC in the aspect of spin Berry curvature. After the examination, we find it is promising to optimize the SHC of Ir by doping using substitutional Pt or Au atoms. Substitutional atoms with more electrons can elevate the position of E_F and then enhance SHC in Ir alloys. We studied the SHC of $\mathrm{Ir}_{1-x}\mathrm{Pt}_x$ and $\mathrm{Ir}_{1-x}\mathrm{Au}_x$ alloys, where $x = 0.125$, 0.25, 0.375, 0.5, respectively. It turns out that $\mathrm{Ir}_{0.75}\mathrm{Au}_{0.25}$ can realize an SHC of 1475 $(\hbar/\mathrm{e})\mathrm{S/cm}$, over three times as large as the SHC of Ir metal. The result demonstrates that substitutional doping is an effective way to improve SHC, hence raising the efficiency of SOT switching. Works above clarify the TMR and SHE modulations induced by heave metals, providing guidelines on the choice of heavy metals to optimize MTJ performances.

Chapter 4

MTJ based on vdW heterojunction

4.1 Introduction

Despite great achievements, MgO-based MTJs are facing the challenge induced by 2% lattice mismatch at the ferromagnet/insulator interface.[37] This obstacle, which is harmful to the material crystallization and the device performance, has become the bottleneck in MTJ development. On the other hand, the emergence of vdW materials removes the concept of lattice mismatch in vdW heterojunctions, where vdW materials are vertically stacked without in-plane lattice limitation.[53–55] In this way, diverse functionalities can be integrated into one heterostructure through stacking vdW materials, enabling various possibilities of devices. Many experimental works have reported vdW MTJs in the thickness of atomic scale.[60–65] However, although giant TMR effects have been observed at ultralow temperature, the absence of room-temperature TMR hinders the practical applications of vdW MTJs. Besides, the conventional magnetic field switching of vdW MTJs [64, 65] impedes the miniaturization of devices. To fill the vacuum of applicable vdW MTJ, in this chapter, we will discuss the vdW MTJ working at room temperature as well as the possibility to switch vdW MTJ using SOT.

4.2 TMR in MTJ of VSe_2/MoS_2 heterojunction

The intrinsic room-temperature ferromagnetism has been observed in VSe_2 monolayer grown on MoS_2 substrate by molecular beam epitaxy.[59, 137] Inspired by the progress in experimental works, we design the vdW MTJ on basis of VSe_2/MoS_2 heterojunction and study its transport properties.

4.2.1 Atomic model and method

Two vdW MTJs based on ferromagnetic VSe_2 monolayers are proposed. Figure 4.1(a) shows the 1T VSe_2/1H MoS_2/1T VSe_2 MTJ, which is abbreviated as MT MTJ in the following. MoS_2 in 1H phase is used as the tunnel layer with the bandgap of 1.9 eV.[138] The VSe_2 in 1T phase is employed as the ferromagnetic layer. Since the magnetization of VSe_2 decays with the increasing layer number,[59, 139] we only study the VSe_2 monolayer in this work. MoS_2 is a good substrate for uniform growth of VSe_2,[59] thus the VSe_2/MoS_2 heterojunction is highly feasible in experiments. For MT MTJ, we define the PC (APC) as the bottom VSe_2 monolayer having the parallel (anti-parallel) magnetized orientation relative to the top VSe_2 monolayer, i.e. the bottom VSe_2 monolayer is the free layer.

Besides, we design another vdW MTJ using 1H VSe_2 to be the tunnel layer as shown in Fig. 4.1(b), with the abbreviation of VT MTJ. For VT MTJ, we define the PC (APC) as the 1H VSe_2 tunnel layer holding the parallel (anti-parallel) magnetized orientation relative to the other two 1T VSe_2 monolayers, namely, 1H VSe_2 is the free layer. Since 1H VSe_2 is the magnetic semiconductor,[140] we expect that both tunnel transport and spin filtering would happen in VT MTJ, as well as the subsequently high TMR. Apart from the basic MTJ structure, the metallic vdW material, 1T phase MoS_2 layers are adopted as the electrodes above and below MTJs. For both MTJs, the tunneling transport is along x direction.

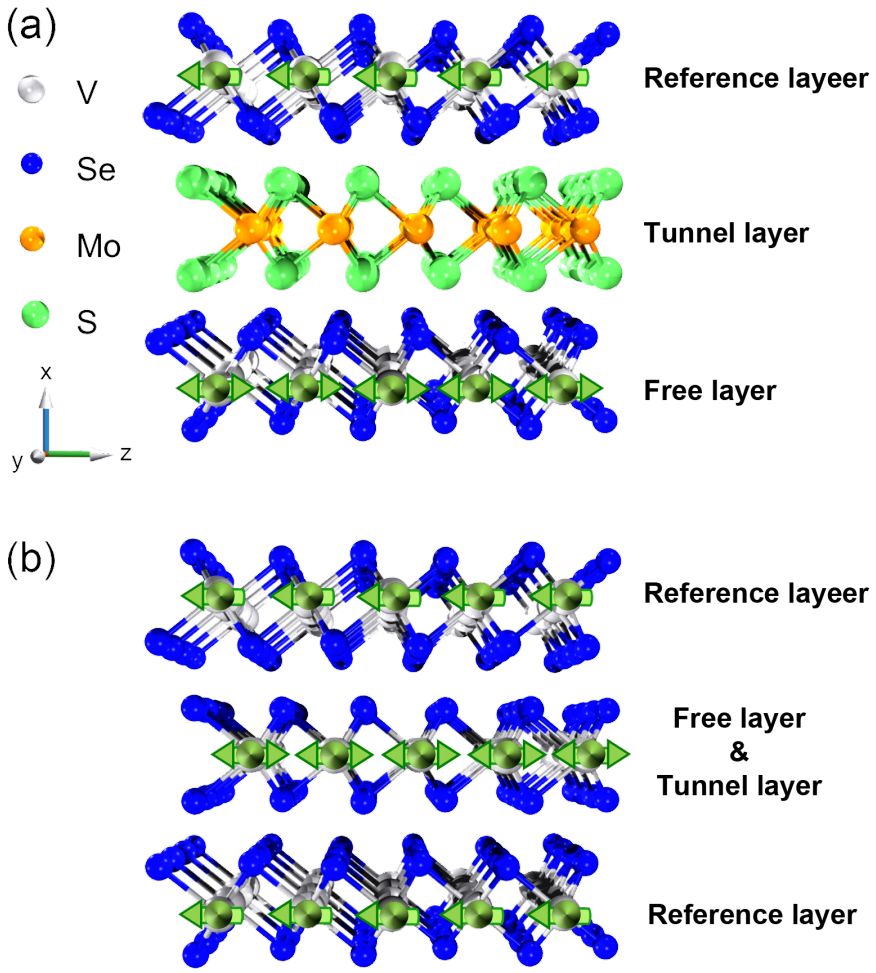

Figure 4.1: Atomic models of (a) 1T VSe_2/1H MoS_2/1T VSe_2 MTJ (abbreviated as MT MTJ) and (b) 1T VSe_2/1H VSe_2/1T VSe_2 MTJ (abbreviated as VT MTJ). Green arrows illustrate the magnetized orientation. Role of every layer is shown in the right side.

The structure optimizations were performed using VASP, with the optB88-vdW functional and the Hubbard U_{eff} = 1.0 eV on d orbital of V element.[141] Energy cutoff of 520 eV, $\boldsymbol{k}$-mesh of $1 \times 21 \times 21$, and maximum force convergence criterion of 0.01 eV/Å were adopted. The in-plane lattice constant is fixed to 3.35 Å.[142] In MT MTJ, the distance between 1T VSe_2 layer and 1H MoS_2 layer is 3.067 Å. In VT MTJ, the distance between 1T VSe_2 layer and 1H VSe_2 layer is 3.234 Å. Both MTJs are symmetrical to keep the most stable interfacial configurations.

The electrical transport properties were calculated using OpenMX package.[143–145] The pseudoatomic orbitals are specified by V8.0-s2p2d1, Mo9.0-s2p2d1, Se8.0-s2p2, and S8.0-s2p2. A Hubbard term on the d orbital of V was considered with $U = 1.0$ eV. The energy cutoff was set to be 3000 eV. The self-consistent calculations were performed using $\boldsymbol{k}$-mesh of $1 \times 21 \times 21$, and the transport properties were calculated with $\boldsymbol{k}$-mesh of $1 \times 150 \times 150$.

We calculated the intrinsic spin Hall conductivity of MoS_2 using the same method as introduced in Sec. 3.2. The plane-wave cutoff energy was 600 eV. A $\boldsymbol{k}$-mesh of $6\times16\times16$ was used in self-consistent calculations, and a dense $\boldsymbol{k}$-mesh of $200\times200\times200$ with adaptive mesh refinement was employed for SHC computations. GGA-PBE was used in all calculations.

4.2.2 Spin-resolved transmission

Table 4.1: Spin-resolved conductance and TMR ratios at the equilibrium state in MT MTJ and VT MTJ. The temperature condition is set to be 300 K, and the conductance is in the unit of $10^{-5}e^2/h$.

MTJs	$G^{\uparrow}_{PC}$	$G^{\downarrow}_{PC}$	$G^{\uparrow}_{APC}$	$G^{\downarrow}_{APC}$	TMR (%)
MT MTJ	225	45	111	111	22
VT MTJ	69	182	34	9	484

We calculated the spin-resolved conductance and TMR of both MT and VT MTJs at the equilibrium state and 300 K temperature, results are presented in Table 4.1. The TMR in MT MTJ is only 22%, however, the VT MTJ presents a much remarkable TMR up to 484%. In both MTJs, the conductance has a comparable scale in PC, while the conductance varies a lot in APC. Distinctly, $G^{\downarrow}_{APC} = 1.11 \times 10^{-3}\ e^2/h$ in MT MTJ is over one magnitude larger than $G^{\downarrow}_{APC} = 9 \times 10^{-5}\ e^2/h$ in VT MTJ. As the TMR ratio is inversely proportional to G_{APC}, low G_{APC} results in high TMR in VT

MTJ. We attribute the low G_{APC} to the effective spin filtering in APC of VT MTJ, where VSe_2 trilayer is stacked in anti-ferromagnetic ordering, blocking spin transport especially for the minority-spin states.

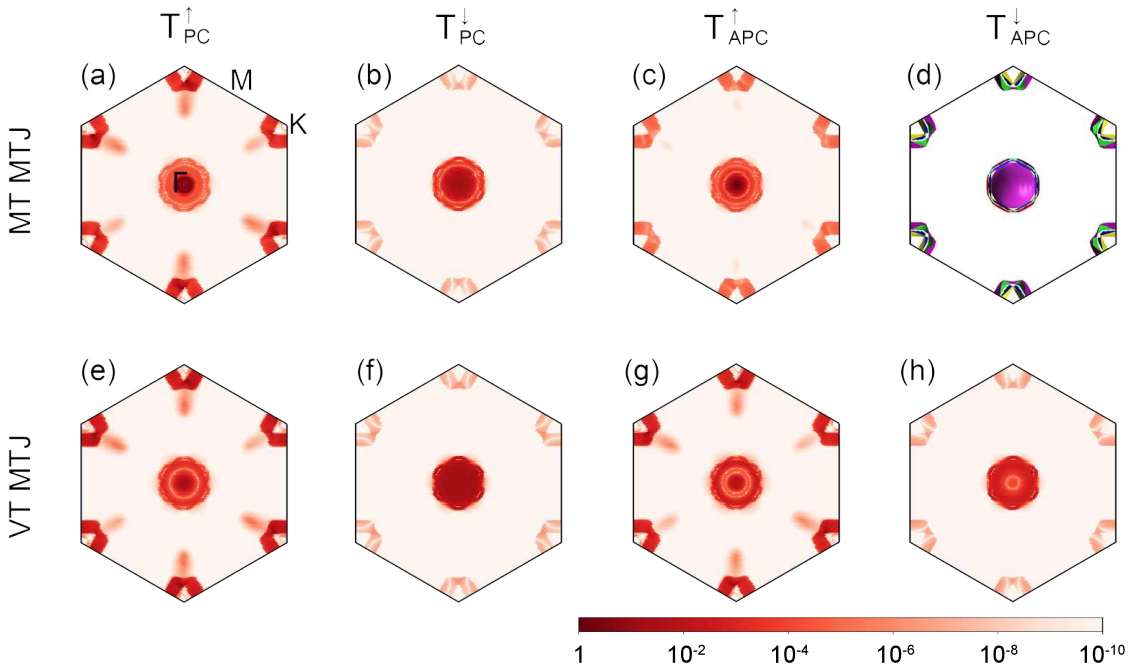

Figure 4.2: Spin- and $\boldsymbol{k}_{||}$-resolved transmission spectra. (a)-(c) are for MT MTJ and (e)-(h) are for VT MTJ. (d) is the Fermi surface of 1T MoS_2 electrode, projected on $k_z = 0$ in BZ. The color bar denotes the transmission scale.

Although VT MTJ can realize high TMR ratio at equilibrium state, it is not feasible for the SOT switching, since the free layer of VT MTJ is in the middle of junction instead of adjoining the bottom layer, incompatible to the conventional SOT device. We may make the bottom 1T VSe_2 ferromagnetic layer as the free layer of VT MTJ, but the double spin filtering effect would vanish, further impairing TMR. Consequently, we consider to analyze and improve the low TMR ratio in MT MTJ. To present more details of conductance, we plot the $\boldsymbol{k}_{||}$-resolved transmission spectra. Figures 4.2(a)-(h) show the transmission spectra in different spin channels in both MT and VT MTJs except for Fig. 4.2(d), which is the Fermi surface of 1T MoS_2 electrode, determining

the outlines of the transmission spectra. Figure 4.2(a) shows that in the majority-spin channel in PC of MT MTJ, a peak, with the maximum transmission coefficient of $T^{\uparrow}_{PC} = 0.16$ at Γ point, results in the high conductance $G^{\uparrow}_{PC}$. Due to the symmetrical structure of MT MTJ, the transmission spectra of $T^{\uparrow}_{APC}$ and $T^{\downarrow}_{APC}$ is identical at equilibrium state, so we only show the $T^{\uparrow}_{APC}$ in Fig. 4.2(c). In APC of MT MTJ, a sharp peak, with $T^{\uparrow}_{APC} = T^{\downarrow}_{APC} = 0.57$ at Γ point, occurs as shown by the deep red color and leads to the high conductance $G^{\uparrow}_{APC} = G^{\downarrow}_{APC} = 1.11 \times 10^{-3}\ e^2/h$ in MT MTJ. On the other hand, for VT MTJ, a remarkable broad peak of $T^{\downarrow}_{PC}$ can be observed in Fig. 4.2(f), resulting in the high conductance $G^{\downarrow}_{PC} = 1.82 \times 10^{-3}\ e^2/h$ in VT MTJ. Due to the double spin filtering effect in VT MTJ, the transmission in minority-spin channel of APC is negligible, as shown in Fig. 4.2(h). For example, $T^{\downarrow}_{APC} = 1.19 \times 10^{-4}$ at Γ point. Based on discussions above, we conclude that the low TMR ratio in MT MTJ can be attributed to the ultrahigh T_{APC}, such as $T^{\uparrow}_{APC} = T^{\downarrow}_{APC} = 0.57$ at Γ point.

4.2.3 Quantum-well states

To understand the unusual transmission coefficient and clarify the APC transmission, we present the minority-spin transmission analysis at Γ point for APC of both MT and VT MTJs, where $T^{\downarrow}_{APC} = 0.57$ and 1.19×10^{-4}, respectively. The analysis of wavefunction components indicates that the s and p_x orbitals in S and Se atoms, as well as the s, p_x, $d_{x^2\text{-}y^2}$ and d_{z^2} orbitals in Mo and V atoms, make the dominant contribution to the transmission, especially d orbitals. The shapes of p_x orbitals in S and Se atoms can be observed by the wavefunctions in Figs. 4.3(b)-(d), as well as the d_{z^2} orbitals in Mo and V atoms. Figure 4.3(a) shows the transmission versus energy curve of MT MTJ. The transmission peaks of both spin components locate approximately at E_F, at $E = E_F - 0.02$ eV to be exact. The transmission coefficient

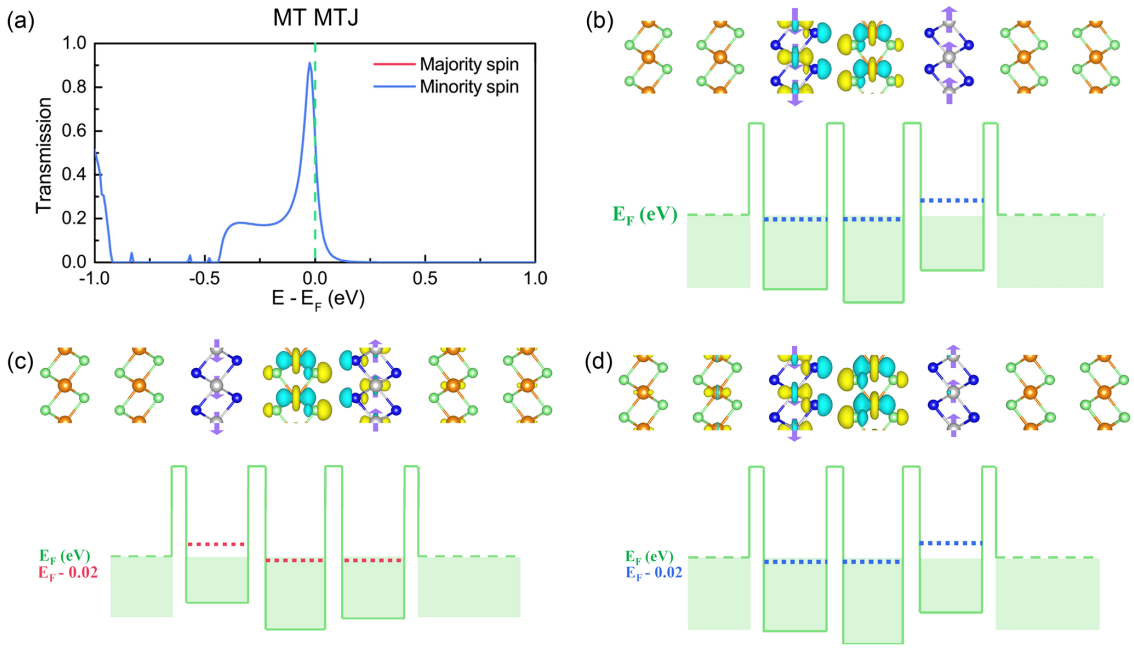

Figure 4.3: Spin-resolved transmissions and resonances of T_{APC} at Γ point for MT MTJ. (a) Transmission coefficients versus energy. (b) Transmission eigenchannel wavefunctions of minority-spin states at E_F. (c) and (d) are transmission eigenchannel wavefunctions of the majority- and minority-spin states, respectively, at $E = E_F - 0.02$ eV. Green dashed lines present the position of E_F. Red and blue dot lines indicate the energy levels of quantum-well states.

at E_F is $T^{\downarrow}_{APC} = 0.57$, which is extraordinarily high for tunneling transport. Figure 4.3(b) shows that eigenchannel wavefunctions localize at the left VSe_2 and the middle MoS_2 layers. Considering the high transmission and wavefunction localization, we infer that the quantum-well resonances arise in MT MTJ. Because of the weak interlayer interaction and the strong intralayer covalent bond, quantum-well resonances are very likely to occur in vdW heterojunctions.[65, 146] Quantum-well states are reflected back and forth, forming a standing wave pattern and resulting in the localization of wavefunctions as well as the transmission probability close to unity. The bottom panel of Fig. 4.3(b) gives a more intelligible picture on resonances by the schematic plot of the potential profile. Close to E_F, the energy levels of quantum-well states in the left VSe_2 and the middle MoS_2 layers match with each other, resulting in the

resonances, as well as the intense localization and ultrahigh transmission. Moreover, we studied the transmission at $E = E_F - 0.02$ eV and present the majority-spin and minority-spin results in Figs. 4.3(c) and (d), respectively. Stronger resonances of both spin components can be observed at the energy point $E = E_F - 0.02$ eV where transmission $T^{\uparrow}_{APC} = T^{\downarrow}_{APC} = 0.91$.

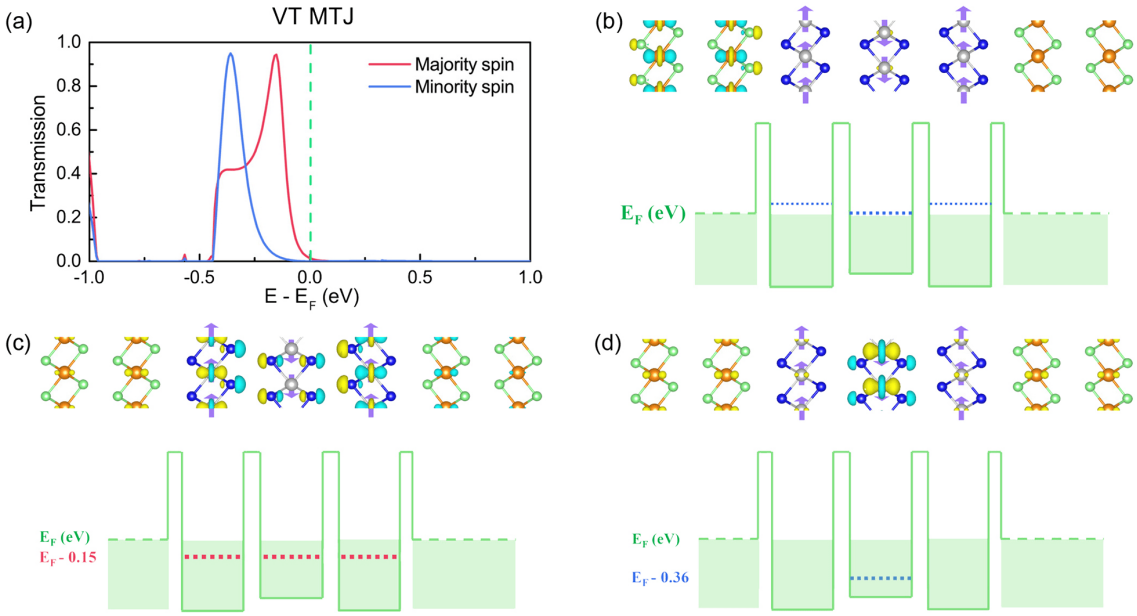

Figure 4.4: Spin-resolved transmissions and resonances of T_{APC} at Γ point for VT MTJ. (a) Transmission coefficients versus energy. (b) Transmission eigenchannel wavefunctions of minority-spin states at E_F. (c) Transmission eigenchannel wavefunctions of majority-spin states at $E = E_F - 0.15$ eV. (d) Transmission eigenchannel wavefunctions of minority-spin states at $E = E_F - 0.36$ eV. Green dashed lines present the position of E_F. Red and blue dot lines indicate the energy levels of quantum-well states.

Figure 4.4(a) shows the energy-resolved transmission for VT MTJ. Two peaks deviate from the E_F, as $T^{\uparrow}_{APC} = 0.95$ at $E = E_F - 0.15$ eV, and $T^{\downarrow}_{APC} = 0.94$ at $E = E_F - 0.36$ eV. Due to the rapid attenuation, the transmissions at E_F for both spins are negligible, and it turns out that $T^{\downarrow}_{APC} = 1.19 \times 10^{-4}$ at E_F. Figure 4.4(b) shows the minority-spin eigenchannel wavefunctions for VT MTJ at E_F. It can be observed

that the incoming wavefunctions decay along the transport x direction. Note that for minority-spin states, both the left 1T VSe_2 and the right 1T VSe_2 have the prohibitive magnetization, this spin filtering effect results in the negligible transmission. We plot the diagram of potential profile in the bottom panel of Fig. 4.4(b). Due to the mismatch in energy levels of quantum-well states, no resonance happens and the wavefunctions attenuate rapidly along the transport direction. However, the majority-spin transmission peak at $E = E_F - 0.15$ eV and the minority-spin one at $E = E_F - 0.36$ eV can be explained by the resonance. Figure 4.4(c) shows the eigenchannel wavefunctions for majority-spin states at $E = E_F - 0.15$ eV with the transmission coefficient $T^{\uparrow}_{APC} = 0.95$ at Γ point. In the VSe_2 trilayer, quantum-well states match in energy, leading to the resonances and high transmission at this energy point. Figure 4.4(d) shows the eigenchannel wavefunctions for minority-spin states at $E = E_F - 0.36$ eV, discussions are omitted here.

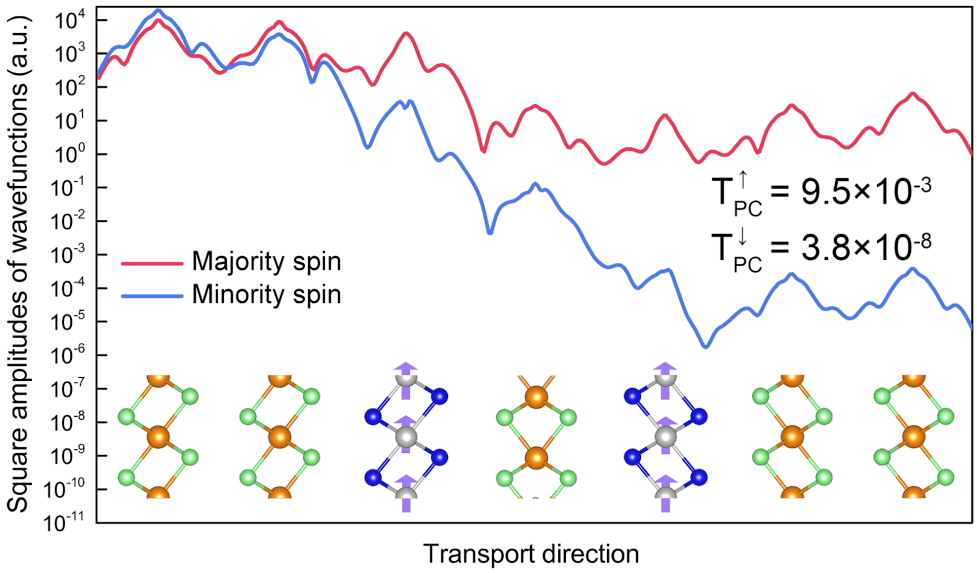

Figure 4.5: Square amplitudes of wavefunctions of transmission states at K′ point in PC of MT MTJ.

To emphasize the importance of resonances, we take MT MTJ as an example to present the non-resonant transmission at $\boldsymbol{k}_{||} = (0.283, 0.283)$, which is named as K′.

It can be read out in Fig. 4.2(a) that $T_{PC}^{\uparrow} = 9.5 \times 10^{-3}$ at K′, relatively high for tunneling transport. The square amplitudes of wavefunctions at K′ are shown in Fig. 4.5. Different from the quantum-well states, wavefunctions at K′ point decay along the transport direction without electron localization effect, and the minority-spin states decay much faster than the majority-spin states, resulting in a negligible transmission of $T_{PC}^{\downarrow} = 3.8 \times 10^{-8}$.

4.2.4 Non-equilibrium transport

Discussions above illuminate that the quantum-well resonances play an important role in the equilibrium transport. However, non-equilibrium transport tells another story. At the non-equilibrium state, the current is calculated as the integral

$$I_\sigma = \frac{e}{h} \int T_\sigma(E)[f(E-\mu_1) - f(E-\mu_2)]dE, \tag{4.1}$$

where f is the Fermi-Dirac statistics, μ_1 and μ_2 are the electrochemical potentials of the left and right contacts, respectively. Since the quantum-well resonances generally occur at certain levels, they have limited influence on the current which is an integral of transmissions in the bias window. The APC transmission spectrum of MT MTJ in Fig. 4.3(a) shows that there is almost no transmission above E_F. To reduce the current in APC and improve TMR, we applied the positive bias to MT MTJ and calculated the non-equilibrium transport properties. As a reference, non-equilibrium transport in VT MTJ was also studied.

Figure 4.6 shows the spin-resolved current and TMR ratio under electric field. Here we define that TMR ratio $= \frac{I_{PC}-I_{APC}}{I_{APC}} \times 100\%$. We observe that in both MTJs, PC currents rise with increasing bias, and majority-spin current is larger than minority-spin current, as shown in Figs. 4.6(a) and (d). However, APC currents behave distinctly in MT and VT MTJs. Figure 4.6(b) shows that in MT MTJ, both majority-spin

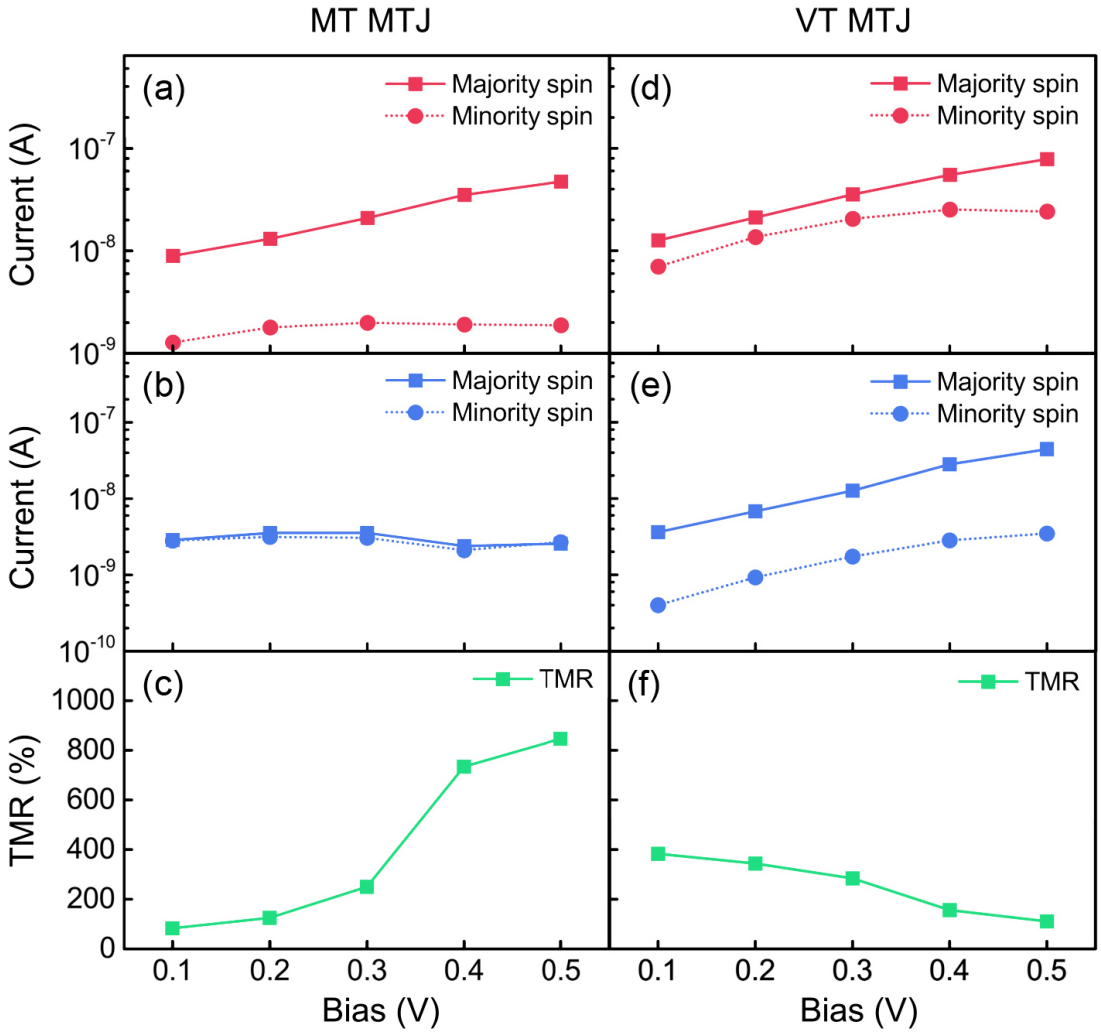

Figure 4.6: Non-equilibrium transport properties at 300 K. The left column is for MT MTJ while the right column is for VT MTJ. (a) and (d) are the currents in PC. (b) and (e) are the currents in APC. (c) and (f) are the TMR ratios.

and minority-spin currents in APC remain almost unchanged with increasing bias, while APC currents in VT MTJ rise with increasing bias, as shown in Fig. 4.6(e). Consequently, in MT MTJ, TMR augments with the increasing bias because of the changeless APC current, as shown in Fig. 4.6(c). Meanwhile, TMR in VT MTJ declines due to the enhancement of APC current with increasing bias, as shown in Fig. 4.6(f). At the bias of 0.5 V, MT MTJ presents a TMR of 846%, which is a considerable result for the room-temperature application.

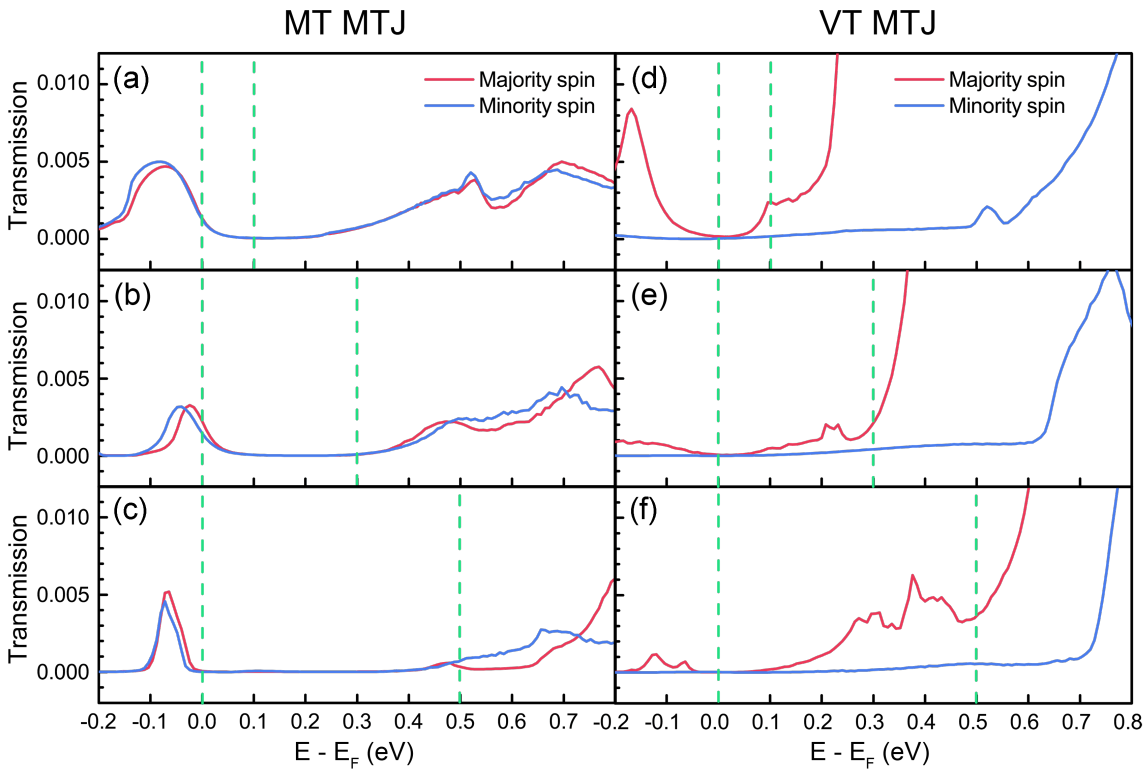

Figure 4.7: Spin-resolved T_{APC} under varying bias. The left column is for MT MTJ and the right column is for VT MTJ. (a) and (d) present the result of 0.1 V bias. (b) and (e) present the 0.3 V bias. (c) and (f) present the 0.5 V bias. Bias windows are shown by vertical green dashed lines.

Since the current is obtained by integrating transmission with respect to energies in the bias window, we turn to the analysis of the energy-resolved transmission spectra of APC under varying bias. APC transmission spectra of MT and VT MTJs are shown in Fig. 4.7, where transmission is the integration over all $\boldsymbol{k}_{||}$ points in BZ. We find that the transmission spectra of MT MTJ are almost changeless in all bias windows where the transmission coefficients approximate to zero. In the equilibrium state, the resonances at Γ point make the wavefunctions intensely localized. Affected by the bias in non-equilibrium states, the resonances move out of the bias windows and result in suppressed currents. On the other hand, majority-spin states dominate in the transmission of VT MTJ. With the rising bias, more majority-spin transmission

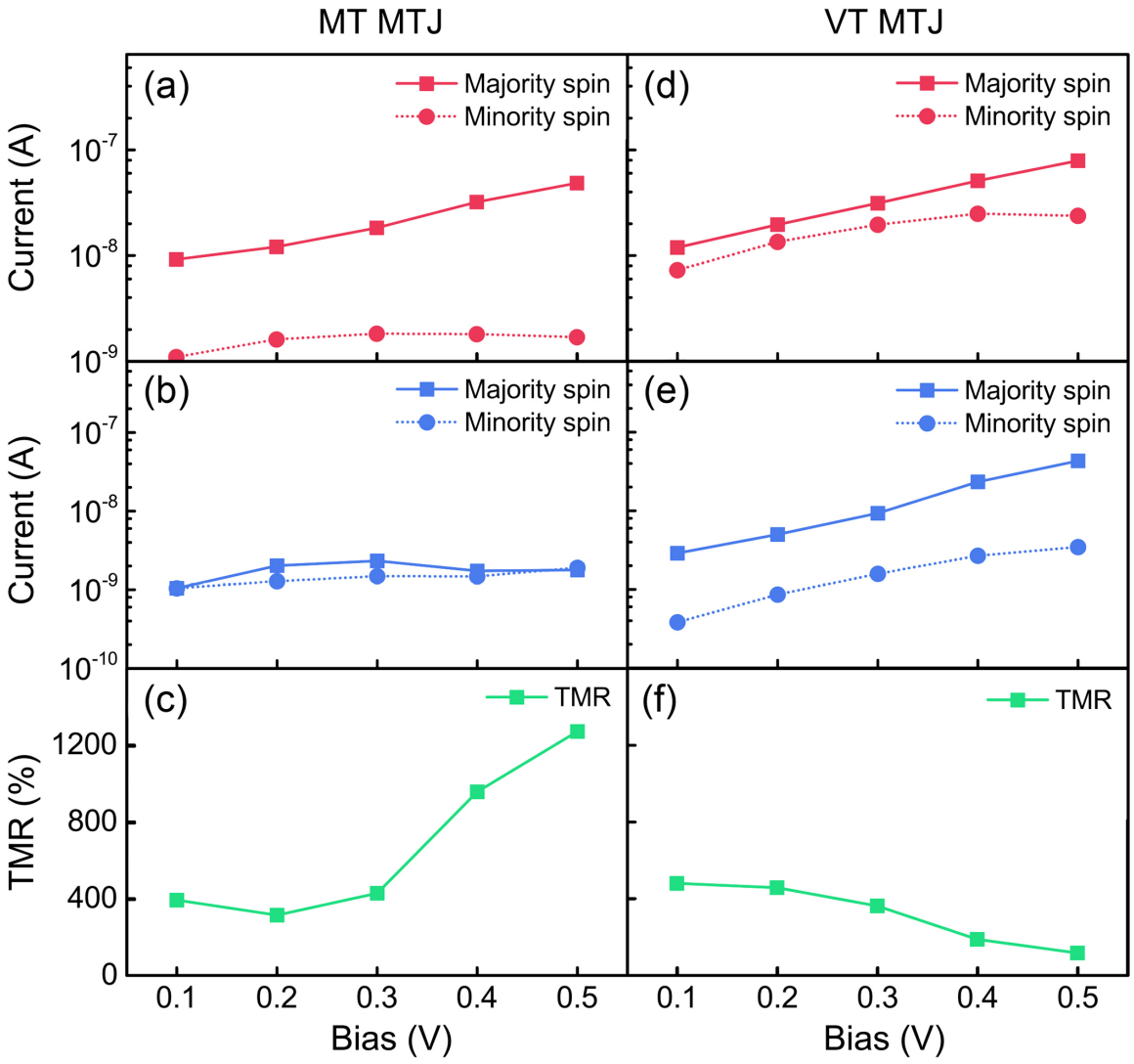

Figure 4.8: Non-equilibrium transport properties at 100 K. The left column is for MT MTJ while the right column is for VT MTJ. (a) and (d) are the currents in PC. (b) and (e) are the currents in APC. (c) and (f) are the TMR ratios.

peaks enter into the bias window and contribute to the current. Due to the effective spin filtering, the minority-spin transmission is suppressed in all of the bias windows. Combining the majority-spin and minority-spin currents together, we get the total current of APC, which increases with bias in VT MTJ. Analyses above explain the different behaviors of APC currents in MT and VT MTJs, explaining the subsequent TMR ratios.

Apart from the calculation at 300 K temperature, we present the calculation at 100 K temperature in Fig. 4.8. It worth stressing that a TMR ratio up to 1277% can be observed in MT MTJ, and the TMR enhancement is attributed to the decline of APC current at 100 K. Consequently, similar to that in the traditional MgO-based MTJ,[37, 38] the TMR ratio in vdW MTJ can also be enhance by the temperature decline.

4.2.5 Concept of SOT vdW MTJ

The magnetic field switching of vdW MTJs [64, 65] impedes the device miniaturization, while the STT switching is not recommended due to the low spin polarization of 1T VSe_2.[147] Thus, we consider the possibility to realize SOT switching in the vdW MTJ. Recently, SOT switching of Fe_3GeTe_2 magnetization has been observed in the Fe_3GeTe_2/Pt bilayer thanks to the SHE in Pt.[148, 149] Compared to the conventional SOT devices, high SOT efficiency has been found in the Fe_3GeTe_2/Pt bilayer, and the efficiency enhancement is attributed to the atomically flat surface which provides excellent interface and Based on works above, we put forward the concept of SOT vdW MTJ, as shown in Fig. 4.9(a). When the writing current is injected into the bottom 1T MoS_2 electrode, the spin current occurs along the vertical direction with the in-plane spin momentum, which can be used to switch the magnetization of the VSe_2 layer adjoining to the bottom MoS_2 layer. To explore the strength of SHE, we study the intrinsic spin Hall conductivity of 1T MoS_2. Results are shown in Fig. 4.9(b). Although the SHC at E_F is limited to -34 $(\hbar/e)$S/cm, SHC at $E = E_F - 2.0$ eV reaches up to 400 $(\hbar/e)$S/cm, illustrating that gate voltage control can help to improve SHC and realize the SOT switching of vdW MTJ.

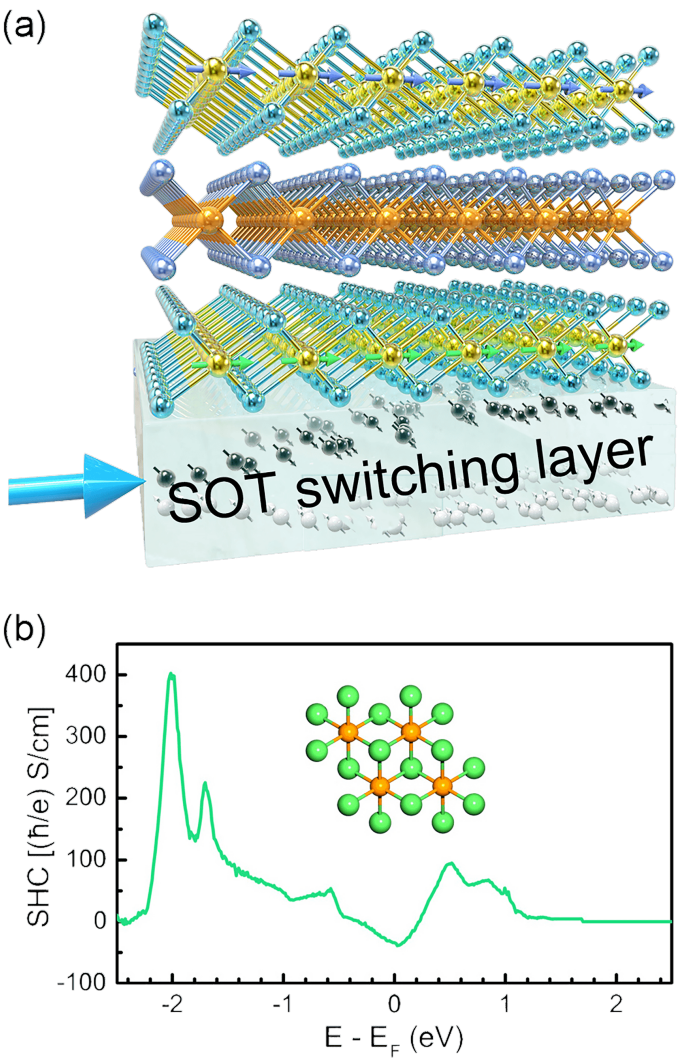

Figure 4.9: Concept of SOT vdW MTJ. (a) The atomic schematic diagram of SOT MTJ including the bottom layer, which is composed of 1T MoS_2 in MT MTJ and used for SOT switching. The blue arrow indicates the writing current, green and purple arrows in VSe_2 layers denote the magnetized orientations, and the small arrows in black and white represent the spins of electrons originating from SHE. (b) Energy-resolved SHC of the 1T MoS_2 in bulk.

4.3 SHE of semimetals $MoTe_2$ and WTe_2

Since the SHC of MoS_2 requires the enhancement via the gate voltage, we consider if we can find a material which has the intrinsic high SHC at E_F. WTe_2 attracted our attention due to its extraordinary SOT performance. Experimental works have reported

that WTe_2/permalloy (Py) device can produce an out-of-plane anti-damping torque when the current is applied along a low-symmetry axis. This is due to the absence of twofold rotational symmetry in WTe_2/Py bilayer.[150, 151] Moreover, the anisotropic enhancement of SOT in WTe_2/Py device has also been observed in experiments.[152] Works above trigger a motivation to explore the SHE of WTe_2. More intriguingly, it is expected to discover large SHA in WTe_2 which is the semimetal with low electrical conductivity.

4.3.1 Atomic model and method

We studied the transition-metal dichalcogenide (TMDC) materials including $MoTe_2$ and WTe_2, both of them are type-II Weyl semimetals with strong SOC and reduced crystalline symmetry.[153–156] Figure 4.10(a) shows the atomic structure of $MoTe_2$ and WTe_2. The space group is $Pmn2_1$ (No. 31), indicating the crystal structure possesses one mirror plane $x = 0$ and one glide mirror plane parallel to $y = 0$, which respectively transform to $k_x = 0$ and $k_y = 0$ planes in BZ as shown in Fig. 4.10(b). This crystalline structure can be classified into the *mmm* magnetic Laue group, which determines there are six nonzero SHC elements with different magnitudes.[157] Our calculations employ the atomic structures in previous reports,[153, 158] with the lattice constants $a = 3.458$ Å, $b = 6.304$ Å, $c = 13.859$ Å in $MoTe_2$, and $a = 3.477$ Å, $b = 6.249$ Å, $c = 14.018$ Å in WTe_2.

SHC of $MoTe_2$ and WTe_2 was calculated using the same method as the SHC calculation of MoS_2 in Sec. 4.2.5. The plane-wave cutoff energy was 600 eV. A $\boldsymbol{k}$-point grid of $12 \times 10 \times 6$ was used in DFT self-consistent calculations, and a dense $\boldsymbol{k}$-mesh of 500×500×500 with adaptive mesh refinement was employed for SHC calculation.

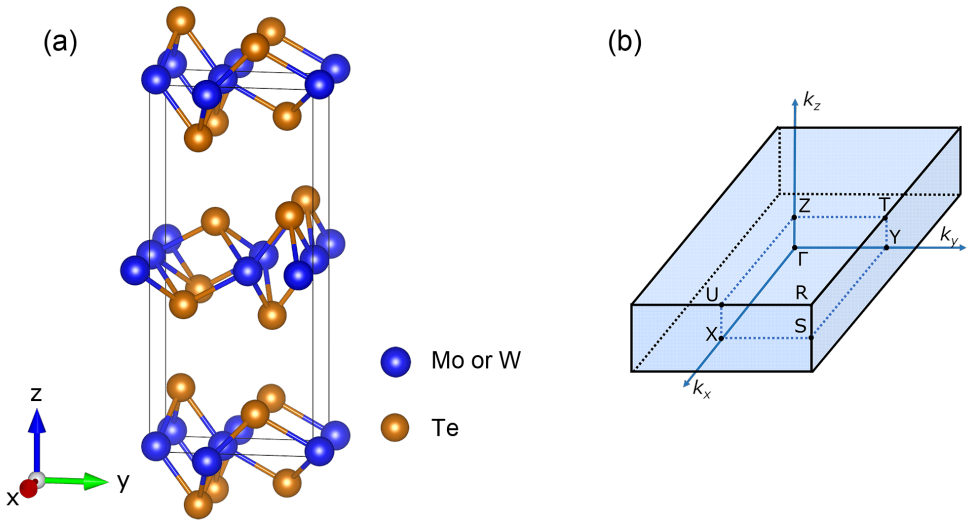

Figure 4.10: (a) Atomic structure of T_d-MTe_2 (M=Mo or W). (b) Schematic diagram of the three-dimensional BZ of MTe_2, the high symmetry points are indicated by black dot lines.

4.3.2 SHC anisotropies

Table 4.2 shows the calculated SHC of $MoTe_2$ and WTe_2 at E_F. SHC $\sigma^{\gamma}_{\alpha\beta}$ is a third-order tensor and represents the spin current along α direction generated by an electric field along β direction, where the spin current is polarized along γ direction.[159] $MoTe_2$ and WTe_2 exhibit more SHC anisotropies than heavy metals. Generally speaking, heavy metals, such as Pt, Pd, Au, α-Ta, β-Ta, α-W, β-W, have C_{4v} symmetry, which restricts their non-zero SHC as $\sigma^z_{xy} = -\sigma^z_{yx} = \sigma^x_{yz} = -\sigma^x_{zy} = \sigma^y_{zx} = -\sigma^y_{xz}$.[132, 135, 159–161] However, owing to the special symmetry, both $MoTe_2$ and WTe_2 have six non-zero SHC tensor elements of different magnitudes. For $MoTe_2$, the maximum of SHC is $\sigma^z_{yx} = -361$ $(\hbar/e)$S/cm, and $\sigma^y_{zx} = 286$ $(\hbar/e)$S/cm is also noticeable. For

Table 4.2: Non-zero SHC tensor elements in $MoTe_2$ and WTe_2 at E_F, in the unit of $(\hbar/e)$S/cm. SHA_{MAX} is defined as Eq. 4.2.

Semimetals	σ^x_{yz}	σ^x_{zy}	σ^y_{xz}	σ^y_{zx}	σ^z_{xy}	σ^z_{yx}	SHA_{MAX}
$MoTe_2$	−18	45	−88	286	−176	−361	−0.72
WTe_2	−44	−44	−61	103	−204	−15	−0.54

WTe_2, the maximum of SHC is $\sigma^z_{xy} = -204$ $(\hbar/e)$S/cm. Compared with SHC in heavy metals, the SHC in $MoTe_2$ and WTe_2 are considerable.[81, 82, 162] These results will provide helpful information for the experimental detection of the SHE.[163] We also calculated spin Hall angle. In Table 4.2, the SHA_{MAX} is defined as

$$SHA_{MAX} = \max_{\alpha,\beta,\gamma}(\sigma^{\gamma}_{\alpha\beta}(E_F))/\sigma_{xx} \tag{4.2}$$

where $\max_{\alpha,\beta,\gamma}(\sigma^{\gamma}_{\alpha\beta}(E_F))$ is the maximum SHC among all six tensor elements at E_F and σ_{xx} is the experimental result of charge conductivity. The conductivity of $MoTe_2$ is 1×10^3 S/cm,[164] and the conductivity of WTe_2 is 7.4×10^2 S/cm.[165] Calculated SHA_{MAX} is -0.72 for $MoTe_2$ and -0.54 for WTe_2. It can be seen that SHAs of $MoTe_2$ and WTe_2 are larger than the SHA of heavy metal Pt, which is only 0.076 according to experiments.[166, 167] The superior spin Hall properties in $MoTe_2$ and WTe_2 make it promising to realize the SOT vdW MTJ.

4.3.3 SHC tensor elements

Figure 4.11 presents the energy-resolved SHC. In the left panels of Fig. 4.11, $MoTe_2$ shows peaks around E_F for σ^z_{yx}, σ^y_{zx} and σ^z_{xy} tensors, as high as -390, 306 and -178 $(\hbar/e)$S/cm, respectively. The relatively high SHC, with an absolute value over 200 $(\hbar/e)$S/cm, remains from -0.5 eV to 0 eV for σ^z_{yx}. In the right panels of Fig. 4.11, WTe_2 exhibits an SHC of $\sigma^z_{yx} = -528$ $(\hbar/e)$S/cm at the energy point of $E = E_F - 0.094$ eV. High SHC around -400 $(\hbar/e)$S/cm occurs at $E = E_F + 0.47$ eV for σ^z_{xy}, and the σ^y_{zx} value reaches up to 370 $(\hbar/e)$S/cm at $E = E_F - 0.048$ eV. Discussions above indicate that tuning the position of E_F is an effective way to enhance SHC. Meanwhile, it has been demonstrated that transition metal doping atoms in the context of layered TMDC materials can modulate the position of E_F, hence improving their performance and extending their potential for applications.[168]

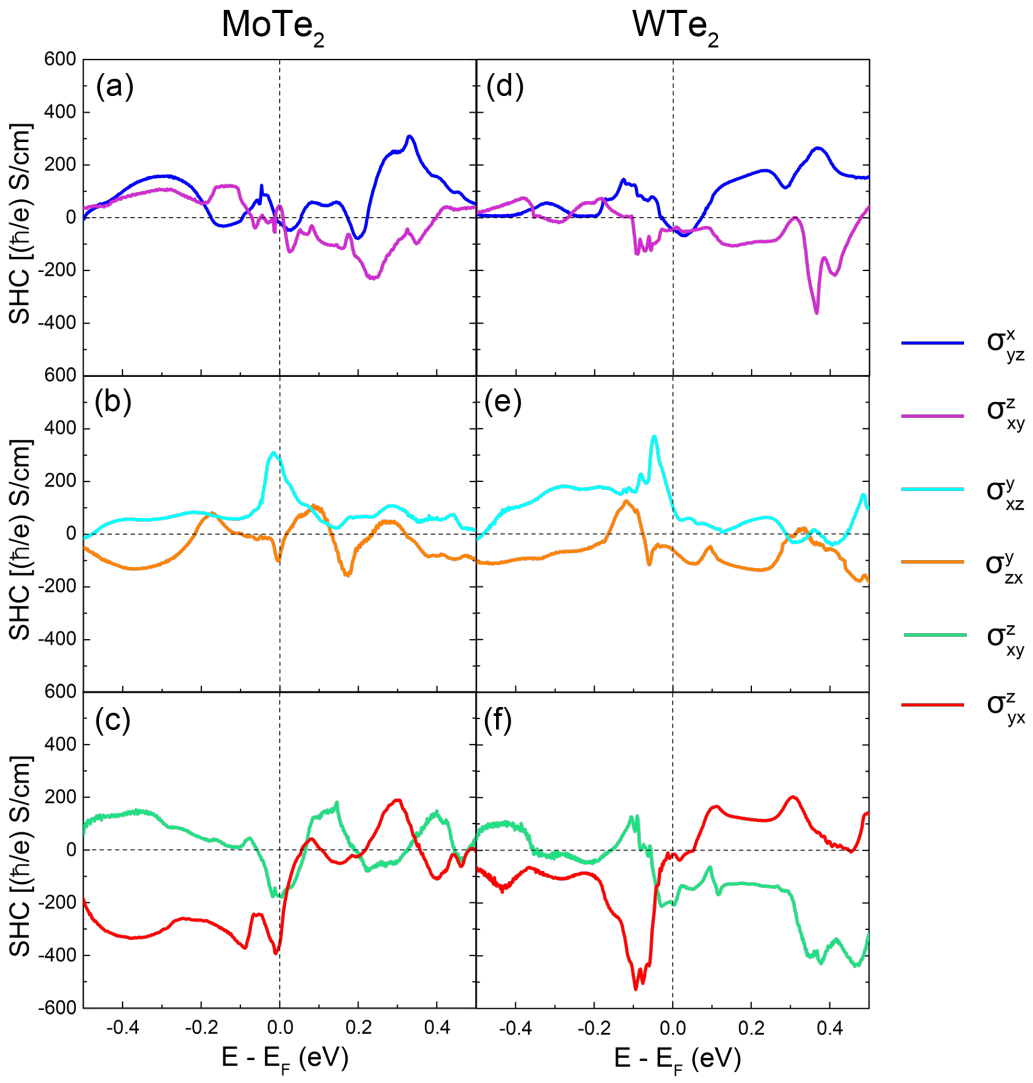

Figure 4.11: SHC tensor elements relative to the energy for (a)-(c) $MoTe_2$ and (d)-(f) WTe_2. Different colors represent different anisotropies.

4.3.4 Analysis of spin Berry curvature

To elucidate the underlying mechanism of the enhancement of SHC induced by E_F shift, we show the band structure projected by spin Berry curvature in Fig. 4.12. We take σ^z_{xy} in WTe_2 as an example, since it varies a lot and reverses its sign in a small energy range, from -204 $(\hbar/e)$S/cm at $E = E_F$ to 127 $(\hbar/e)$S/cm at $E = E_F - 0.09$ eV, marked by horizontal green dashed lines in Fig. 4.12(b). Figure 4.12(a) shows the band structure projected by spin Berry curvature $\Omega^z_{n,xy}(\boldsymbol{k})$ with the log scale, and

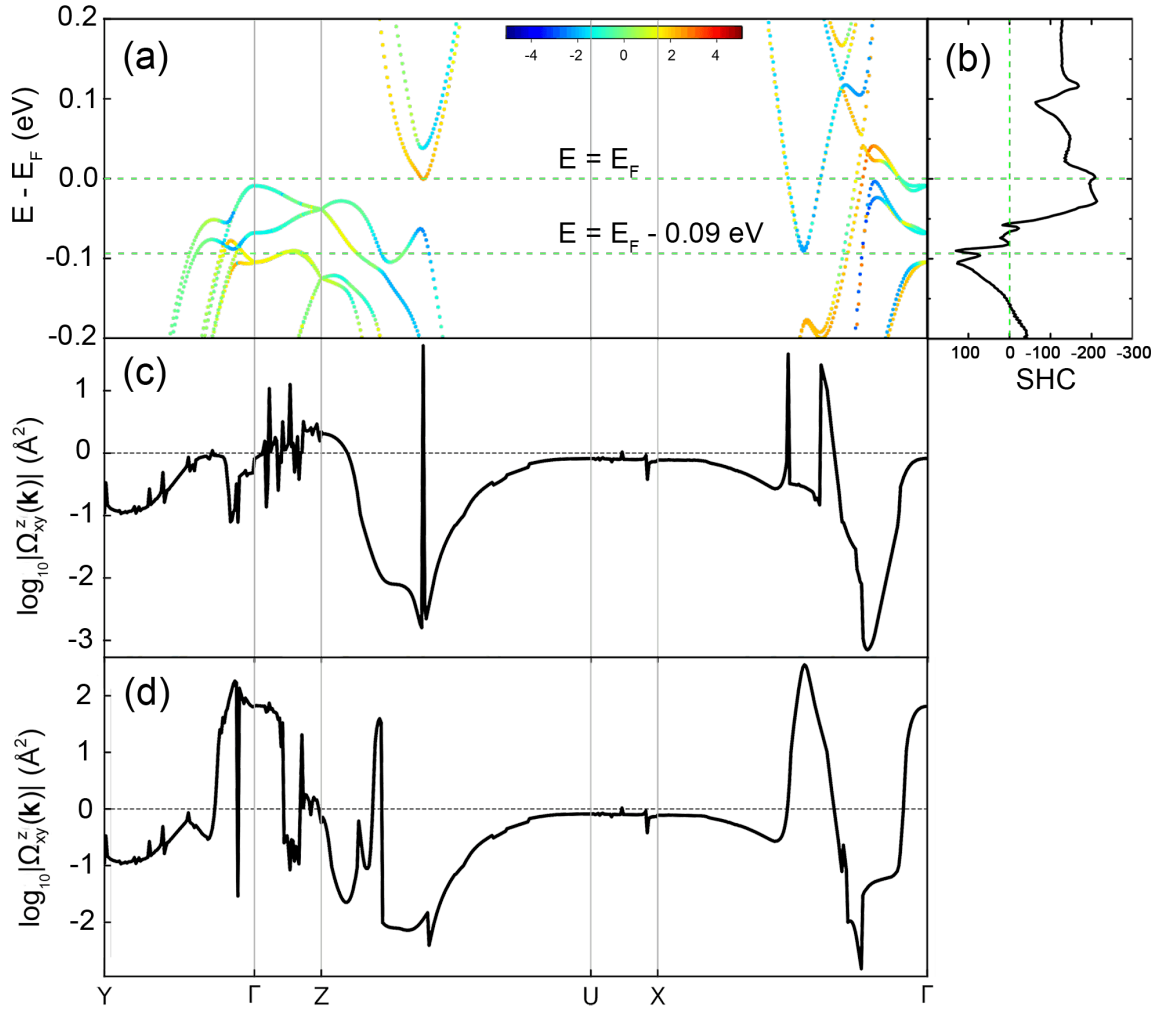

Figure 4.12: (a) Band structure projected by spin Berry curvature with log scale. (b) SHC σ^z_{xy} of WTe_2 versus energy. (c) and (d) are $\boldsymbol{k}$-resolved spin Berry curvatures at $E = E_F$ and $E = E_F - 0.09$ eV, respectively. Identical high symmetry points are used in (a), (c), and (d).

red (blue) color denotes the positive (negative) contribution of spin Berry curvature. It illustrates that the negative SHC at $E = E_F$ is due to the negative contribution along Z-U and X-Γ path. When the energy is shifted by -0.09 eV, positive spin Berry curvature arises and overwhelms the negative one, resulting in an SHC of 127 $(\hbar/e)$S/cm. To make it more intelligible, Figs. 4.12(c) and (d) show the $\boldsymbol{k}$-resolved spin Berry curvature with the log scale. At E_F, the negative spin Berry curvature

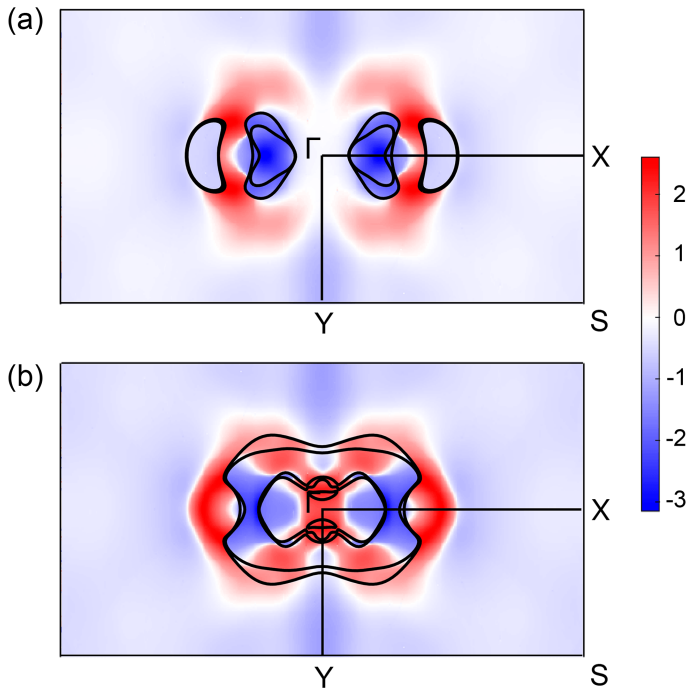

Figure 4.13: The $\boldsymbol{k}$-resolved spin Berry curvature with log scale in a slice of the 2D BZ at $k_z = 0$ for SHC σ^z_{xy} of WTe_2 at (a) $E = E_F$ and (b) $E = E_F - 0.09$ eV, respectively. High symmetry points are Γ (0, 0, 0), X (0.5, 0, 0), Y (0, 0.5, 0) and S (0.5, 0.5, 0). Black curves are the intersections of Fermi surface with the slice of BZ.

dominates along Z-U and X-Γ paths. Some sharp peaks are caused by the bands crossing with E_F. When E_F is shifted by -0.09 eV, the negative spin Berry curvature along X-Γ path weakens while the positive one strengthens, especially at the Γ point. As a result, SHC turns out to be positive. Remarkably, the spin Berry curvature varies dramatically along Γ-Z path. In such a case, the method of adaptive mesh refinement can be effective for efficient convergence of SHC calculation.[81]

Figure 4.13 shows the $\boldsymbol{k}$-resolved spin Berry curvature projected on the 2D slice of $k_z = 0$ in BZ. Figures 4.13(a) and (b) are the results at $E = E_F$ and $E = E_F - 0.09$ eV, respectively. The spin Berry curvature is also in the log scale and red (blue) color denotes a positive (negative) contribution. It can be seen that the spin Berry curvature depends sensitively on Fermi energy shift. The sign reverses throughout a large fraction of the 2D BZ, especially around Γ point. Figure 4.13(a) shows that at $E = E_F$, the

spin Berry curvature at Γ point is close to zero as shown by white color, and the negative region surrounded by black curves has large magnitude considering the log scale. At $E = E_F - 0.09$ eV in Fig. 4.13(b), the spin Berry curvature around Γ point becomes positive as shown by red color. Besides, the positive region expands widely and strengthens, while the negative region shrinks and weakens. The integration of spin Berry curvature in 2D BZ results in the reversal of SHC sign, from the negative one at $E = E_F$ to the positive one at $E = E_F - 0.09$ eV. The above analyses clarify the mechanism of SHC variation with the position of E_F, and shed light on the method to optimize SHC.

4.4 Summary

Traditional MgO-based MTJ faces the challenge of lattice mismatch, impeding the improvement of its performances. In this chapter, we propose the MTJ on the basis of vdW heterojunctions, which can be vertically stacked without the limitation of lattice match. Previous experiments have verified the room-temperature ferromagnetism of VSe_2 monolayer grown on the MoS_2 substrate. Fully considering the practical implementation, we proposed the vdW MTJ using $VSe_2/MoS_2/VSe_2$ stack and studied its properties.

NEGF-DFT calculations illustrate that at equilibrium state, the APC conductance of vdW MTJ is considerable, leading to the decline of TMR ratio. Analyses on wavefunctions illustrate that transmission states localize at certain layers, resulting in the quantum-well resonances and ultrahigh transmission coefficients close to unity. The bias voltage, which would suppress the resonances, can be an effective method to reduce the APC current and enhance the TMR ratio of vdW MTJ. Under the voltage control, a room-temperature TMR ratio up to 846% can be achieved, as well as a TMR ratio of 1277% at 100 K.

We put forward the concept of SOT vdW MTJ, where MoS_2 is used as the bottom layer for writing current and SOT switching. We calculated the SHC of MoS_2. It turns out that at E_F, SHC of MoS_2 is only -34 $(\hbar/e)$S/cm, and it can reach up to 400 $(\hbar/e)$S/cm at $E = E_F -$ 2.0 eV. The tunable SHC of MoS_2 brings the possibility to realize SOT switching in the vdW MTJ.

To find out the material with intrinsic high SHC at E_F, we investigate semimetals $MoTe_2$ and WTe_2. Superior to MoS_2, $MoTe_2$ exhibits a noticeable SHC of $\sigma^z_{yx} = -361$ $(\hbar/e)$S/cm at E_F, and WTe_2 shows an SHC of $\sigma^z_{xy} = -204$ $(\hbar/e)$S/cm at E_F. Both semimetals exhibit large SHA, which can be attributed to high SHC and low electrical conductivity of the semimetal. The superior spin Hall properties in $MoTe_2$ and WTe_2 make it promising to realize the SOT vdW MTJ. Intriguingly, because of the reduced structural symmetry, $MoTe_2$ and WTe_2 exhibit unusually diverse SHC elements of different magnitudes. Analyses of spin Berry curvature have also been presented to clarify the mechanism of SHC. Investigations above would promote the practical applications of 2D spintronics devices, and provide new concepts for their future developments.

Chapter 5

2D spin injection system

5.1 Introduction

2D materials show great potential for the realization of spin logic devices.[99, 169–171] With the characters of massless Dirac fermion and weak SOC, graphene is an extraordinary material for spin transport in logic devices.[93–95, 98] One of the most promising applications of graphene is the field effect transistor (FET), which requires the opening and controlling of the energy gap. However, monolayer graphene remains zero-gap semimetallic under an external vertical electric field since it has two equivalent planar sublattices, making it difficult to operate the graphene FET. Great efforts have been devoted to the research on 2D materials with a controllable energy gap. Thanks to the successful experimental synthesis,[172, 173] silicene, the monolayer consisting of Si atoms, is attracting increasing attention.[174, 175] Similar to graphene, silicene has the hexagonal structure and the Dirac cone at K point composed by p orbitals of Si atoms.[174] Superior to graphene, silicene overcomes the problem of compatibility with the present silicon-based semiconductor technology.[176] More intriguingly, it has been predicted that tunable gap can be opened in silicene by applying vertical electrical field due to its buckling structure.[177, 178] Thanks to the innovation of encapsulated

delamination transfer method, experimentalists successfully prepared a silicene FET, where a small gap was opened.[179] Works above demonstrate that it is practical to exploit silicene as the transport channel and realize the switching functionality of spin-FET. On the other hand, despite the abundant achievements in graphene spintronics, the spin device using silicene as the transport channel remains absent. In this chapter, we will discuss the spin injection system based on silicene as well as its spin-resolved performance.

5.2 Spin injection in Fe/silicene system

We propose a spin injection system, where Fe(111)/silicene stack acts as the spin injector, and silicene is used to be the spin transport channel. Through NEGF-DFT calculations, we revealed the remarkable spin injection efficiency under bias. The density of states of Fe(111)/silicene stack as well as the energy-resolved transmission spectra have been analyzed to understand the physical mechanism.

5.2.1 Atomic model and method

The spin transport system is composed of Fe(111)/silicene stack and pure silicene channel. Figure 5.1 shows its atomic model, Fig. 5.1(a) is the side view, Fig. 5.1(b) is the top view. Fe(111)/silicene stack is the spin injector and generates spin-polarized current. The pure silicene is the spin transport channel where spin-polarized current propagates. The spin transport is along x direction, and the scattering length along the transport direction, excluding left and right electrodes, is 26.74 Å. The system extends periodically in y direction, and the normal direction of silicene plane is z direction where vacuum layer exists. The unit cell of Fe(111)/silicene stack is shown in the red box, and the lattice constant is kept to 3.86 Å according to the lattice constant of silicene.[180] Note that the lattice constant of bcc Fe is 2.866 Å,[131] thus

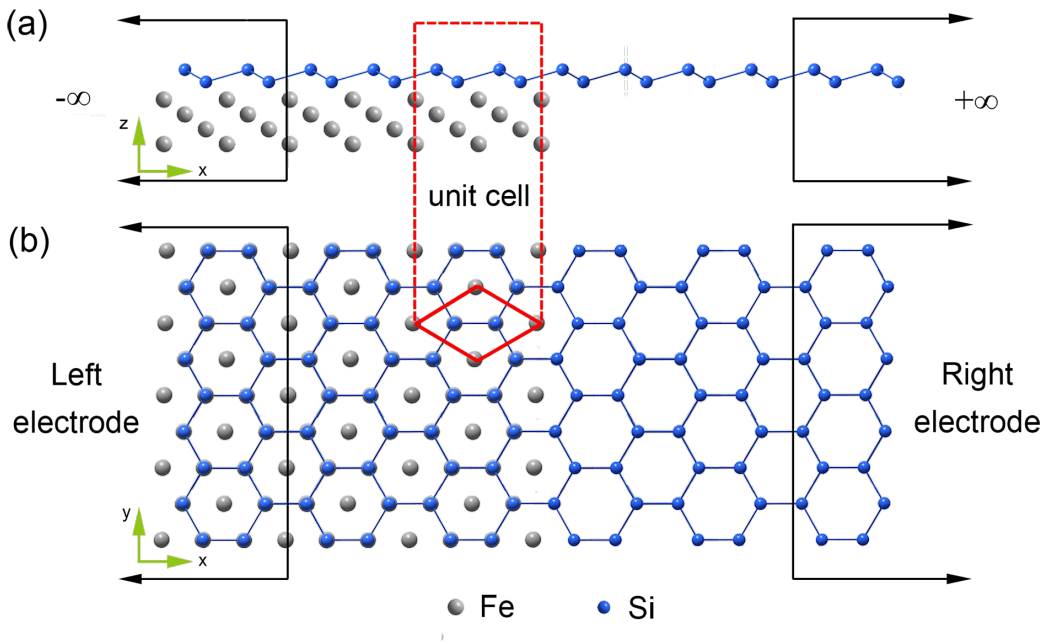

Figure 5.1: Diagram of the spin injection system. The black arrows indicate the left and right electrodes, extending to $\pm\infty$ and consisting of Fe(111)/silicene stack (left electrode) and pure silicene (right electrode). The center part is the scattering region. The red box indicates the unit cell of Fe(111)/silicene stack. (a) The side view. (b) The top view.

the lattice constant of hexagonal Fe(111) section is $2.866 \times \sqrt{2} = 4.053$ Å. For the match between Fe(111) and silicene, the Fe is homogeneously strained by less than 5% in this model. Buckling distance in silicene 0.46 Å.[180]

The configuration of Fe(111)/silicene unit cell was validated by the interlayer spacing test using VASP with a $33 \times 33 \times 1$ $\boldsymbol{k}$-mesh.

Figure 5.2 shows the details about interlayer spacing test. The binding energies of six different configurations have been checked for varying Fe(111)/silicene interlayer spacing. Our result illustrates that the most stable configuration is "$B_{up}C_{down}$" configuration with 1.1 Å interlayer spacing, which has the largest binding energy. We briefly discuss the experimental feasibility of this device. DFT calculations of phonon dispersion have proved that the structure of silicene is dynamically stable,[174, 178] consequently it is possible to move silicene onto another substrate. Later on, experi-

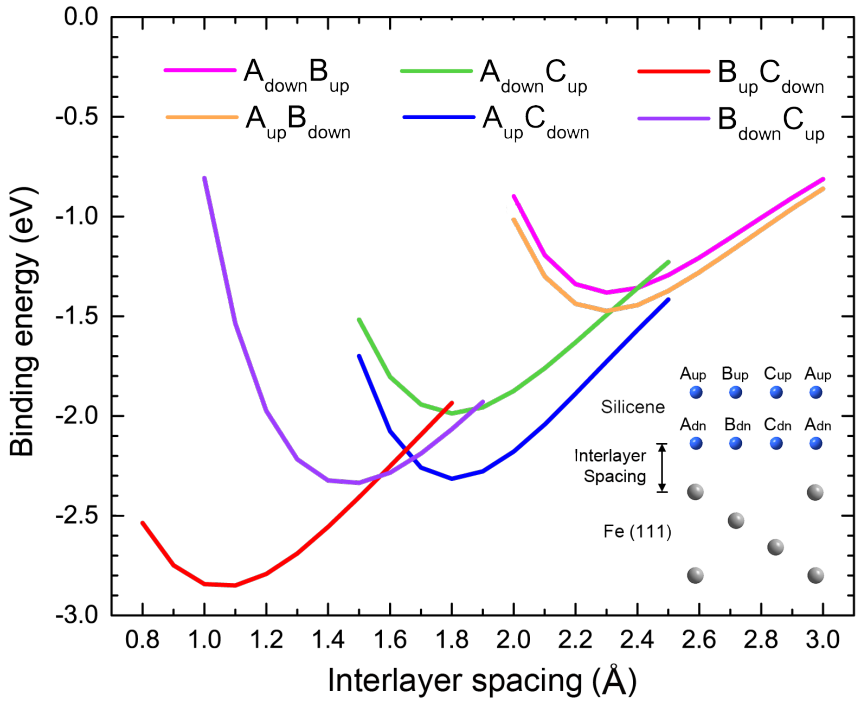

Figure 5.2: Binding energy of a silicene monolayer on Fe(111) surface as a function of the stack configuration and the interlayer spacing. Different kinds of stack configuration are shown in the inset.

mental works put forward a method to transfer silicene by the encapsulation through Al_2O_3 capping layer.[179, 181] Based on works above, we assume that silicene can be transferred onto the Fe(111) layer, meanwhile the silicene buckling structure is well preserved.

NanoDCAL package was employed for the calculations of transport properties. A $1 \times 21 \times 1$ $\boldsymbol{k}$-mesh was used for the self-consistent calculation of the whole system, and a dense sampling of $1 \times 500 \times 1$ was employed for the transmission calculation. GGA-PBE exchange-correlation potential [109] was used in all calculations.

5.2.2 Bias-dependent SIE

Using the atomic model introduced above, we calculate the spin-resolved transport properties. Spin-resolved currents and total currents are shown in Fig. 5.3(a). It can

be observed that at finite positive bias voltage, the minority-spin current is remarkably higher than the majority-spin current. Minority-spin current increases rapidly with bias, while majority-spin current remains close to zero until the bias reaches up to 50

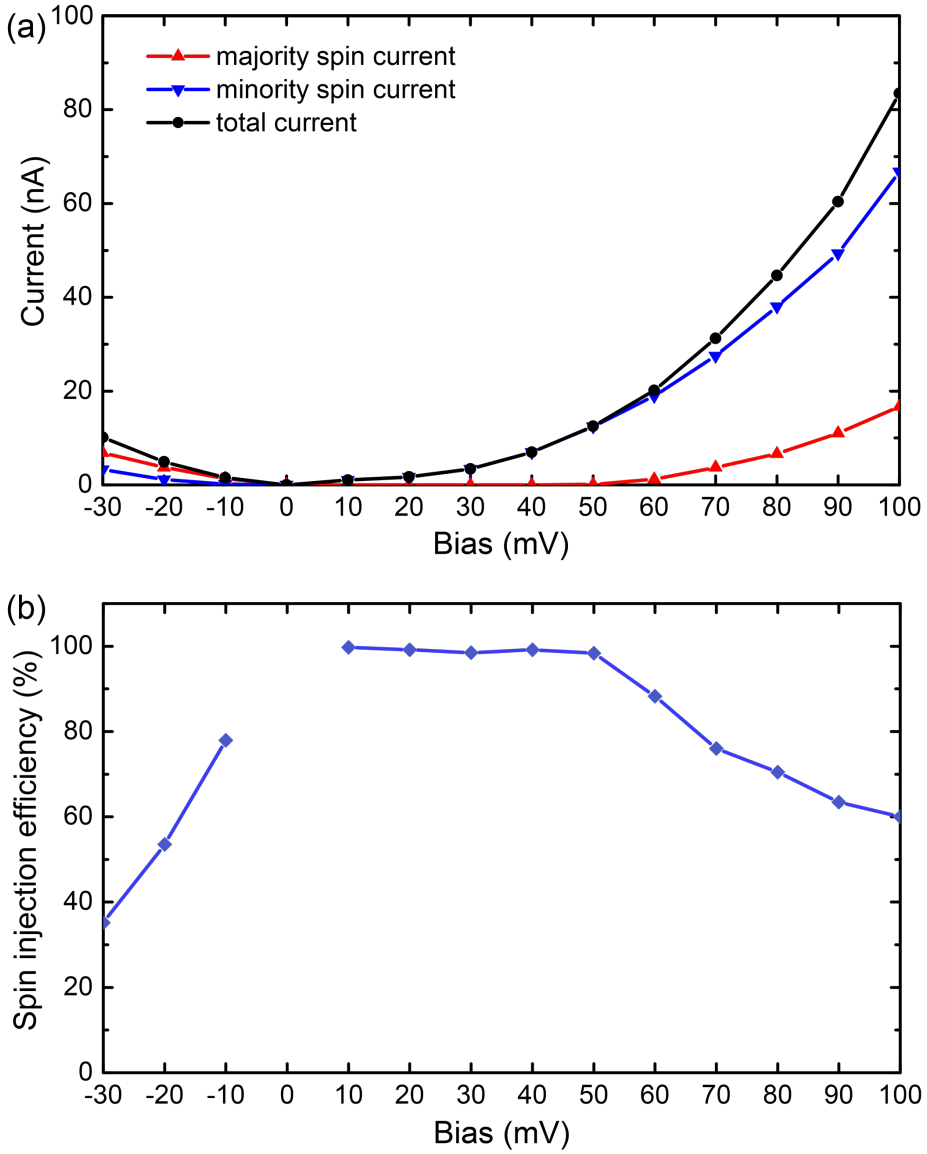

Figure 5.3: Transport properties of the spin injection system in non-equilibrium states. (a) Spin-resolved and total currents. The red line with up-pointing triangles and blue line with down-pointing triangles indicate the majority-spin current and minority-spin current, respectively. The black line with dots denotes the total current. (b) Spin injection efficiencies defined as 5.1.

mV. For the negative bias, the condition is different. Both majority-spin and minority-spin currents are arising with increasing bias, and majority-spin current is higher than the minority-spin current.

On the basis of spin-dependent currents, the non-equilibrium spin injection efficiency SIE is defined as

$$\mathrm{SIE} = \left| \frac{\mathrm{I}^{\uparrow} - \mathrm{I}^{\downarrow}}{\mathrm{I}^{\uparrow} + \mathrm{I}^{\downarrow}} \right| \times 100\%, \tag{5.1}$$

where $\mathrm{I}^{\uparrow}$ is the majority-spin current and $\mathrm{I}^{\downarrow}$ is the minority-spin current. Fig. 5.3(b) presents SIEs at various bias excluding the zero bias point due to the nonexistence of current. It shows that for the positive bias, SIE is close to 100% in the bias range from 10 mV to 50 mV. This perfect spin filtering effect can be attributed to the overwhelming minority-spin current. The decline of SIE starts from 60 mV, because at this bias point, the majority-spin current begins to rise and compete with the minority-spin current. For the negative bias, SIE decreases with the increasing bias owing to the comparable majority- and minority-spin currents.

5.2.3 Analysis of band structures

To understand the remarkable SIEs, we investigate the projected band structure and the partial density of states (PDOS) of the Fe(111)/silicene unit cell. Figures 5.4(a) and (b) show the majority-spin and minority-spin bands, respectively. The black up-triangles (blue down-triangles) denote p orbitals of the high-position (low-position) Si atom, and the red dots represent the d orbitals of Fe atoms. In pure silicene monolayer, the Dirac cone at K point is composed by the p orbitals of Si atoms.[174] However, due to the existence of Fe layers, the Dirac cone of silicene disappears in the band structure of Fe(111)/silicene stack. For the majority spin, p bands of Si atoms cross the E_F. For the minority spin, d bands of Fe atoms cross the E_F. Figure 5.4(c) presents the PDOS of all Fe atoms in the Fe(111)/silicene stack. It can be seen that majority-spin states

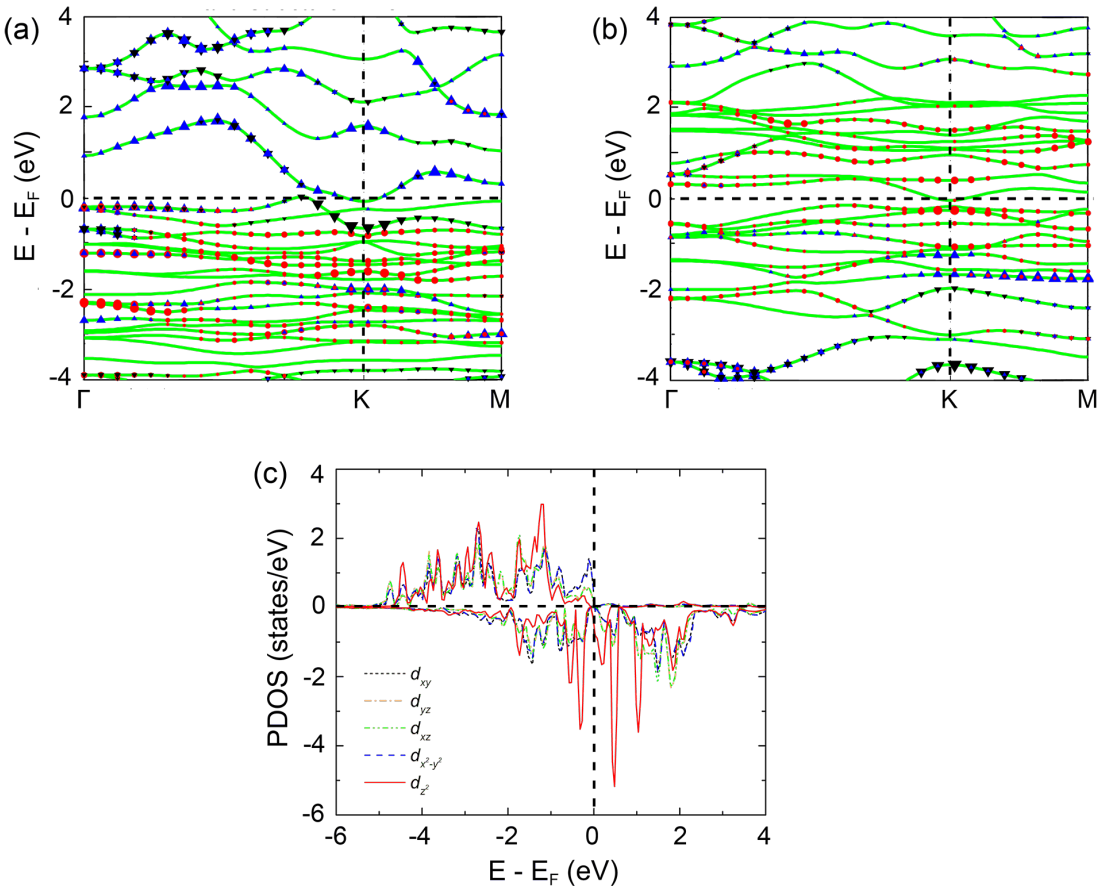

Figure 5.4: Band structure of Fe(111)/silicene unit cell stack for (a) majority-spin states and (b) minority-spin states. Black up-triangles (blue down-triangles) show the p orbitals of the high-position (low-position) Si atom, and the red dots represent the d orbitals of Fe atoms. (c) Projected density of states of Fe atoms in the Fe(111)/silicene stack.

are obviously suppressed above E_F. Consequently, the minority-spin states contribute primarily to the total current. In details, d_{z^2} orbital is prominent, as shown by the red line in Fig. 5.4(c). Dominant minority-spin component induces the spin-filtering effect, resulting in high minority-spin current and remarkable SIE in the transport system. Below E_F, there are both majority-spin and minority-spin states, making two kinds of current comparable. Thus, SIE is relatively trivial under the negative bias. The above analyses of PDOS clarify the obvious difference between majority-spin current and minority-spin current at non-equilibrium states.

5.2.4 Transmission spectra

Energy-resolved transmission spectra T(E, V) at finite bias are shown in Fig. 5.5. Current is obtained by integrating transmission coefficients in the bias window $-V/2 \leq E \leq +V/2$, denoted by vertical green dashed lines. Figure 5.5(a) presents that for

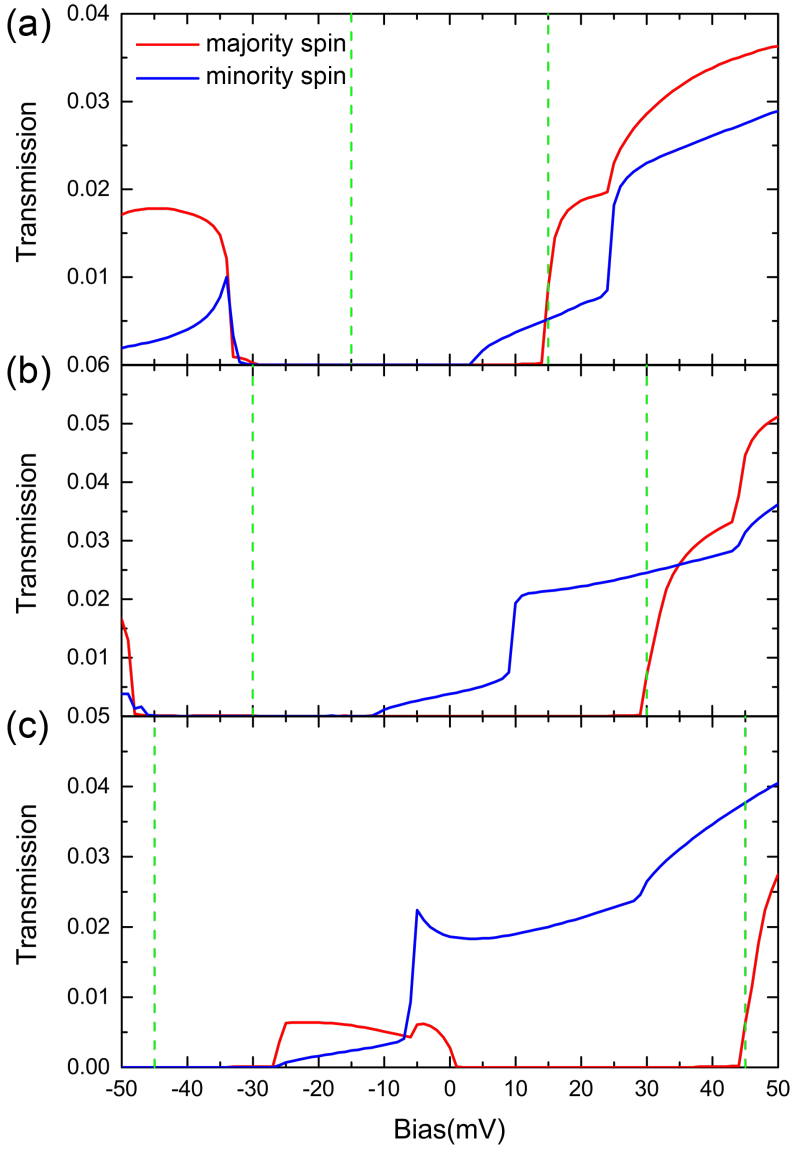

Figure 5.5: Energy-resolved transmission spectra of the system under different bias V. (a) $V = 30$ mV. (b) $V = 60$ mV. (c) $V = 90$ mV. The bias window is denoted by the two green dashed lines.

30 mV bias, the bias window nearly locates in the transmission gap for majority-spin states, resulting in a dominant minority-spin current and a nearly 100% SIE, as shown in Fig. 5.3. Figure 5.5(b) shows that for 60 mV bias, minority-spin transmission strengthens with the increasing bias, while majority-spin transmission is still suppressed by a transmission gap. Figure 5.5(c) illustrates that for the 90 mV bias, majority-spin transmission peak moves into the bias window, consequently, the difference between majority-spin current and minority-spin current narrows, making SIE decline as shown in Fig. 5.3(b). The transmission spectra agree well to the spin-resolved I-V curves, further explains the mechanisms of high SIEs.

5.3 Summary

The spintronics device based on silicene has desirable advantages, such as the controllable switching operation induced by vertical electric field, the compatibility with silicon semiconductor technology, as well as the long spin diffusion length. In this chapter, we designed a spin injection system, where the Fe(111)/silicene stack acts as a spin injector, and silicene is used to be the spin transport channel. The most stable configuration of Fe(111)/silicene stack and the experimental feasibility of this device have been fully considered.

We focus on the performance of SIE, which is proportional to the difference between majority- and minority-spin currents. NEGF-DFT calculations reveal that in a certain range of positive bias, the minority-spin current dominates in the non-equilibrium transport, making the system exhibit high SIEs close to 100%.

To understand the extraordinary phenomenon, the spin-resolved band and density of states of the Fe(111)/silicene stack have been investigated. It shows that the majority-spin states are suppressed above Fermi energy, leading to an overwhelming minority-spin current under the positive bias. To present more details of transmission

coefficients in bias windows, energy-resolved transmission spectra were also studied. Considering silicene is an ideal switchable transport channel superior to graphene, this proposal of silicene device would help to develop spin-FET and other spin logic devices.

Chapter 6

Summary and perspectives

In this thesis, we have investigated spin-dependent quantum transport through *ab initio* calculations. To design high-performance spintronic devices, we investigated the tunneling magnetoresistance effects in magnetic tunnel junctions, the spin Hall effect in heavy metals and TMDCs, as well as the spin injection efficiency in silicene system.

We firstly designed the MgO-based MTJs with heavy metals including Ta, W, Mo, and Ir, and theoretically studied the modulation on TMR effects induced by HMs. It has been found that different HMs lead to diverse transmission channel spectra, which affect the spin-resolved transmission spectra and conductance of MTJs. Interestingly, due to the absence of Δ_1 band crossing Fermi energy in Mo metal, the centered majority-spin transmission peak disappears in the PC of Mo-MTJ. Meanwhile, interfacial resonant states primarily contribute to the minority-spin conductance in PC, resulting in high TMR in Mo-MTJ. Moreover, due to the ultralow conductance in APC, W-MTJ and Ir-MTJ are able to present remarkable TMR effects.

To reveal HMs which are efficient for the SOT switching of MTJs, we studied SHE and calculated the intrinsic spin Hall conductivity of Mo and Ir metals. We have found that the SHC of Mo is -412 $(\hbar/\mathrm{e})\mathrm{S/cm}$ at E_F, and the SHC of Ir is 403 $(\hbar/\mathrm{e})\mathrm{S/cm}$ at E_F. Intriguingly, we realize the SHC enhancement of Ir alloys. Exploiting substitution

doping, an SHC of 1475 ($\hbar$/e)S/cm is achievable in $Ir_{0.75}Au_{0.25}$ alloy, over three times as large as the SHC of Ir metal. Works above clarify the TMR and SHE modulations induced by HMs, and provide guidelines to optimize reading and writing performances through selecting HMs in MTJs.

Despite the great progress in MgO-based MTJs, the mismatch problem between ferromagnetic electrodes and tunnel layer is difficult to overcome. Advances in van der Waals materials enable a bond-free integration strategy without lattice limitation. Inspired by the observation of room-temperature ferromagnetism in VSe_2 grown on MoS_2, we proposed vdW MTJs on basis of VSe_2/MoS_2 heterojunction. Quantum-well resonances in vdW MTJs are highlighted, and voltage control has been demonstrated to be an effective method to modulate TMR ratio, which can reach up to 846% at room temperature and 1277% at 100 K temperature.

We put forward the concept of SOT vdW MTJ, which is fully composed of vdW materials and switched by the SOT in bottom vdW layer. To find out the desirable vdW materials for SOT switching, we studied the SHC of type-II Weyl semimetals $MoTe_2$ and WTe_2. It turns out that $MoTe_2$ can exhibit a noticeable SHC of $\sigma^z_{yx} = -361$ ($\hbar$/e)S/cm at E_F. Thanks to the reduced symmetry, extraordinarily diverse SHC anisotropies have been found in $MoTe_2$ and WTe_2. It is worth stressing that due to the high SHC and low electrical conductivity, large spin Hall angle can be expected in these two semimetals.

Lastly, motivated by the demand of a 2D switchable device with long spin diffusion length, we proposed the spin injection system with the silicene as spin transport channel and the Fe(111)/silicene stack as spin injector. It has been proved that at non-equilibrium states, this spin injection system can exhibit high spin injection efficiencies close to 100%, originating from the unique spin-resolved density of states of the Fe(111)/silicene stack. Works above present the potential of 2D spintronics

devices, as well as the new concepts for their future developments.

In summary, in this thesis, we propose spintronics devices with high performances through *ab initio* calculations. Our works would shed light on the mechanisms of spin-resolved phenomenon as well as promote the spintronics applications.

Our future work will focus on the computation of SOT and the investigation of spin dynamics in MTJs. We intend to extract the key parameters from *ab initio* calculations of the spin Hall effects and interfacial Dzyaloshinskii-Moriya interactions. Then we would build the model on extensive scale to simulate the real process of spin dynamics, and observe the spin precession and SOT switching. We believe plenty of novel phenomena can be discovered in 2D systems thanks to the ultrathin layers and flat surfaces of vdW materials.

References

[1] S. A. Wolf, D. D. Awschalom, R. A. Buhrman, J. M. Daughton, S. von Molnár, M. L. Roukes, A. Y. Chtchelkanova, and D. M. Treger, "Spintronics: A spin-based electronics vision for the future", Science **294**, 1488–1495 (2001).

[2] I. Žutić, J. Fabian, and S. Das Sarma, "Spintronics: Fundamentals and applications", Rev. Mod. Phys. **76**, 323–410 (2004).

[3] S. Tehrani, J. M. Slaughter, M. Deherrera, B. N. Engel, N. D. Rizzo, J. Salter, M. Durlam, R. W. Dave, J. Janesky, B. Butcher, K. Smith, and G. Grynkewich, "Magnetoresistive random access memory using magnetic tunnel junctions", Proc. IEEE **91**, 703–714 (2003).

[4] E. Chen, D. Apalkov, Z. Diao, A. Driskill-Smith, D. Druist, D. Lottis, V. Nikitin, X. Tang, S. Watts, S. Wang, S. A. Wolf, A. W. Ghosh, J. W. Lu, S. J. Poon, M. Stan, W. H. Butler, S. Gupta, C. K. A. Mewes, T. Mewes, and P. B. Visscher, "Advances and future prospects of spin-transfer torque random access memory", IEEE Trans. Magn. **46**, 1873–1878 (2010).

[5] S. Mühlbauer, B. Binz, F. Jonietz, C. Pfleiderer, A. Rosch, A. Neubauer, R. Georgii, and P. Böni, "Skyrmion lattice in a chiral magnet", Science **323**, 915–919 (2009).

[6] V. Baltz, A. Manchon, M. Tsoi, T. Moriyama, T. Ono, and Y. Tserkovnyak, "Antiferromagnetic spintronics", Rev. Mod. Phys. **90**, 015005 (2018).

[7] I. A. Sergienko and E. Dagotto, "Role of the Dzyaloshinskii-Moriya interaction in multiferroic perovskites", Phys. Rev. B **73**, 094434 (2006).

[8] Y. L. Chen, J. G. Analytis, J.-H. Chu, Z. K. Liu, S.-K. Mo, X. L. Qi, H. J. Zhang, D. H. Lu, X. Dai, Z. Fang, S. C. Zhang, I. R. Fisher, Z. Hussain, and Z.-X. Shen, "Experimental realization of a three-dimensional topological insulator, Bi_2Te_3", Science **325**, 178–181 (2009).

[9] J. Qiao, S. Peng, Y. Zhang, H. Yang, and W. Zhao, "First-principles investigation of magnetocrystalline anisotropy oscillations in Co_2FeAl/Ta heterostructures", Phys. Rev. B **97**, 054420 (2018).

[10] J. Sinova, S. O. Valenzuela, J. Wunderlich, C. H. Back, and T. Jungwirth, "Spin Hall effects", Rev. Mod. Phys. **87**, 1213–1260 (2015).

[11] S. Peng, D. Zhu, J. Zhou, B. Zhang, A. Cao, M. Wang, W. Cai, K. Cao, and W. Zhao, "Modulation of heavy metal/ferromagnetic metal interface for high-performance spintronic devices", Adv. Electron. Mater. **5**, 1900134 (2019).

[12] W. S. Zhao, T. Devolder, Y. Lakys, J. O. Klein, C. Chappert, and P. Mazoyer, "Design considerations and strategies for high-reliable STT-MRAM", Microelectron. Reliab. **51**, 1454–1458 (2011).

[13] S. Bhatti, R. Sbiaa, A. Hirohata, H. Ohno, S. Fukami, and S. N. Piramanayagam, "Spintronics based random access memory: A review", Mater. Today **20**, 530–548 (2017).

[14] S. Chung, T. Kishi, J. W. Park, M. Yoshikawa, K. S. Park, T. Nagase, K. Sunouchi, H. Kanaya, G. C. Kim, K. Noma, M. S. Lee, A. Yamamoto, K. M. Rho, K. Tsuchida, S. J. Chung, J. Y. Yi, H. S. Kim, Y. S. Chun, H. Oyamatsu, and S. J. Hong, "4Gbit density STT-MRAM using perpendicular MTJ realized

with compact cell structure", in 2016 IEEE Int. Electron Devices Meet. (IEDM) (Dec. 2016), pp. 27.1.1–27.1.4.

[15] J. Zhu, "Magnetoresistive random access memory: The path to competitiveness and scalability", Proc. IEEE **96**, 1786–1798 (2008).

[16] D. Apalkov, B. Dieny, and J. M. Slaughter, "Magnetoresistive random access memory", Proc. IEEE **104**, 1796–1830 (2016).

[17] Z. Wang, M. Saito, K. P. McKenna, S. Fukami, H. Sato, S. Ikeda, H. Ohno, and Y. Ikuhara, "Atomic-scale structure and local chemistry of CoFeB–MgO magnetic tunnel junctions", Nano Lett. **16**, 1530–1536 (2016).

[18] B. G. Park, J. Wunderlich, X. Martí, V. Holý, Y. Kurosaki, M. Yamada, H. Yamamoto, A. Nishide, J. Hayakawa, H. Takahashi, A. B. Shick, and T. Jungwirth, "A spin-valve-like magnetoresistance of an antiferromagnet-based tunnel junction", Nat. Mater. **10**, 347–351 (2011).

[19] H. Sato, M. Yamanouchi, S. Ikeda, S. Fukami, F. Matsukura, and H. Ohno, "MgO/CoFeB/Ta/CoFeB/MgO recording structure in magnetic tunnel junctions with perpendicular easy axis", IEEE Trans. Magn. **49**, 4437–4440 (2013).

[20] T. Nozaki, N. Tezuka, and K. Inomata, "Quantum oscillation of the tunneling conductance in fully epitaxial double barrier magnetic tunnel junctions", Phys. Rev. Lett. **96**, 027208 (2006).

[21] Z. Wang, W. Zhao, E. Deng, J.-O. Klein, and C. Chappert, "Perpendicular-anisotropy magnetic tunnel junction switched by spin-Hall-assisted spin-transfer torque", J. Phys. D: Appl. Phys. **48**, 065001 (2015).

[22] B. Dieny, R. C. Sousa, J. Herault, C. Papusoi, G. Prenat, U. Ebels, D. Houssameddine, B. Rodmacq, S. Auffret, and L. D. B. Prejbeanu, "Spin-transfer effect and its use in spintronic components", Int. J. Nanotechnol. **7**, 591 (2010).

[23] K. Jabeur, G. D. Pendina, G. Prenat, L. D. Buda-Prejbeanu, and B. Dieny, "Compact modeling of a magnetic tunnel junction based on spin orbit torque", IEEE Trans. Magn. **50**, 1–8 (2014).

[24] M. Julliere, "Tunneling between ferromagnetic films", Phys. Lett. A **54**, 225–226 (1975).

[25] T. Miyazaki and N. Tezuka, "Giant magnetic tunneling effect in Fe/Al_2O_3/Fe junction", J. Magn. Magn. Mater. **139**, L231–L234 (1995).

[26] J. S. Moodera, L. R. Kinder, T. M. Wong, and R. Meservey, "Large magnetoresistance at room temperature in ferromagnetic thin film tunnel junctions", Phys. Rev. Lett. **74**, 3273–3276 (1995).

[27] D. Wang, C. Nordman, J. M. Daughton, Z. Qian, and J. Fink, "70% TMR at room temperature for SDT sandwich junctions with CoFeB as free and reference Layers", IEEE Trans. Magn. **40**, 2269–2271 (2004).

[28] M. Tanaka and Y. Higo, "Large tunneling magnetoresistance in GaMnAs /AlAs /GaMnAs ferromagnetic semiconductor tunnel junctions", Phys. Rev. Lett. **87**, 026602 (2001).

[29] M. Guth, A. Dinia, G. Schmerber, and H. A. M. van den Berg, "Tunnel magnetoresistance in magnetic tunnel junctions with a ZnS barrier", Appl. Phys. Lett. **78**, 3487–3489 (2001).

[30] W. H. Butler, X.-G. Zhang, S. Vutukuri, M. Chshiev, and T. C. Schulthess, "Theory of tunneling magnetoresistance for epitaxial systems", IEEE Trans. Magn. **41**, 2645–2648 (2005).

[31] W. H. Butler, X.-G. Zhang, T. C. Schulthess, and J. M. MacLaren, "Spin-dependent tunneling conductance of Fe|MgO|Fe sandwiches", Phys. Rev. B **63**, 054416 (2001).

[32] J. Mathon and A. Umerski, "Theory of tunneling magnetoresistance of an epitaxial Fe/MgO/Fe(001) junction", Phys. Rev. B **63**, 220403 (2001).

[33] S. Yuasa, "Giant tunneling magnetoresistance in MgO-based magnetic tunnel junctions", J. Phys. Soc. Jpn. **77**, 031001 (2008).

[34] D. Waldron, V. Timoshevskii, Y. Hu, K. Xia, and H. Guo, "First principles modeling of tunnel magnetoresistance of Fe/MgO/Fe trilayers", Phys. Rev. Lett. **97**, 226802 (2006).

[35] Y. Ke, K. Xia, and H. Guo, "Oxygen-vacancy-induced diffusive scattering in Fe/MgO/Fe magnetic tunnel junctions", Phys. Rev. Lett. **105**, 236801 (2010).

[36] S.-Z. Wang, K. Xia, and G. E. W. Bauer, "Thermoelectricity and disorder of FeCo/MgO/FeCo magnetic tunnel junctions", Phys. Rev. B **90**, 224406 (2014).

[37] S. Yuasa, T. Nagahama, A. Fukushima, Y. Suzuki, and K. Ando, "Giant room-temperature magnetoresistance in single-crystal Fe/MgO/Fe magnetic tunnel junctions", Nat. Mater. **3**, 868 (2004).

[38] S. S. P. Parkin, C. Kaiser, A. Panchula, P. M. Rice, B. Hughes, M. Samant, and S.-H. Yang, "Giant tunnelling magnetoresistance at room temperature with MgO (100) tunnel barriers", Nat. Mater. **3**, 862–867 (2004).

[39] Y. M. Lee, J. Hayakawa, S. Ikeda, F. Matsukura, and H. Ohno, "Effect of electrode composition on the tunnel magnetoresistance of pseudo-spin-valve magnetic tunnel junction with a MgO tunnel barrier", Appl. Phys. Lett. **90**, 212507 (2007).

[40] S. Ikeda, J. Hayakawa, Y. Ashizawa, Y. M. Lee, K. Miura, H. Hasegawa, M. Tsunoda, F. Matsukura, and H. Ohno, "Tunnel magnetoresistance of 604% at 300K by suppression of Ta diffusion in CoFeB/MgO/CoFeB pseudo-spin-valves annealed at high temperature", Appl. Phys. Lett. **93**, 082508 (2008).

[41] C. Burrowes, N. Vernier, J.-P. Adam, L. Herrera Diez, K. Garcia, I. Barisic, G. Agnus, S. Eimer, J.-V. Kim, T. Devolder, A. Lamperti, R. Mantovan, B. Ockert, E. E. Fullerton, and D. Ravelosona, "Low depinning fields in Ta-CoFeB-MgO ultrathin films with perpendicular magnetic anisotropy", Appl. Phys. Lett. **103**, 182401 (2013).

[42] B. Dieny and M. Chshiev, "Perpendicular magnetic anisotropy at transition metal/oxide interfaces and applications", Rev. Mod. Phys. **89**, 025008 (2017).

[43] S. Ikeda, K. Miura, H. Yamamoto, K. Mizunuma, H. D. Gan, M. Endo, S. Kanai, J. Hayakawa, F. Matsukura, and H. Ohno, "A perpendicular-anisotropy CoFeB–MgO magnetic tunnel junction", Nat. Mater. **9**, 721 (2010).

[44] M.-S. Jeon, K.-S. Chae, D.-Y. Lee, Y. Takemura, S.-E. Lee, T.-H. Shim, and J.-G. Park, "The dependency of tunnel magnetoresistance ratio on nanoscale thicknesses of $Co_2Fe_6B_2$ free and pinned layers for $Co_2Fe_6B_2$/MgO-based perpendicular-magnetic-tunnel-junctions", Nanoscale **7**, 8142–8148 (2015).

[45] H. D. Gan, H. Sato, M. Yamanouchi, S. Ikeda, K. Miura, R. Koizumi, F. Matsukura, and H. Ohno, "Origin of the collapse of tunnel magnetoresistance at high annealing temperature in CoFeB/MgO perpendicular magnetic tunnel junctions", Appl. Phys. Lett. **99**, 252507 (2011).

[46] H. Almasi, C. L. Sun, X. Li, T. Newhouse-Illige, C. Bi, K. C. Price, S. Nahar, C. Grezes, Q. Hu, P. Khalili Amiri, K. L. Wang, P. M. Voyles, and W. G. Wang, "Perpendicular magnetic tunnel junction with W seed and capping layers", J. Appl. Phys. **121**, 153902 (2017).

[47] K. Watanabe, S. Fukami, H. Sato, S. Ikeda, F. Matsukura, and H. Ohno, "Annealing temperature dependence of magnetic properties of CoFeB/MgO stacks on different buffer layers", Jpn. J. Appl. Phys. **56**, 0802B2 (2017).

[48] T. Liu, Y. Zhang, J. W. Cai, and H. Y. Pan, "Thermally robust Mo/CoFeB/MgO trilayers with strong perpendicular magnetic anisotropy", Sci. Rep. **4**, 5895 (2014).

[49] H. Almasi, D. R. Hickey, T. Newhouse-Illige, M. Xu, M. R. Rosales, S. Nahar, J. T. Held, K. A. Mkhoyan, and W. G. Wang, "Enhanced tunneling magnetoresistance and perpendicular magnetic anisotropy in Mo/CoFeB/MgO magnetic tunnel junctions", Appl. Phys. Lett. **106**, 182406 (2015).

[50] H. Almasi, M. Xu, Y. Xu, T. Newhouse-Illige, and W. G. Wang, "Effect of Mo insertion layers on the magnetoresistance and perpendicular magnetic anisotropy in Ta/CoFeB/MgO junctions", Appl. Phys. Lett. **109**, 032401 (2016).

[51] S.-E. Lee, Y. Takemura, and J.-G. Park, "Effect of double MgO tunneling barrier on thermal stability and TMR ratio for perpendicular MTJ spin-valve with tungsten layers", Appl. Phys. Lett. **109**, 182405 (2016).

[52] M. Wang, W. Cai, K. Cao, J. Zhou, J. Wrona, S. Peng, H. Yang, J. Wei, W. Kang, Y. Zhang, J. Langer, B. Ocker, A. Fert, and W. Zhao, "Current-induced magnetization switching in atom-thick tungsten engineered perpendicular magnetic tunnel junctions with large tunnel magnetoresistance", Nat. Commun. **9**, 671 (2018).

[53] M.-Y. Li, S.-K. Su, H.-S. P. Wong, and L.-J. Li, "How 2D semiconductors could extend Moore's law", Nature **567**, 169 (2019).

[54] Y. Liu, Y. Huang, and X. Duan, "Van der Waals integration before and beyond two-dimensional materials", Nature **567**, 323 (2019).

[55] X. Lin, W. Yang, K. L. Wang, and W. Zhao, "Two-dimensional spintronics for low-power electronics", Nat. Electron. **2**, 274–283 (2019).

[56] C. Gong, L. Li, Z. Li, H. Ji, A. Stern, Y. Xia, T. Cao, W. Bao, C. Wang, Y. Wang, Z. Q. Qiu, R. J. Cava, S. G. Louie, J. Xia, and X. Zhang, "Discovery of intrinsic ferromagnetism in two-dimensional van der Waals crystals", Nature **546**, 265 (2017).

[57] B. Huang, G. Clark, E. Navarro-Moratalla, D. R. Klein, R. Cheng, K. L. Seyler, D. Zhong, E. Schmidgall, M. A. McGuire, D. H. Cobden, W. Yao, D. Xiao, P. Jarillo-Herrero, and X. Xu, "Layer-dependent ferromagnetism in a van der Waals crystal down to the monolayer limit", Nature **546**, 270 (2017).

[58] Y. Deng, Y. Yu, Y. Song, J. Zhang, N. Z. Wang, Z. Sun, Y. Yi, Y. Z. Wu, S. Wu, J. Zhu, J. Wang, X. H. Chen, and Y. Zhang, "Gate-tunable room-temperature ferromagnetism in two-dimensional Fe_3GeTe_2", Nature **563**, 94 (2018).

[59] M. Bonilla, S. Kolekar, Y. Ma, H. C. Diaz, V. Kalappattil, R. Das, T. Eggers, H. R. Gutierrez, M.-H. Phan, and M. Batzill, "Strong room-temperature ferromagnetism in VSe_2 monolayers on van der Waals substrates", Nat. Nanotechnol. **13**, 289 (2018).

[60] C. Cardoso, D. Soriano, N. A. García-Martínez, and J. Fernández-Rossier, "Van der Waals spin valves", Phys. Rev. Lett. **121**, 067701 (2018).

[61] H. H. Kim, B. Yang, T. Patel, F. Sfigakis, C. Li, S. Tian, H. Lei, and A. W. Tsen, "One million percent tunnel magnetoresistance in a magnetic van der Waals heterostructure", Nano Lett. **18**, 4885–4890 (2018).

[62] T. Song, M. W.-Y. Tu, C. Carnahan, X. Cai, T. Taniguchi, K. Watanabe, M. A. McGuire, D. H. Cobden, D. Xiao, W. Yao, and X. Xu, "Voltage control of a van der Waals spin-filter magnetic tunnel junction", Nano Lett. **19**, 915–920 (2019).

[63] D. R. Klein, D. MacNeill, J. L. Lado, D. Soriano, E. Navarro-Moratalla, K. Watanabe, T. Taniguchi, S. Manni, P. Canfield, J. Fernández-Rossier, and P. Jarillo-Herrero, "Probing magnetism in 2D van der Waals crystalline insulators via electron tunneling", Science **360**, 1218–1222 (2018).

[64] Z. Wang, D. Sapkota, T. Taniguchi, K. Watanabe, D. Mandrus, and A. F. Morpurgo, "Tunneling spin valves based on Fe_3GeTe_2/hBN/Fe_3GeTe_2 van der Waals heterostructures", Nano Lett. **18**, 4303–4308 (2018).

[65] T. Song, X. Cai, M. W.-Y. Tu, X. Zhang, B. Huang, N. P. Wilson, K. L. Seyler, L. Zhu, T. Taniguchi, K. Watanabe, M. A. McGuire, D. H. Cobden, D. Xiao, W. Yao, and X. Xu, "Giant tunneling magnetoresistance in spin-filter van der Waals heterostructures", Science **360**, 1214–1218 (2018).

[66] W. S. Zhao, Y. Zhang, T. Devolder, J. O. Klein, D. Ravelosona, C. Chappert, and P. Mazoyer, "Failure and reliability analysis of STT-MRAM", Microelectron. Reliab. **52**, 1848–1852 (2012).

[67] W. Zhao, X. Zhao, B. Zhang, K. Cao, L. Wang, W. Kang, Q. Shi, M. Wang, Y. Zhang, Y. Wang, S. Peng, J.-O. Klein, L. A. De Barros Naviner, and D. Ravelosona, "Failure analysis in magnetic tunnel junction nanopillar with interfacial perpendicular magnetic anisotropy", Materials **9**, 41 (2016).

[68] M. Krounbi, V. Nikitin, D. Apalkov, J. Lee, X. Tang, R. Beach, D. Erickson, and E. Chen, "Status and challenges in spin-transfer torque MRAM technology", ECS Trans. **69**, 119–126 (2015).

[69] G. Prenat, K. Jabeur, G. Di Pendina, O. Boulle, and G. Gaudin, "Beyond STT-MRAM, spin orbit torque RAM SOT-MRAM for high speed and high reliability applications", SpringerLink, 145–157 (2015).

[70] I. M. Miron, K. Garello, G. Gaudin, P.-J. Zermatten, M. V. Costache, S. Auffret, S. Bandiera, B. Rodmacq, A. Schuhl, and P. Gambardella, "Perpendicular switching of a single ferromagnetic layer induced by in-plane current injection", Nature **476**, 189–193 (2011).

[71] L. Liu, C.-F. Pai, Y. Li, H. W. Tseng, D. C. Ralph, and R. A. Buhrman, "Spin-torque switching with the giant spin Hall effect of tantalum", Science **336**, 555–558 (2012).

[72] M. Cubukcu, O. Boulle, M. Drouard, K. Garello, C. Onur Avci, I. Mihai Miron, J. Langer, B. Ocker, P. Gambardella, and G. Gaudin, "Spin-orbit torque magnetization switching of a three-terminal perpendicular magnetic tunnel junction", Appl. Phys. Lett. **104**, 042406 (2014).

[73] J. Kim, B. Tuohy, C. Ma, W. H. Choi, I. Ahmed, D. Lilja, and C. H. Kim, "Spin-Hall effect MRAM based cache memory: A feasibility study", in 2015 73rd Annual Device Research Conference (DRC) (June 2015), pp. 117–118.

[74] A. van den Brink, S. Cosemans, S. Cornelissen, M. Manfrini, A. Vaysset, W. Van Roy, T. Min, H. J. M. Swagten, and B. Koopmans, "Spin-Hall-assisted magnetic random access memory", Appl. Phys. Lett. **104**, 012403 (2014).

[75] C. K. Safeer, E. Jué, A. Lopez, L. Buda-Prejbeanu, S. Auffret, S. Pizzini, O. Boulle, I. M. Miron, and G. Gaudin, "Spin–orbit torque magnetization switching controlled by geometry", Nat. Nanotechnol. **11**, 143–146 (2015).

[76] M. Cubukcu, O. Boulle, N. Mikuszeit, C. Hamelin, T. Brächer, N. Lamard, M. Cyrille, L. Buda-Prejbeanu, K. Garello, I. M. Miron, O. Klein, G. de Loubens, V. V. Naletov, J. Langer, B. Ocker, P. Gambardella, and G. Gaudin, "Ultra-fast perpendicular spin-orbit torque MRAM", IEEE Trans. Magn. **54**, 1–4 (2018).

[77] L. Liu, T. Moriyama, D. C. Ralph, and R. A. Buhrman, "Spin-torque ferromagnetic resonance induced by the spin Hall effect", Phys. Rev. Lett. **106**, 036601 (2011).

[78] C.-F. Pai, M.-H. Nguyen, C. Belvin, L. H. Vilela-Leão, D. C. Ralph, and R. A. Buhrman, "Enhancement of perpendicular magnetic anisotropy and transmission of spin-Hall-effect-induced spin currents by a Hf spacer layer in W/Hf/CoFeB /MgO layer structures", Appl. Phys. Lett. **104**, 082407 (2014).

[79] J. Sinova and T. Jungwirth, "Surprises from the spin Hall effect", Phys. Today **70**, 38 (2017).

[80] N. Nagaosa, J. Sinova, S. Onoda, A. H. MacDonald, and N. P. Ong, "Anomalous Hall effect", Rev. Mod. Phys. **82**, 1539–1592 (2010).

[81] J. Qiao, J. Zhou, Z. Yuan, and W. Zhao, "Calculation of intrinsic spin Hall conductivity by Wannier interpolation", Phys. Rev. B **98**, 214402 (2018).

[82] F. Freimuth, S. Blügel, and Y. Mokrousov, "Anisotropic spin Hall effect from first principles", Phys. Rev. Lett. **105**, 246602 (2010).

[83] A. Manchon, J. Železný, I. Miron, T. Jungwirth, J. Sinova, A. Thiaville, K. Garello, and P. Gambardella, "Current-induced spin-orbit torques in ferromagnetic and antiferromagnetic systems", Rev. Mod. Phys. **91**, 035004 (2019).

[84] A. Manchon and S. Zhang, "Theory of spin torque due to spin-orbit coupling", Phys. Rev. B **79**, 094422 (2009).

[85] G. Yu, P. Upadhyaya, Y. Fan, J. G. Alzate, W. Jiang, K. L. Wong, S. Takei, S. A. Bender, L.-T. Chang, Y. Jiang, M. Lang, J. Tang, Y. Wang, Y. Tserkovnyak, P. K. Amiri, and K. L. Wang, "Switching of perpendicular magnetization by spin-orbit torques in the absence of external magnetic fields", Nat. Nanotechnol. **9**, 548 (2014).

[86] C.-F. Pai, L. Liu, Y. Li, H. W. Tseng, D. C. Ralph, and R. A. Buhrman, "Spin transfer torque devices utilizing the giant spin Hall effect of tungsten", Appl. Phys. Lett. **101**, 122404 (2012).

[87] W. Zhang, M. B. Jungfleisch, W. Jiang, J. Sklenar, F. Y. Fradin, J. E. Pearson, J. B. Ketterson, and A. Hoffmann, "Spin pumping and inverse spin Hall effects—Insights for future spin-orbitronics (invited)", J. Appl. Phys. **117**, 172610 (2015).

[88] M. Cinchetti, K. Heimer, J.-P. Wüstenberg, O. Andreyev, M. Bauer, S. Lach, C. Ziegler, Y. Gao, and M. Aeschlimann, "Determination of spin injection and transport in a ferromagnet/organic semiconductor heterojunction by two-photon photoemission", Nat. Mater. **8**, 115–119 (2008).

[89] B. T. Jonker, G. Kioseoglou, A. T. Hanbicki, C. H. Li, and P. E. Thompson, "Electrical spin-injection into silicon from a ferromagnetic metal/tunnel barrier contact", Nat. Phys. **3**, 542–546 (2007).

[90] Q. Wu, L. Shen, Z. Bai, M. Zeng, M. Yang, Z. Huang, and Y. P. Feng, "Efficient spin injection into graphene through a tunnel barrier: Overcoming the spin-conductance mismatch", Phys. Rev. Appl. **2**, 044008 (2014).

[91] T. Yamaguchi, R. Moriya, S. Oki, S. Yamada, S. Masubuchi, K. Hamaya, and T. Machida, "Spin injection into multilayer graphene from highly spin-polarized Co_2FeSi Heusler alloy", Appl. Phys Express **9**, 063006 (2016).

[92] S. Omar and B. J. van Wees, "Graphene-WS_2 heterostructures for tunable spin injection and spin transport", Phys. Rev. B **95**, 081404 (2017).

[93] V. M. Karpan, G. Giovannetti, P. A. Khomyakov, M. Talanana, A. A. Starikov, M. Zwierzycki, J. van den Brink, G. Brocks, and P. J. Kelly, "Graphite and graphene as perfect spin filters", Phys. Rev. Lett. **99**, 176602 (2007).

[94] J. Maassen, W. Ji, and H. Guo, "Graphene spintronics: The role of ferromagnetic electrodes", Nano Lett. **11**, 151–155 (2011).

[95] P. Lazić, G. M. Sipahi, R. K. Kawakami, and I. Žutić, "Graphene spintronics: Spin injection and proximity effects from first principles", Phys. Rev. B **90**, 085429 (2014).

[96] B. Dlubak, P. Seneor, A. Anane, C. Barraud, C. Deranlot, D. Deneuve, B. Servet, R. Mattana, F. Petroff, and A. Fert, "Are Al_2O_3 and MgO tunnel barriers suitable for spin injection in graphene?", Appl. Phys. Lett. **97**, 092502 (2010).

[97] M. V. Kamalakar, A. Dankert, J. Bergsten, T. Ive, and S. P. Dash, "Enhanced tunnel spin injection into graphene using chemical vapor deposited hexagonal boron nitride", Sci. Rep. **4**, 6146 (2014).

[98] B. Dlubak, M.-B. Martin, C. Deranlot, B. Servet, S. Xavier, R. Mattana, M. Sprinkle, C. Berger, W. A. De Heer, F. Petroff, A. Anane, P. Seneor, and A. Fert, "Highly efficient spin transport in epitaxial graphene on SiC", Nat. Phys. **8**, 557 (2012).

[99] X. Lin, L. Su, Z. Si, Y. Zhang, A. Bournel, Y. Zhang, J.-O. Klein, A. Fert, and W. Zhao, "Gate-driven pure spin current in graphene", Phys. Rev. Appl. **8**, 034006 (2017).

[100] F. Schwierz, "Graphene transistors", Nat. Nanotechnol. **5**, 487–496 (2010).

[101] M. Born and R. Oppenheimer, "Zur Quantentheorie der Molekeln", Ann. Phys. **389**, 457–484 (1927).

[102] D. R. Hartree, "The wave mechanics of an atom with a non-coulomb central field. part I. theory and methods", Math. Proc. Cambridge Philos. Soc. **24**, 89–110 (1928).

[103] J. C. Slater, "Note on Hartree's method", Phys. Rev. **35**, 210–211 (1930).

[104] L. H. Thomas, "The calculation of atomic fields", Proc. Camb. Phil. Soc. **23** (1927).

[105] E. Fermi, "Un metodo statistico per la determinazione di alcune priorieta dell'atome", Rend. Accad. Naz. Lincei **6** (1927).

[106] P. Hohenberg and W. Kohn, "Inhomogeneous electron gas", Phys. Rev. **136**, B864–B871 (1964).

[107] W. Kohn and L. J. Sham, "Self-consistent equations including exchange and correlation effects", Phys. Rev. **140**, A1133–A1138 (1965).

[108] D. M. Ceperley and B. J. Alder, "Ground state of the electron gas by a stochastic method", Phys. Rev. Lett. **45**, 566–569 (1980).

[109] J. P. Perdew, K. Burke, and M. Ernzerhof, "Generalized gradient approximation made simple", Phys. Rev. Lett. **77**, 3865–3868 (1996).

[110] M. Wang, W. Cai, D. Zhu, Z. Wang, J. Kan, Z. Zhao, K. Cao, Z. Wang, Y. Zhang, T. Zhang, C. Park, J.-P. Wang, A. Fert, and W. Zhao, "Field-free switching of a perpendicular magnetic tunnel junction through the interplay of spin–orbit and spin-transfer torques", Nat. Electron. **1**, 582 (2018).

[111] T. A. Peterson, A. P. McFadden, C. J. Palmstrøm, and P. A. Crowell, "Influence of the magnetic proximity effect on spin-orbit torque efficiencies in ferromagnet/platinum bilayers", Phys. Rev. B **97**, 020403 (2018).

[112] K. Sankaran, J. Swerts, S. Couet, K. Stokbro, and G. Pourtois, "Oscillatory behavior of the tunnel magnetoresistance due to thickness variations in Ta|CoFe|MgO magnetic tunnel junctions: A first-principles study", Phys. Rev. B **94**, 094424 (2016).

[113] Y. Liu, B. Zhou, and J.-G. Zhu, "Field-free magnetization switching by utilizing the spin Hall effect and interlayer exchange coupling of iridium", Sci. Rep. **9**, 325 (2019).

[114] L. Liu, C.-F. Pai, D. C. Ralph, and R. A. Buhrman, "Magnetic oscillations driven by the spin Hall effect in 3-terminal magnetic tunnel junction devices", Phys. Rev. Lett. **109**, 186602 (2012).

[115] K.-S. Lee, S.-W. Lee, B.-C. Min, and K.-J. Lee, "Threshold current for switching of a perpendicular magnetic layer induced by spin Hall effect", Appl. Phys. Lett. **102**, 112410 (2013).

[116] J. Häglund, A. Fernández Guillermet, G. Grimvall, and M. Körling, "Theory of bonding in transition-metal carbides and nitrides", Phys. Rev. B **48**, 11685–11691 (1993).

[117] S. Peng, W. Zhao, J. Qiao, L. Su, J. Zhou, H. Yang, Q. Zhang, Y. Zhang, C. Grezes, P. K. Amiri, and K. L. Wang, "Giant interfacial perpendicular magnetic anisotropy in MgO/CoFe/capping layer structures", Appl. Phys. Lett. **110**, 072403 (2017).

[118] S. Peng, M. Wang, H. Yang, L. Zeng, J. Nan, J. Zhou, Y. Zhang, A. Hallal, M. Chshiev, K. L. Wang, Q. Zhang, and W. Zhao, "Origin of interfacial perpendicular magnetic anisotropy in MgO/CoFe/metallic capping layer structures", Sci. Rep. **5**, 18173 (2015).

[119] G. Kresse and J. Hafner, "Ab initio molecular dynamics for open-shell transition metals", Phys. Rev. B **48**, 13115–13118 (1993).

[120] G. Kresse and J. Furthmüller, "Efficient iterative schemes for ab initio total-energy calculations using a plane-wave basis set", Phys. Rev. B **54**, 11169–11186 (1996).

[121] G. Kresse and D. Joubert, "From ultrasoft pseudopotentials to the projector augmented-wave method", Phys. Rev. B **59**, 1758–1775 (1999).

[122] J. Taylor, H. Guo, and J. Wang, "Ab initio modeling of quantum transport properties of molecular electronic devices", Phys. Rev. B **63**, 245407 (2001).

[123] J. Taylor, H. Guo, and J. Wang, "Ab initio modeling of open systems: Charge transfer, electron conduction, and molecular switching of a C_{60} device", Phys. Rev. B **63**, 121104 (2001).

[124] P. Giannozzi, O. Andreussi, T. Brumme, O. Bunau, M. B. Nardelli, M. Calandra, R. Car, C. Cavazzoni, D. Ceresoli, M. Cococcioni, N. Colonna, I. Carnimeo, A. Dal Corso, S. de Gironcoli, P. Delugas, R. A. DiStasio Jr., A. Ferretti, A. Floris, G. Fratesi, G. Fugallo, R. Gebauer, U. Gerstmann, F. Giustino, T. Gorni, J. Jia, M. Kawamura, H.-Y. Ko, A. Kokalj, E. Küçükbenli, M. Lazzeri, M. Marsili, N. Marzari, F. Mauri, N. L. Nguyen, H.-V. Nguyen, A. Otero-de-la-Roza, L. Paulatto, S. Poncé, D. Rocca, R. Sabatini, B. Santra, M. Schlipf, A. P. Seitsonen, A. Smogunov, I. Timrov, T. Thonhauser, P. Umari, N. Vast, X. Wu, and S. Baroni, "Advanced capabilities for materials modelling with Quantum ESPRESSO", J. Phys.: Condens. Matter **29**, 465901 (2017).

[125] G. Pizzi, V. Vitale, R. Arita, S. Blügel, F. Freimuth, G. Géranton, M. Gibertini, D. Gresch, C. Johnson, T. Koretsune, J. Ibañez-Azpiroz, H. Lee, J.-M. Lihm, D. Marchand, A. Marrazzo, Y. Mokrousov, J. I. Mustafa, Y. Nohara, Y. Nomura, L. Paulatto, S. Poncé, T. Ponweiser, J. Qiao, F. Thöle, S. S. Tsirkin, M. Wierzbowska, N. Marzari, D. Vanderbilt, I. Souza, A. A. Mostofi, and J. R. Yates, "Wannier90 as a community code: new features and applications", arXiv (2019).

[126] N. Marzari, A. A. Mostofi, J. R. Yates, I. Souza, and D. Vanderbilt, "Maximally localized wannier functions: Theory and applications", Rev. Mod. Phys. **84**, 1419–1475 (2012).

[127] N. Miyakawa, D. C. Worledge, and K. Kita, "Impact of Ta diffusion on the perpendicular magnetic anisotropy of Ta/CoFeB/MgO", IEEE Magn. Lett. **4**, 1000104 (2013).

[128] J. Chatterjee, R. C. Sousa, N. Perrissin, S. Auffret, C. Ducruet, and B. Dieny, "Enhanced annealing stability and perpendicular magnetic anisotropy in perpendicular magnetic tunnel junctions using W layer", Appl. Phys. Lett. **110**, 202401 (2017).

[129] K. Watanabe, S. Fukami, H. Sato, F. Matsukura, and H. Ohno, "Magnetic properties of CoFeB–MgO stacks with different buffer-layer materials (Ta or Mo)", IEEE Trans. Magn. **52**, 1–4 (2016).

[130] O. Wunnicke, N. Papanikolaou, R. Zeller, P. H. Dederichs, V. Drchal, and J. Kudrnovský, "Effects of resonant interface states on tunneling magnetoresistance", Phys. Rev. B **65**, 064425 (2002).

[131] P. X. Xu, V. M. Karpan, K. Xia, M. Zwierzycki, I. Marushchenko, and P. J. Kelly, "Influence of roughness and disorder on tunneling magnetoresistance", Phys. Rev. B **73**, 180402 (2006).

[132] X. Sui, C. Wang, J. Kim, J. Wang, S. H. Rhim, W. Duan, and N. Kioussis, "Giant enhancement of the intrinsic spin Hall conductivity in β-tungsten via substitutional doping", Phys. Rev. B **96**, 241105 (2017).

[133] Y. Yao, L. Kleinman, A. H. MacDonald, J. Sinova, T. Jungwirth, D.-S. Wang, E. Wang, and Q. Niu, "First principles calculation of anomalous Hall conductivity in ferromagnetic bcc Fe", Phys. Rev. Lett. **92**, 037204 (2004).

[134] G. Y. Guo, Y. Yao, and Q. Niu, "Ab initio calculation of the intrinsic spin Hall effect in semiconductors", Phys. Rev. Lett. **94**, 226601 (2005).

[135] G. Y. Guo, S. Murakami, T. W. Chen, and N. Nagaosa, "Intrinsic spin Hall effect in platinum: First-principles calculations", Phys. Rev. Lett. **100**, 096401 (2008).

[136] M. Obstbaum, M. Decker, A. K. Greitner, M. Haertinger, T. N. G. Meier, M. Kronseder, K. Chadova, S. Wimmer, D. Ködderitzsch, H. Ebert, and C. H. Back, "Tuning spin Hall angles by alloying", Phys. Rev. Lett. **117**, 167204 (2016).

[137] S. Lee, J. Kim, Y. C. Park, and S.-H. Chun, "Atomistic real-space observation of the van der Waals layered structure and tailored morphology in VSe_2", Nanoscale **11**, 431–436 (2019).

[138] H. Zeng, J. Dai, W. Yao, D. Xiao, and X. Cui, "Valley polarization in MoS_2 monolayers by optical pumping", Nat. Nanotechnol. **7**, 490 (2012).

[139] B. Shabbir, M. Nadeem, Z. Dai, M. S. Fuhrer, Q.-K. Xue, X. Wang, and Q. Bao, "Long range intrinsic ferromagnetism in two dimensional materials and dissipationless future technologies", Appl. Phys. Rev. **5**, 041105 (2018).

[140] W.-Y. Tong, S.-J. Gong, X. Wan, and C.-G. Duan, "Concepts of ferrovalley material and anomalous valley Hall effect", Nat. Commun. **7**, 13612 (2016).

[141] S. L. Dudarev, G. A. Botton, S. Y. Savrasov, C. J. Humphreys, and A. P. Sutton, "Electron-energy-loss spectra and the structural stability of nickel oxide: An LSDA+U study", Phys. Rev. B **57**, 1505–1509 (1998).

[142] M. Esters, R. G. Hennig, and D. C. Johnson, "Dynamic instabilities in strongly correlated VSe_2 monolayers and bilayers", Phys. Rev. B **96**, 235147 (2017).

[143] T. Ozaki, "Variationally optimized atomic orbitals for large-scale electronic structures", Phys. Rev. B **67**, 155108 (2003).

[144] T. Ozaki and H. Kino, "Numerical atomic basis orbitals from H to Kr", Phys. Rev. B **69**, 195113 (2004).

[145] T. Ozaki and H. Kino, "Efficient projector expansion for the ab initio LCAO method", Phys. Rev. B **72**, 045121 (2005).

[146] M. Koleini, M. Paulsson, and M. Brandbyge, "Efficient organometallic spin filter between single-wall carbon nanotube or graphene electrodes", Phys. Rev. Lett. **98**, 197202 (2007).

[147] Y. Ma, Y. Dai, M. Guo, C. Niu, Y. Zhu, and B. Huang, "Evidence of the existence of magnetism in pristine VX_2 monolayers (X = S, Se) and their strain-induced tunable magnetic properties", ACS Nano **6**, 1695–1701 (2012).

[148] M. Alghamdi, M. Lohmann, J. Li, P. R. Jothi, Q. Shao, M. Aldosary, T. Su, B. P. T. Fokwa, and J. Shi, "Highly efficient spin–orbit torque and switching of layered ferromagnet Fe_3GeTe_2", Nano Lett. **19**, 4400–4405 (2019).

[149] X. Wang, J. Tang, X. Xia, C. He, J. Zhang, Y. Liu, C. Wan, C. Fang, C. Guo, W. Yang, Y. Guang, X. Zhang, H. Xu, J. Wei, M. Liao, X. Lu, J. Feng, X. Li, Y. Peng, H. Wei, R. Yang, D. Shi, X. Zhang, Z. Han, Z. Zhang, G. Zhang, G. Yu, and X. Han, "Current-driven magnetization switching in a van der Waals ferromagnet Fe_3GeTe_2 ", Sci. Adv. **5**, eaaw8904 (2019).

[150] D. MacNeill, G. M. Stiehl, M. H. D. Guimaraes, R. A. Buhrman, J. Park, and D. C. Ralph, "Control of spin–orbit torques through crystal symmetry in WTe_2/ferromagnet bilayers", Nat. Phys. **13**, 300 (2016).

[151] D. MacNeill, G. M. Stiehl, M. H. D. Guimarães, N. D. Reynolds, R. A. Buhrman, and D. C. Ralph, "Thickness dependence of spin-orbit torques generated by WTe_2", Phys. Rev. B **96**, 054450 (2017).

[152] P. Li, W. Wu, Y. Wen, C. Zhang, J. Zhang, S. Zhang, Z. Yu, S. A. Yang, A. Manchon, and X.-X. Zhang, "Spin-momentum locking and spin-orbit torques in magnetic nano-heterojunctions composed of Weyl semimetal WTe_2", Nat. Commun. **9**, 3990 (2018).

[153] A. A. Soluyanov, D. Gresch, Z. Wang, Q. Wu, M. Troyer, X. Dai, and B. A. Bernevig, "Type-II Weyl semimetals", Nature **527**, 495 (2015).

[154] Y. Wu, D. Mou, N. H. Jo, K. Sun, L. Huang, S. L. Bud'ko, P. C. Canfield, and A. Kaminski, "Observation of Fermi arcs in the type-II Weyl semimetal candidate WTe_2", Phys. Rev. B **94**, 121113 (2016).

[155] C. Wang, Y. Zhang, J. Huang, S. Nie, G. Liu, A. Liang, Y. Zhang, B. Shen, J. Liu, C. Hu, Y. Ding, D. Liu, Y. Hu, S. He, L. Zhao, L. Yu, J. Hu, J. Wei, Z. Mao, Y. Shi, X. Jia, F. Zhang, S. Zhang, F. Yang, Z. Wang, Q. Peng, H. Weng, X. Dai, Z. Fang, Z. Xu, C. Chen, and X. J. Zhou, "Observation of Fermi arc and its connection with bulk states in the candidate type-II Weyl semimetal WTe_2", Phys. Rev. B **94**, 241119 (2016).

[156] B. Feng, Y.-H. Chan, Y. Feng, R.-Y. Liu, M.-Y. Chou, K. Kuroda, K. Yaji, A. Harasawa, P. Moras, A. Barinov, W. Malaeb, C. Bareille, T. Kondo, S. Shin, F. Komori, T.-C. Chiang, Y. Shi, and I. Matsuda, "Spin texture in type-II Weyl semimetal WTe_2", Phys. Rev. B **94**, 195134 (2016).

[157] M. Seemann, D. Ködderitzsch, S. Wimmer, and H. Ebert, "Symmetry-imposed shape of linear response tensors", Phys. Rev. B **92**, 155138 (2015).

[158] Z. Wang, D. Gresch, A. A. Soluyanov, W. Xie, S. Kushwaha, X. Dai, M. Troyer, R. J. Cava, and B. A. Bernevig, "$MoTe_2$: A type-II Weyl topological metal", Phys. Rev. Lett. **117**, 056805 (2016).

[159] Y. Sun, Y. Zhang, C. Felser, and B. Yan, "Strong intrinsic spin Hall effect in the TaAs family of Weyl semimetals", Phys. Rev. Lett. **117**, 146403 (2016).

[160] G. Y. Guo, "Ab initio calculation of intrinsic spin Hall conductivity of Pd and Au", J. Appl. Phys. **105**, 07C701 (2009).

[161] Y. Zhang, Y. Sun, H. Yang, J. Železný, S. P. P. Parkin, C. Felser, and B. Yan, "Strong anisotropic anomalous Hall effect and spin Hall effect in the chiral antiferromagnetic compounds Mn_3X (X = Ge, Sn, Ga, Ir, Rh, and Pt)", Phys. Rev. B **95**, 075128 (2017).

[162] T. Tanaka, H. Kontani, M. Naito, T. Naito, D. S. Hirashima, K. Yamada, and J. Inoue, "Intrinsic spin Hall effect and orbital Hall effect in 4*d* and 5*d* transition metals", Phys. Rev. B **77**, 165117 (2008).

[163] B. Zhao, D. Khokhriakov, Y. Zhang, H. Fu, B. Karpiak, A. Hoque, X. Xu, Y. Jiang, B. Yan, and S. P. Dash, "Observation of spin Hall effect in semimetal WTe_2", arXiv (2018).

[164] Y. Qi, P. G. Naumov, M. N. Ali, C. R. Rajamathi, W. Schnelle, O. Barkalov, M. Hanfland, S.-C. Wu, C. Shekhar, Y. Sun, V. Süß, M. Schmidt, U. Schwarz, E. Pippel, P. Werner, R. Hillebrand, T. Förster, E. Kampert, S. Parkin, R. J. Cava, C. Felser, B. Yan, and S. A. Medvedev, "Superconductivity in Weyl semimetal candidate $MoTe_2$", Nat. Commun. **7**, 11038 (2016).

[165] M. K. Jana, A. Singh, D. J. Late, C. R. Rajamathi, K. Biswas, C. Felser, U. V. Waghmare, and C. N. R. Rao, "A combined experimental and theoretical study of the structural, electronic and vibrational", J. Phys.: Condens. Matter **27**, 285401 (2015).

[166] Y. Wang, P. Deorani, X. Qiu, J. H. Kwon, and H. Yang, "Determination of intrinsic spin Hall angle in Pt", Appl. Phys. Lett. **105**, 152412 (2014).

[167] W. Zhang, W. Han, X. Jiang, S.-H. Yang, and S. S. P. Parkin, "Role of transparency of platinum–ferromagnet interfaces in determining the intrinsic magnitude of the spin Hall effect", Nat. Phys. **11**, 496 (2015).

[168] A. A. Tedstone, D. J. Lewis, and P. O'Brien, "Synthesis, properties, and applications of transition metal-doped layered transition metal dichalcogenides", Chem. Mater. **28**, 1965–1974 (2016).

[169] W. Han, R. K. Kawakami, M. Gmitra, and J. Fabian, "Graphene spintronics", Nat. Nanotechnol. **9**, 794 (2014).

[170] L. Su, W. Zhao, Y. Zhang, D. Querlioz, Y. Zhang, J.-O. Klein, P. Dollfus, and A. Bournel, "Proposal for a graphene-based all-spin logic gate", Appl. Phys. Lett. **106**, 072407 (2015).

[171] M. Zeng, L. Shen, H. Su, C. Zhang, and Y. Feng, "Graphene-based spin logic gates", Appl. Phys. Lett. **98**, 092110 (2011).

[172] P. Vogt, P. De Padova, C. Quaresima, J. Avila, E. Frantzeskakis, M. C. Asensio, A. Resta, B. Ealet, and G. Le Lay, "Silicene: Compelling experimental evidence for graphene-like two-dimensional silicon", Phys. Rev. Lett. **108**, 155501 (2012).

[173] L. Meng, Y. Wang, L. Zhang, S. Du, R. Wu, L. Li, Y. Zhang, G. Li, H. Zhou, W. A. Hofer, and H.-J. Gao, "Buckled silicene formation on Ir(111)", Nano Lett. **13**, 685–690 (2013).

[174] S. Cahangirov, M. Topsakal, E. Aktürk, H. Şahin, and S. Ciraci, "Two- and one-dimensional honeycomb structures of silicon and germanium", Phys. Rev. Lett. **102**, 236804 (2009).

[175] A. Molle, C. Grazianetti, L. Tao, D. Taneja, M. H. Alam, and D. Akinwande, "Silicene, silicene derivatives, and their device applications", Chem. Soc. Rev. **47**, 6370–6387 (2018).

[176] J. Zhao, H. Liu, Z. Yu, R. Quhe, S. Zhou, Y. Wang, C. C. Liu, H. Zhong, N. Han, J. Lu, Y. Yao, and K. Wu, "Rise of silicene: A competitive 2D material", Prog. Mater Sci. **83**, 24–151 (2016).

[177] Z. Ni, Q. Liu, K. Tang, J. Zheng, J. Zhou, R. Qin, Z. Gao, D. Yu, and J. Lu, "Tunable bandgap in silicene and germanene", Nano Lett. **12**, 113–118 (2012).

[178] N. D. Drummond, V. Zólyomi, and V. I. Fal'ko, "Electrically tunable band gap in silicene", Phys. Rev. B **85**, 075423 (2012).

[179] L. Tao, E. Cinquanta, D. Chiappe, C. Grazianetti, M. Fanciulli, M. Dubey, A. Molle, and D. Akinwande, "Silicene field-effect transistors operating at room temperature", Nat. Nanotechnol. **10**, 227 (2015).

[180] C.-C. Liu, W. Feng, and Y. Yao, "Quantum spin Hall effect in silicene and two-dimensional germanium", Phys. Rev. Lett. **107**, 076802 (2011).

[181] A. Molle, C. Grazianetti, D. Chiappe, E. Cinquanta, E. Cianci, G. Tallarida, and M. Fanciulli, "Hindering the oxidation of silicene with non-reactive encapsulation", Adv. Funct. Mater. **23**, 4340–4344 (2013).

Publications related to this work

[1] **J. Zhou**, W. Zhao, Y. Wang, S. Peng, J. Qiao, L. Su, L. Zeng, N. Lei, L. Liu, Y. Zhang, and A. Bournel, "Large influence of capping layers on tunnel magnetoresistance in magnetic tunnel junctions", Appl. Phys. Lett. **109**, 242403 (2016).

[2] **J. Zhou**, H. Zhou, A. Bournel, and W. Zhao, "Large spin Hall effect and tunneling magnetoresistance in iridium-based magnetic tunnel junctions", Sci. China Phys. Mech. Astron. **63**, 217511 (2020).

[3] **J. Zhou**, W. Zhao, S. Peng, J. Qiao, J.-O. Klein, X. Lin, Y. Zhang, and A. Bournel, "High tunnel magnetoresistance in Mo/CoFe/MgO magnetic tunnel junction: A first-principles study", IEEE Trans. Magn. **53**, 1–4 (2017).

[4] **J. Zhou**, J. Qiao, C.-G. Duan, A. Bournel, K. L. Wang, and W. Zhao, "Large tunneling magnetoresistance in VSe_2/MoS_2 magnetic tunnel junction", ACS Appl. Mater. Interfaces **11**, 17647–17653 (2019).

[5] **J. Zhou**, J. Qiao, A. Bournel, and W. Zhao, "Intrinsic spin Hall conductivity of the semimetals $MoTe_2$ and WTe_2", Phys. Rev. B **99**, 060408 (2019).

[6] **J. Zhou**, A. Bournel, Y. Wang, X. Lin, Y. Zhang, and W. Zhao, "Silicene spintronics: Fe(111)/silicene system for efficient spin injection", Appl. Phys. Lett. **111**, 182408 (2017).

International conferences

[1] **J. Zhou**, J. Qiao, C.-G. Duan, A. Bournel, K. L. Wang, and W. Zhao, "Room-temperature tunneling magnetoresistance and spin Hall effect in van der Waals magnetic tunnel junction", in the 10$^{\text{th}}$ International Symposium on Metallic Multilayers (MML 2019), Oral (June 2019).

[2] **J. Zhou**, A. Bournel, Y. Wang, X. Lin, Y. Zhang, and W. Zhao, "Silicene spintronics: Fe(111)/silicene system for efficient spin injection", in Intermag 2018 Conference, Poster (Apr. 2018).

[3] **J. Zhou**, W. Zhao, S. Peng, J. Qiao, J.-O. Klein, X. Lin, Y. Zhang, and A. Bournel, "Heavy metal modulations for magnetic tunnel junction performances", in Journées Nationales du Réseau Doctoral en Micro-nanoélectronique (JNRDM), Oral+poster (Nov. 2017).

[4] **J. Zhou**, T. Sarkar, A. Chanda, A. P. Chen, and D. Kumar, "Investigation of the magnetic properties of 2D materials for spintronics applications", in IEEE magnetic society summer school 2017, Group presentation (June 2017).

[5] **J. Zhou**, W. Zhao, Y. Wang, S. Peng, J. Qiao, L. Su, L. Zeng, N. Lei, L. Liu, Y. Zhang, and A. Bournel, "Large influence of capping layers on tunnel magnetoresistance in magnetic tunnel junctions", in Intermag 2017 Conference, Poster (Apr. 2017).

Other publications

[1] S. Peng*, D. Zhu*, **J. Zhou***, B. Zhang, A. Cao, M. Wang, W. Cai, K. Cao, and W. Zhao, "Modulation of heavy metal/ferromagnetic metal interface for high-performance spintronic devices", Adv. Electron. Mater. **5**, 1900134 (2019).

[2] J. Qiao, **J. Zhou**, Z. Yuan, and W. Zhao, "Calculation of intrinsic spin Hall conductivity by Wannier interpolation", Phys. Rev. B **98**, 214402 (2018).

[3] M. Wang, W. Cai, K. Cao, **J. Zhou**, J. Wrona, S. Peng, H. Yang, J. Wei, W. Kang, Y. Zhang, J. Langer, B. Ocker, A. Fert, and W. Zhao, "Current-induced magnetization switching in atom-thick tungsten engineered perpendicular magnetic tunnel junctions with large tunnel magnetoresistance", Nat. Commun. **9**, 671 (2018).

[4] S. Peng, L. Wang, X. Li, Z. Wang, **J. Zhou**, J. Qiao, R. Chen, Y. Zhang, K. L. Wang, and W. Zhao, "Enhancement of perpendicular magnetic anisotropy through Fe insertion at the CoFe/W interface", IEEE Trans. Magn. **54**, 1–5 (2018).

[5] S. Peng, S. Li, W. Kang, **J. Zhou**, N. Lei, Y. Zhang, H. Yang, X. Li, P. K. Amiri, K. L. Wang, and W. Zhao, "Large voltage-controlled magnetic anisotropy in the $SrTiO_3$/Fe/Cu structure", Appl. Phys. Lett. **111**, 152403 (2017).

[6] S. Peng, W. Zhao, J. Qiao, L. Su, **J. Zhou**, H. Yang, Q. Zhang, Y. Zhang, C. Grezes, P. K. Amiri, and K. L. Wang, "Giant interfacial perpendicular mag-

netic anisotropy in MgO/CoFe/capping layer structures", Appl. Phys. Lett. **110**, 072403 (2017).

[7] S. Peng, M. Wang, H. Yang, L. Zeng, J. Nan, **J. Zhou**, Y. Zhang, A. Hallal, M. Chshiev, K. L. Wang, Q. Zhang, and W. Zhao, "Origin of interfacial perpendicular magnetic anisotropy in MgO/CoFe/metallic capping layer structures", Sci. Rep. **5**, 18173 (2015).

Acknowledgements

At the end of my Ph.D. period, I would like to express the most sincere gratitude to my supervisor, Prof. BOURNEL Arnaud, who gives me the chance to obtain the double doctoral degree between Université Paris-Saclay and Beihang University. Thank him for the continuous support of my Ph.D study and research, for his profession, patience, and immense knowledge. His guidance helped me in all the time of research and writing of this thesis. I am always impressed by his rigorous attitude and devoted spirit to the academic work. I would also like to thank all my colleges at Centre de Nanosciences et de Nanotechnologies: Prof. SAINT-MARTIN Jérôme, Prof. DOLLFUS Philippe, Prof. PALA Marco, Prof. CASSAN Eric, Dr. NGUYEN Mai Chung, Dr. DAVIER Brice, Dr. CHOUKROUN Jean, Mme. STEPHEN Laurence and Mme. ANDALON Lydia. I appreciate China Scholarship Council for the funding which supports me to study in France for 18 months.

I appreciate Prof. FERT Albert and Prof. ZHAO Weisheng in Beihang University. They stimulated my interests in academics and lead me to the world of spintronics. Their supervision and encouragement are indispensable for me. I also want to thank the spintronics community, I can always get help and inspirations from conferences and discussions, I enjoy working in such a friendly and energetic community.

Lastly, I give special thanks to my families. They do not know what spin angular momentum is, but they support me to do what I like. They are always my source of strength and solid backing, thanks them a lot.

Titre : Etude ab initio du transport quantique dépendant du spin

Mots clés : la magnétorésistance à effet tunnel, l'effet de Hall de spin, l'efficacité d'injection de spin, la jonction tunnel magnétique, le système bidimensionnel, le calcul ab initio

Résumé :
Les dispositifs spintroniques exploitent le degré de liberté du spin électronique pour traiter l'information. Dans cette thèse, nous étudions les propriétés de transport quantique dépendant du spin pour optimiser les performances des composants associés. Par l'approche ab initio, nous calculons la magnétorésistance à effet tunnel (tunneling magnetoresistance, TMR), l'effet Hall de spin (spin Hall effect, SHE) et l'efficacité d'injection de spin (spin injection efficiency, SIE). Nous montrons ainsi que les métaux lourds (heavy metals, HMs) influencent la TMR dans des jonctions tunnel magnétiques (magnetic tunnel junctions, MTJs) à base de MgO. L'utilisation de W, Mo, ou Ir peut améliorer la TMR. De plus, le dopage par substitution aide à optimiser le SHE dans les HM, ce qui renforce les angles de Hall de spin (spin Hall angle, SHA) pour rendre plus efficace le renversement d'aimantation par couple spin-orbite (spin-orbit torque, SOT) dans les MTJ. Afin de contourner les problèmes induits par le désaccord de maille entre couches ferromagnétiques et MgO, nous avons conçu une MTJ basée sur l'hétérojonction VSe_2/MoS_2 de van der Waals (vdW) et calculons la TMR à température ambiante. L'apparition d'effets de résonance tunnel permet d'utiliser la tension appliquée pour moduler la TMR dans cette structure. Nous proposons également d'y favoriser le SOT en utilisant des matériaux bidimensionnels (two-dimensional, 2D) avec un fort SHE. $MoTe_2$ et WTe_2 apparaissent comme de bons candidats. Ces dichalcogénures de métaux de transition (transition metal dichalcogenides, TMDC) présentent un fort SHE ainsi que de grands SHA grâce à leur faible conductivité électrique. Enfin, motivés par la demande d'un dispositif commutable 2D à grande longueur de diffusion spin, nous étudions un système d'injection de spin dans le silicène et obtenons des SIE élevés sous tension appliquée. L'ensemble de ces travaux apportent un éclairage pour la recherche de nouveaux dispositifs spintroniques.

Title : Ab initio investigations of spin-dependent quantum transport

Keywords : tunneling magnetoresistance, spin Hall effect, spin injection efficiency, magnetic tunnel junction, two-dimensional system, ab initio calculation

Abstract :
Spintronics devices manipulate the electron spin degree of freedom to process information. In this thesis, we investigate spin-dependent quantum transport properties to optimize the performances of spintronics devices. Through ab initio approach, we research the tunneling magnetoresistance (TMR), spin Hall effect (SHE), as well as spin injection efficiency (SIE). It has been demonstrated that heavy metals (HMs) are able to modulate TMR effects in MgO-based magnetic tunnel junctions (MTJs), and tungsten, molybdenum, and iridium are promising to enhance TMR. Moreover, substitutional atom doping can effectively optimize SHE of HMs, which would strengthen spin Hall angles (SHAs) to achieve efficient spin-orbit torque (SOT) switching of MTJs. To eliminate the mismatch between ferromagnetic and barrier layers in MgO-based MTJs, we design the MTJ with bond-free van der Waals (vdW) heterojunction VSe_2/MoS_2 and report the room-temperature TMR. The occurrence of quantum-well resonances enables voltage control to be an effective method to modulate TMR ratios in vdW MTJ. We put forward the idea of SOT vdW MTJ, which employs SOT to switch vdW MTJ and requires vdW materials with strong SHE. Research on $MoTe_2$ and WTe_2 verifies the possibility of realizing this idea. Both of them are layered transition metal dichalcogenides (TMDC) and exhibit strong SHEs, as well as large SHAs thanks to their low electrical conductivity. Lastly, motivated by the demand of a two-dimensional (2D) switchable device with long spin diffusion length, we construct the spin injection system with silicene monolayer, and reveal high SIEs under electric fields. Works in this thesis would advance the research of spintronics devices.

Université Paris-Saclay
Espace Technologique / Immeuble Discovery
Route de l'Orme aux Merisiers RD 128 / 91190 Saint-Aubin, France